A Proof-of-Concept Application of Principal Component Analysis For Identification of Anatomical Variations in Pharyngeal Flap Patients Experiencing Persistent Velopharyngeal Insufficiency

By

Taylor Falk

May, 2026

Director of Thesis: Alex Vadati, PhD

Major Department: East Carolina University Department of Engineering

Abstract

Cleft palates are one of the most common birth defects across the globe. The repair of cleft palates often includes the addition of a pharyngeal flap to assist with closure between the nasal and oral cavities. The failure rate of the pharyngeal flap placement is up to 30%, resulting in persistent velopharyngeal insufficiency, hyper-nasal speech, obstructive sleep apnea, and often requiring repetitive and expensive medical care. Many of these failures are caused by a lack of personalized surgical planning, using generic placement locations for the pharyngeal flaps. The generic placement of pharyngeal flaps is an insufficient method due to anatomical differences found in the patients receiving these surgeries. This study developed a proof-of-concept method for using principal component analysis to identify potential differences in anatomical shapes and compare them to clinical outcomes. An existing set of MRIs was used to identify shape variations found in patients with varying levels of velopharyngeal insufficiency. The identifications of these shape differences supported the ability to use the principal component analysis method for this kind of work. Results of this study provided the framework for future modeling projects. Further work with a larger and more homogeneous data set is needed to validate and expand on the findings made in this pilot study.

A Proof-of-Concept Application of Principal Component Analysis For Identification of Anatomical Variations in Pharyngeal Flap Patients Experiencing Persistent Velopharyngeal Insufficiency

A Thesis

Presented to the Faculty of the Department of Engineering

East Carolina University

In Partial Fulfillment of the Requirements for the Degree

Master of Science in Biomedical Engineering

By

Taylor Falk

May, 2026

Director of Thesis: Alex Vadati, PhD

Thesis Committee Members:

Jamie Perry, PhD

Stephanie George, PhD

Acknowledgements

I would like to express my gratitude to the many mentors of my academic career that brought this thesis to fruition. First, my advisor, Dr. Alex Vadati, for taking a chance on a chemist who wanted to be an engineer. His confidence in my abilities allowed me to achieve more than I thought possible two years ago.

I would also like to thank Dr. Jamie Perry and Emma Stewart for their expertly led crash course in pharyngeal anatomy. Without both, this project would not have made it past October. I would also like to thank Dr. Perry for her professionalism and dedication to my work over the past year. It is greatly appreciated. I would also like to thank Dr. Stephanie George for participating in my committee, your time and efforts spent on this project are greatly appreciated.

I would like to thank my mom, Ronda, for answering my panicked calls late at night and for keeping me sane. Thank you for supporting me in the endeavor that was graduate school, and for all the years before. Your financial, emotional, and physical contributions to my success do not go unnoticed or unappreciated.

I would like to thank my stepfather Darryl for the repetitive brainstorming sessions he participated in. A man of many words, some of which made it into this document. Your love for writing is unmatched, and I am grateful for your dedication to my success.

Lastly, I would like to thank Mackenzie Hoey for her friendship and guidance over the last two years. She is not only a great friend, but an incredible mentor. Thank you for introducing me to CrossFit, I had no idea the impact it would have on my graduate school experience and my life. May we have many more years of thinking in sync.

TABLE OF CONTENTS

List of Tables

List of Figures

CHAPTER 1: Introduction

Orofacial clefts are one of the most common congenital birth defects across the world, affecting about 1 in 700 births [1]. Individuals affected by clefts have an estimated lifetime cost of $200,000 including multiple dental and craniofacial surgical procedures [2]. Clefts are also associated with higher risks of mental health problems, higher infant mortality rates, and higher risks of various cancer types, with these complications being exacerbated in developing countries. Children left with unrepaired cleft palates face stigma and social isolation, decreasing socioeconomic opportunities [3]. Current cleft palate repairs can cost up to $70,000 in medical costs, with up to 30% of patients requiring a second surgery [4], [5]. Up to 40% of children with a repaired cleft palate continue to experience persistent velopharyngeal insufficiency (VPI) [6]. This occurs when full closure between the oral and nasal cavities is not complete and can result in hyper-nasal speech resonance and obstructive sleep apnea (OSA). To alleviate these symptoms, a common solution is the addition of a pharyngeal flap (PF), which is a small piece of tissue attached to the back of the soft palate. However, when placed in suboptimal positions, VPI can persist. Standard surgical plans are generalized and not specific to the patient. A more personalized analysis of an individual's anatomy could increase surgical success, improve quality of life, and provide a more economical solution to current cleft palate practices.

The goal of this study was to develop a proof-of-concept method to first identify shape variations in relevant anatomical structures of the pharyngeal system. This was done using post-operative magnetic resonance images (MRIs) from patients with pharyngeal flap placements to obtain a coordinate point system of their anatomies. Secondly these coordinate points underwent component analysis (PCA) to determine if there were identifiable regions of shape variation across the sample set. Finally, after determining regions of shape variation, patients with post-op improved hypernasality were compared to those continuing to experience persistent VPI and hypernasality symptoms to determine if there were patterns correlating specific anatomical characteristics to improved nasality scoring. The results of this pilot study provided the foundation for future modeling projects that may eventually lead to the application of statistical methods in VPI studies. Decreasing the need for repetitive surgical procedures could positively affect the lives of hundreds of thousands of children across the globe every year [2].

1.1 Cleft palate development and repair

Palates develop during weeks 4-12 of the embryonic gestation period [1]. The palatal shelves are located under the tongue and as the jaw develops, they are supposed to grow towards each other, eventually fusing. When fusion fails, the result is a cleft palate. There are four subtypes of clefts, (a.) incomplete cleft palate only, (b.) unilateral complete cleft lip and palate, (c.) bilateral complete cleft lip and palate, and (d.) cleft lip only (Figure 1). Patients in this study had varying subtypes of clefts repaired. This unpreventable variable could add to shape variation post-operation and can be avoided using stratification given larger sample sizes in future modeling projects.

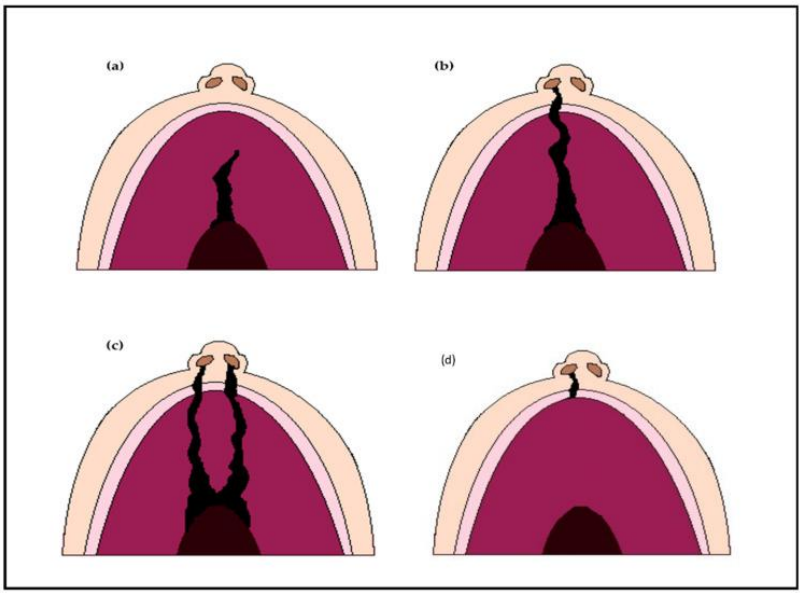

Figure 1. *The subtypes of clefts.* ***A.*** *Incomplete cleft palate only.* ***B.*** *Unilateral complete cleft lip and palate.* ***C****. Bilateral complete cleft lip and palate.* ***D****. Cleft lip only. Image from Babai and Irving with permission under Creative Commons Attribution 4.0 [1].*

Up to 40% of children with repaired cleft palates suffer from VPI which severely impacts speech development and overall quality of life [6]. To repair the cleft palate, a common surgical treatment, the PF, aims to correct this by narrowing the velopharyngeal port, by attaching a flap of tissue from the posterior pharyngeal wall to the soft palate (Figure 2). The PF is a widely used solution, occurring in over 85% of VPI repairs. PFs have a failure rate of up to 30% and carry substantial risk of symptoms such as OSA, airway obstruction, and flap dehiscence [6], [2]. These complications not only lead to persistent VPI but can seriously degrade the quality of life a child experiences post-repair, especially with prolonged hospital stays and increased exposure to anesthesia.

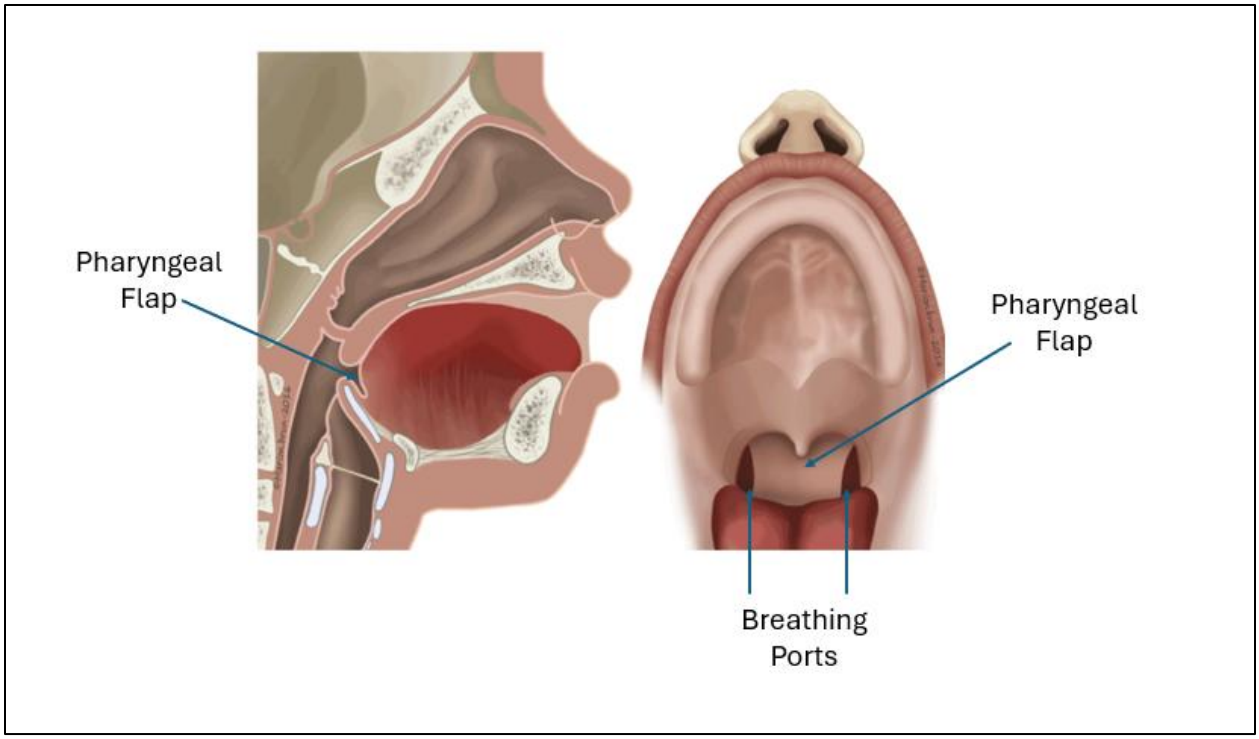

Figure 2. *On the left is the lateral view of pharyngeal flap placement. The flap connects the posterior pharyngeal walls to the soft palate. On the right is a superior view of the pharyngeal flap. On either side, there are small gaps left in the pharyngeal port to provide adequate air during nasal breathing. Image from Roessingh, et al. adapted from Creative Commons Attribution [7].*

The leading causes of a failed PF are the flap width and/or flap height being inconsistent with the specific needs of an individual's pharyngeal system. Airway obstruction can occur when a flap is too wide, but when the flap is too narrow it can produce residual hypernasality in cases where the lateral pharyngeal wall movement does not allow complete closure against the PF [8]. If the flap is placed too low, it increases the risk of flap failure. When placed below the plane of palatal closure, it can tether the flap and prevent full VP seal, causing OSA and hypernasality during speech.

Clinicians and the children they treat would benefit from a method to better understand potential correlations between patient anatomy and resulting symptoms after the addition of a PF. This study used MRI derived segmented models to develop a PCA method that identified regions of anatomical differences in patients after receiving a PF. By utilizing existing de-identified MRI datasets from patients with and without persistent VPI, this study aimed to create a method for identifying anatomical shape variations that may contribute to surgical successes or failures. This preliminary framework will be needed to later understand surgical outcomes across various anatomical conditions

CHAPTER 2: Background

The anatomy of the pharyngeal system works together to form closure between the nasal and oral cavities during speech and swallowing. When a patient has a cleft palate or repaired cleft palate the anatomy can fail to function normally. These complications can cause VPI and hypernasality to persist. Previous research includes many scalar measurement investigations. When volume measurements from MRIs were done using two-dimensional slices, there was more focus on the overall size of a structure than where that structure attaches to other regions, or how it functions [9], [10]. There is extensive documentation using MRIs that identify reductions in muscle length, velar thickness, and pharyngeal wall movement in children with persistent VPI, but this does not capture the multi-plane variation present in a three-dimensional (3D) system [11], [12], [13], [14], [15]. This study introduced PCA as a potential solution to identifying variation in a 3D space rather than using scalar measurements.

2.1 Anatomy of the pharyngeal system

Understanding the anatomy of the pharyngeal system in the context of cleft palates is essential for this work. The velopharyngeal mechanism is a muscular valve that connects the oral and nasal cavities and plays a crucial role in speech. It includes the soft palate (velum), the levator veli palatini (LVP), tensor veli palatini (TVP), palatoglossus, and the pharyngeal wall. During speech and swallowing, these structures contract to close the velopharyngeal port, separating the nasal and oral cavities. In children with a cleft palate, these structures are often misaligned or malformed. Most significantly, the LVP, responsible for lifting the velum, is often shortened and attached incorrectly [16]. The musculus uvulae, a key muscle for closure at the midline, may be absent or underdeveloped [17],[18], [19].

The velum retracts and elevates during velopharyngeal closure [18] and the PF is attached to the velum during surgery [20]. In this study, the PF was treated as part of the velum to facilitate segmentation and analysis. The musculus uvulae is an intrinsic muscle of the velum and sits in the sling created by the levator bundles [18]. The musculus uvulae fills the gap between the velum and posterior pharyngeal wall when closed, creating a seal as shown in Figure 3. In adults with normal velopharyngeal anatomy, the musculus uvulae is cylindrical and oblong [11]. The musculus uvulae has a bulk section located just above the LVP muscle sling. However, in patients with repaired cleft palate, the musculus uvulae is lacking in volume and this bulk section is not present. Since this bulk section is located where the palate contracts, the absence may contribute to VPI in patients with repaired cleft palate [11]. This study produced 3D models of the velum to provide better shape representation than would result from traditional size and volume measurements of the bulk section. The use of 3D modeling allows visualization of where the velum connects with other muscles in the pharyngeal system as they work together to seal the space between oral and nasal cavities.

The LVP muscles are responsible for most of the closing of the velopharyngeal system. Originating on either side of the base of the skull, the bundles of these muscles travel to the

middle of the velum where they fan outwards and join with the muscle from the other side as shown in Figure 3. During speech, the LVP pulls the velum up at a 45-degree angle until it closes against the posterior pharyngeal wall [6]. In patients with repaired cleft palates, the length of the LVP is often the same as patients without cleft palates. However, the volume, circumference, and diameter are significantly smaller in patients with repaired cleft palates. The differences in muscle size can induce abnormal velopharyngeal control for speech and swallowing [18]. There are observable differences in the lengths of the intra-velar (segment within the soft palate) and extra-velar (the muscles' attachment points on the velum) LVP. In children with VPI the intra-velar segment is significantly longer when compared to children with either no cleft palate or with cleft palate but no VPI. The extra-velar segment was found to be significantly shorter in those with VPI [13]. Previous works failed to describe the coordinated 3D positional variation across corresponding anatomical locations. This study used coordinates from all three dimensions to identify effects of shape and attachment points rather than muscle thickness and size.

Running parallel to the LVP, the TVP is a pair of thin and flat muscles also originating at the base of the skull [18]. Running medially and inferiorly, the TVP ends at a tendon wrapping around the hamulus of the medial pterygoid plate, which then continues into the velum as shown in Figure 3. The primary function of the TVP muscles are to open the eustachian tube during swallowing and yawning, allowing for drainage of fluids from the middle ear and equalization of air pressure across the ear drum [6]. During cleft palate repair it is critical to maintain the integrity of the TVP to prevent alterations to the eustachian tube's dilation mechanism. Adverse effects of failure to maintain the integrity of the TVP could lead to eustachian tube dysfunction and middle ear problems [21]. Previous MRI-based studies again used scalar measurements to determine differences in patients with cleft palates based on muscle length, thickness, and volume [22], [23]. This study focused on the shape differences in the 3D models rather than measurement differences to determine if coordinate point locations correlated to specific VPI symptoms.

The palatoglossus muscle originates from the lateral region of the velum and inserts into the lateral region of the tongue [18]. Acting as a direct antagonist to the LVP, this muscle smooths the movements of both the velum and the tongue during swallowing, improving the process by reducing the amount of swallowed air, and reducing spasm during swallowing to avoid choking. The specific attachment location of the palatoglossus varies among individuals, with some having a posterior attachment and some having a more anterior velar attachment point (Figure 3). This variation can affect the functionality of the LVP in certain individuals. Like the TVP, the palatoglossus is also a pair of muscles with a left and right segment. Current research uses muscle length, width, velar insertion, and angle measurements from two-dimensional MRI slices to determine the relationship between the LVP and palatoglossus placement [24]. While these are relevant measurements, they fail to capture the complex combinations of these measurements in a 3D space. This study used 3D models to understand how overall shape may vary and change

LVP attachment location, providing a more detailed understanding of the palatoglossus compared to scalar determinations.

In normal anatomy, the lateral and posterior pharyngeal walls move towards each other to create closure [18]. The superior, middle, and inferior pharyngeal constrictor muscles run along the posterior pharyngeal wall. Most relevant to velopharyngeal closure is the superior pharyngeal constrictor, comprised of multiple bundles such as the pterygopharyngeus, buccopharyngeus, mylopharyngeus, and glossopharyngues muscles. These fibers run along the posterior pharyngeal walls forming a ridge along the midline. Some of these fiber bundles also attach to the velum and contribute to retraction during velopharyngeal closure. Along the lateral pharyngeal walls lies the salpingopharyngeus muscle, which originates near the orifice of the eustachian tube [18]. This set of muscle fibers runs through the salpingopharyngeal fold and ends in the lateral pharyngeal walls. Not all individuals have this set of fibers, and they are unlikely to provide significant functionality to the velopharyngeal system.

Shape variations in pharyngeal walls are important to detect when planning the exact shape and location of a PF placement. In this study, the superior constrictor section of the pharyngeal wall was segmented for analysis as it contains the region that contacts a PF. Current research uses length, breadth, and cross-sectional area from MRIs to describe the pharyngeal wall [25]. While these measurements are useful for purposes such as airflow studies, they fail to identify the potential effects that shape may have on the overall function of the pharyngeal system. This study focused on the shape of the walls themselves as this can affect the ability of the PF to form a seal during closure.

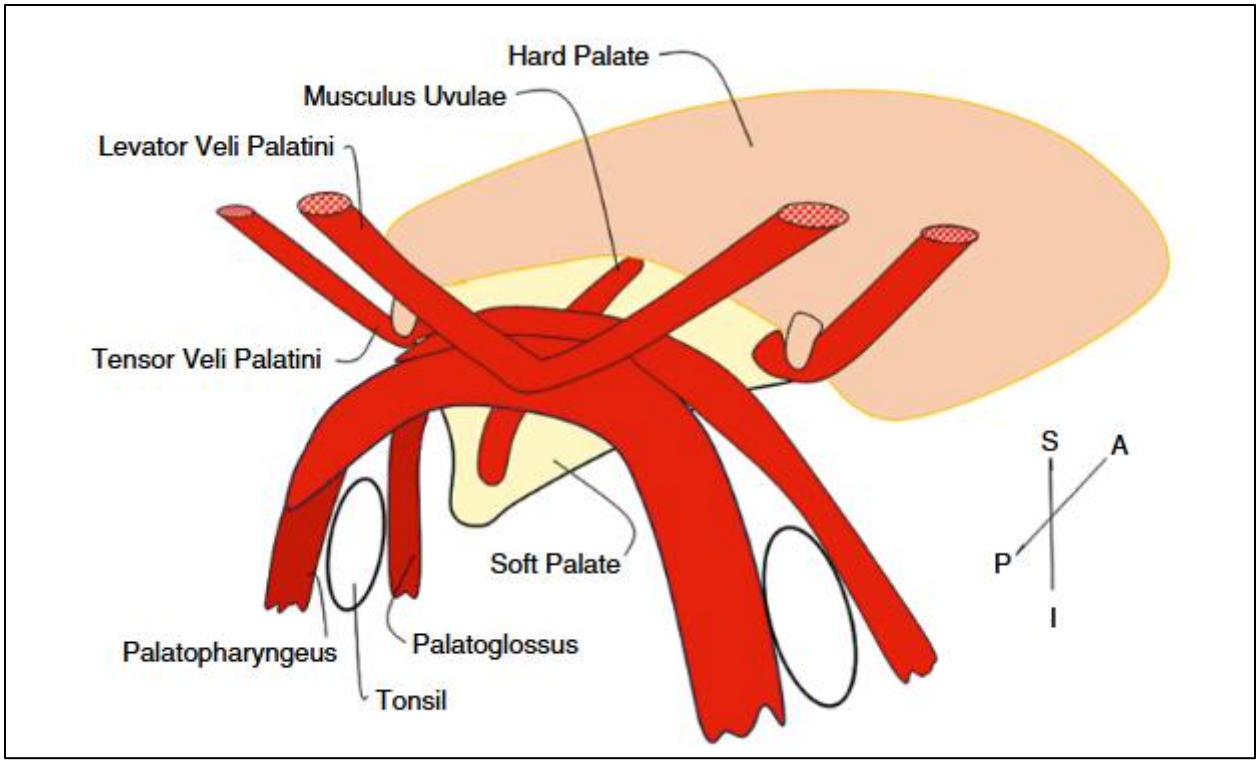

***Figure 3**. Diagram of relevant anatomical structures in the pharyngeal system including the hard and soft palates, LVP, TVP, palatoglossus, and musculus uvuvale [26]. Image from Boyd, et al. with permission obtained through the Copyright Clearance Center.*

2.2 MRI for Velopharyngeal Visualization and Modeling

The use of MRI for velopharyngeal visualization a is safer and more comfortable alternative to traditional nasendoscopy and videofluoroscopy techniques [14]. Additionally, MRI can obtain views of underlying musculature such as the levator muscle, while the traditional methods do not allow for such depth. To ensure the muscle is visible in both cleft palate and normal anatomical patients, the oblique coronal plane is best suited for image collection (Figure 4). Data in this study was collected from an existing set that used imaging protocols and training programs that reliably capture the levator muscle, soft palate, and surrounding structures, making MRI an ideal source for constructing accurate anatomical models of the pharyngeal system [14],[27],[28]. In this study, an MRI data set was obtained from existing scans and were segmented from the oblique coronal plane to maintain image quality and anatomical accuracy [14].

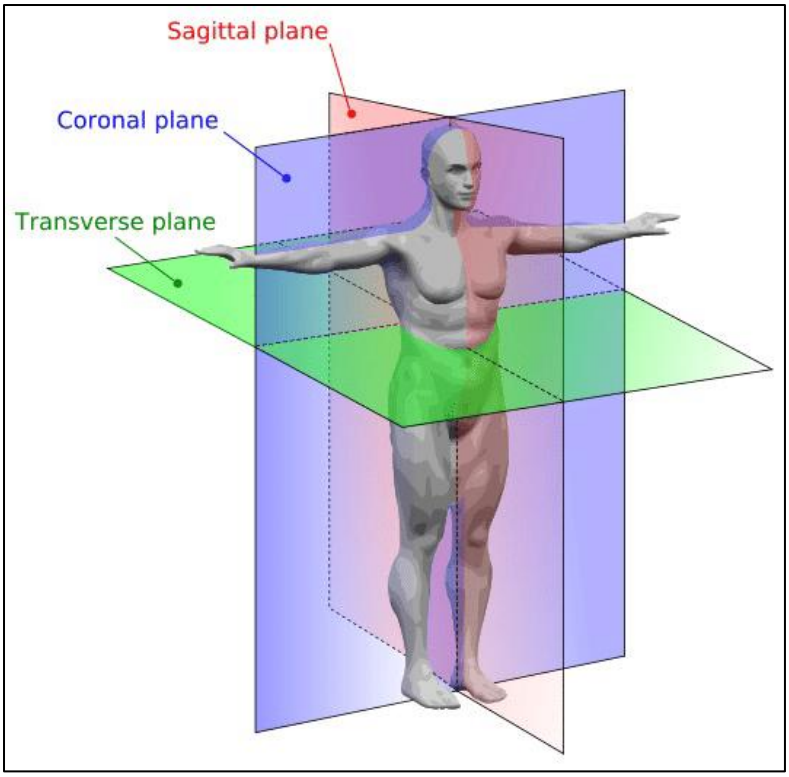

Figure 4. *Rendering of potential MRI acquisition planes [29]. Specific to this study is the intersection of the oblique and coronal planes displayed in blue and teal. Image from Das, with permission under the Creative Commons Attribution 4.0 International License.*

In 2024, Tran and colleagues [30] developed a framework for 3D subject-specific modeling by simulating the biomechanics in the velopharyngeal system after pharyngoplasty surgery, creating the basis for subsequent models of PF surgeries. After developing the models, researchers were able to simulate hypothetical surgical placements of pharyngoplasty tissue locations on the posterior pharyngeal wall (PPW). They modeled changes to the location of the tissue until velar contact with the pharyngoplasty tissue was achieved. Researchers also determined that successful surgeries had symmetrical LVP muscles while failed surgeries had asymmetric LVP muscles that overlap at the midline. This led to a second simulation where they generated different versions of the LVP muscle sling. The researchers measured the biomechanics of velopharyngeal closure of symmetric muscles and compared them to the computational model values of predicted failed outcomes. The ability of this study to identify differences between successful and failed outcomes in pharyngoplasty surgery provided the background needed to be confident that models can be developed for PF surgeries using MRI data.

2.3 PCA and Statistical Shape Modeling in Surgical Applications

Statistical Shape Models (SSMs) are applications of methods such as PCA used to compare medical imaging by creating a mean model shape and identify variation within a given data set [31]. SSMs use “modes” to explain percentage of shape variation between an average shape and the shape in a data set. These methods can be used for anatomical reconstructions in future work.

An example of a SSM with 10 modes showing shape variations in a mandible reconstruction study can be found in Figure 5 [32]. The current study was a pilot of coordinate point based PCA methods supported by previous uses of PCA and SSMs in biomedical applications.

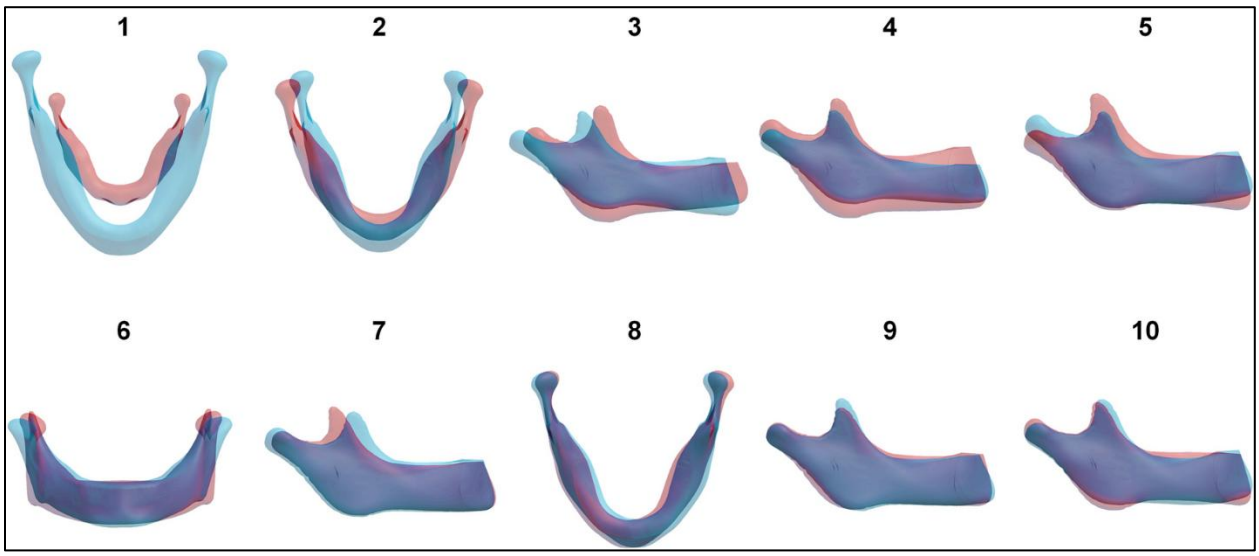

Figure 5. *Principal component modes 1–10. For each mode, two models are shown: a weight of − 3 standard deviations (red) and a weight of + 3 standard deviations (light blue). Dark blue zones represent overlap between these models [32]. Image and figure caption from Klop with permissions under Creative Commons Attribution 4.0 International License.*

The use of PCA on selected anatomical points has proven to be an appropriate technique for comparing shape variation among multiple patients. For example, Hylke, et al [33] collected cone beam computed tomography (CBCT) scans before performing bilateral sagittal split osteotomies to obtain images of the mandible [33]. Segmentation of the mandibles were done using an automated algorithm and manual improvements were made in MIMICS Core 27.0 [34] to produce 3D models. Evenly distributed "landmarks" were selected on all the models, and the mean position was calculated to provide a "mean mandible model". PCA was used to calculate shape variation from the mean model. After analysis, it was determined that the first three principal components (PCs) were responsible for a large part of variation. The current study followed a similar framework by segmenting MRIs, producing 3D models, selecting landmarks, and using PCA to compare patients to a mean shape, ultimately obtaining PC vectors indicative of potential shape variation.

Our study also aimed to identify which patients had the largest variation from the mean shape. To identify individual influence on shape variations, Rodrigquez-Florez et al. [35], created a population-based model to understand the effects of craniotomy size and spring positioning in sagittal synostosis repairs. These models were created by using 3D CT head scans pre and post spring insertion surgery to create stereolithography (STL) surface meshes in MeshMixer. From there, Rodriguez-Florez et al. used various packages in R to perform statistical analyses. They concluded that image-based SSM provides a powerful tool to understand the average effect of

individual surgical placements to guide surgeons in optimizing their approaches [35]. Our study used imaging-based techniques to obtain magnitudes of influence on PCs to determine individual effects on shape variation.

PCA can also be used in SSMs to identify which components are most influential in variations from the average anatomical model. For example, Rodero et al. [21] used SSMs to determine which localized anatomical changes affect cardiac functional outputs. They created four-chamber heart meshes sourced from 20 healthy patients' CT images to create an SSM. As a result, Rodero et al. [21] identified 18 components explaining the variance in shapes, with the first 9 explaining 89.99% of the variance. Our study used PCA to identify which regions of the anatomical structures could most explain shape variations in our data set. Identifying these regions can inform the preliminary framework for future computational modeling.

CHAPTER 3: Methods

A convenience sample of MRIs were obtained from a pre-existing set of images from Phoenix Children's Hospital for use in this study (IRB Number # - UMCIRB 20-002293).

3.1 Data Set

MRIs were sourced from 10 patients, all of whom had PF surgery. The data set contained intrinsic variables that may affect velopharyngeal anatomy, speech outcomes, and surgical procedures. With an age range from 4-26 years old, one patient at 26 exceeded the age range for pediatric study, one patient had 22q11.2 deletion syndrome, and one patient with OSA had no recorded speech outcome, this was considered an exploratory convenience sample. While the available data were heterogeneous, their availability contributed to the overall methodology-oriented study aims and provided a deeper understanding of the anatomical differences that could improve surgical intervention. Further, the heterogeneity introduced a level of variance that supported exploration of the limits of PCA feasibility for these types of analyses. Of these patients, four experienced corrections of their hypernasal speech and the OSA patient did not have recorded speech outcomes. In this study they were referred to as the "Improved-VPI group". The other five patients continued to experience hypernasality and were referred to as the "VPI group". The patients numbered 1-10, included patients 1-5 in the improved-VPI group and 6-10 in the VPI group. A summary of descriptive patient information can be found in Table 1, including age, sex, MRI and PF surgery dates, speech assessments at the time of MRI, cleft phenotype, PF placement, and operating surgeon. The patients from the VPI group had varying levels of VPI ranging from minimal to moderate cases of hypernasality, with descriptions of these levels found in Table 2.

Table 1. Patient Summary Information

Patient Number	Age (years)	Sex	MRI Date	PF Surgery Date	MRI Pre or Post PF OP	Speech Assessment	Cleft Phenotype (Repaired)	PF distance below palatal plane (mm)	Surgeon / Hospital
1	4	M	9/18/2024	4/3/2024	Post	Normal	Unilateral cleft lip and palate	15.7	Sitzman / Phoenix Children's
2	7	F	3/19/2025	8/26/2022	Post	Minimal Hypernasality	Unilateral cleft lip and palate	7.2	Phoenix Children's
3	8	M	2/15/2023	1/17/2019	Post	Minimal Hypernasality	Bilateral cleft lip and palate	9.2	Singh / Phoenix Children's
4	11	M	4/19/2023	6/14/2023	Post	Normal	Unilateral cleft lip and palate	12.0	Singh / Phoenix Children's
5	15	M	6/26/2021	Not applicable	Post	OSA (Speech not recorded)	Cleft palate	15.5	Phoenix Children's
6	26	F	3/01/2023	8/25/2023	Post	Mild Hypernasality	Cleft palate	7.5	Phoenix Children's
7	Not applicable	Not applicable	Not applicable	Not applicable	Not applicable	Not applicable	Not applicable	Not applicable	Not applicable
8	7	F	2/01/2023	2/24/2020	Post	Mild Hypernasality	22a11.2 Deletion Syndrome	5.1	Phoenix Children's
9	12	F	8/22/2022	3/3/2023	Post	Moderate Hypernasality	Bilateral cleft lip and palate	11.2	Singh / Phoenix Children's
10	13	F	12/20/2023	Not applicable	Post	Mild Hypernasality	Cleft Palate	15.5	Phoenix Children's

Table 2. Hypernasality Rating Scale For Clinical Settings [36], [37].

Level	Description
0	Normal: No Hypernasality
1	Minimal: Slight increase in nasal resonance
2	Mild: Noticeable hypernasality, mostly in high vowels
3	Moderate: Significant nasal resonance, frequent air emissions
4	Severe: Significant speech impairment

A summary of data preparation originating as DICOM images and ending at PCA analysis can be found in Figure 6.

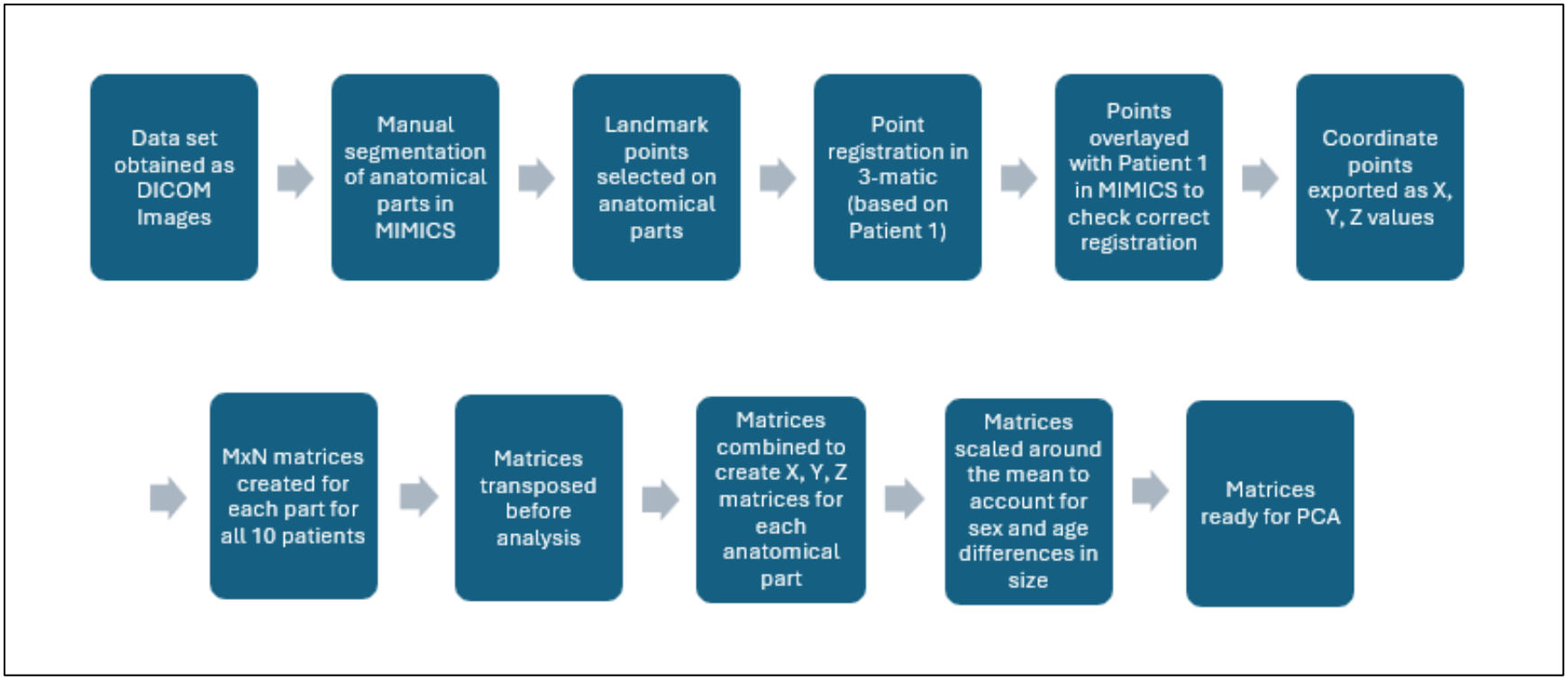

Figure 6. *Flowchart of data preparation process originating as DICOM images and progressing to PCA analysis.*

3.2 Image Segmentation

All 10 patient image sets were used to create 3D renderings of their anatomy in MIMICS 27.0 (Materialise NV, Belgium) [34]. Segmentation of the velum, LVP, TVP, palatoglossus, and pharyngeal wall was performed using the manual segmentation tool and used to create "parts" of the 3D models. Each part was meshed and smoothed in MIMICS 27.0 to remove any artifacts and ensure the entirety of each anatomical part was present in the model as shown in Figure 7. Patients 1-5 are represented in Figure 7.A1-A5. and patients 6-10 are represented in Figure 7.B1-B5. respectively.

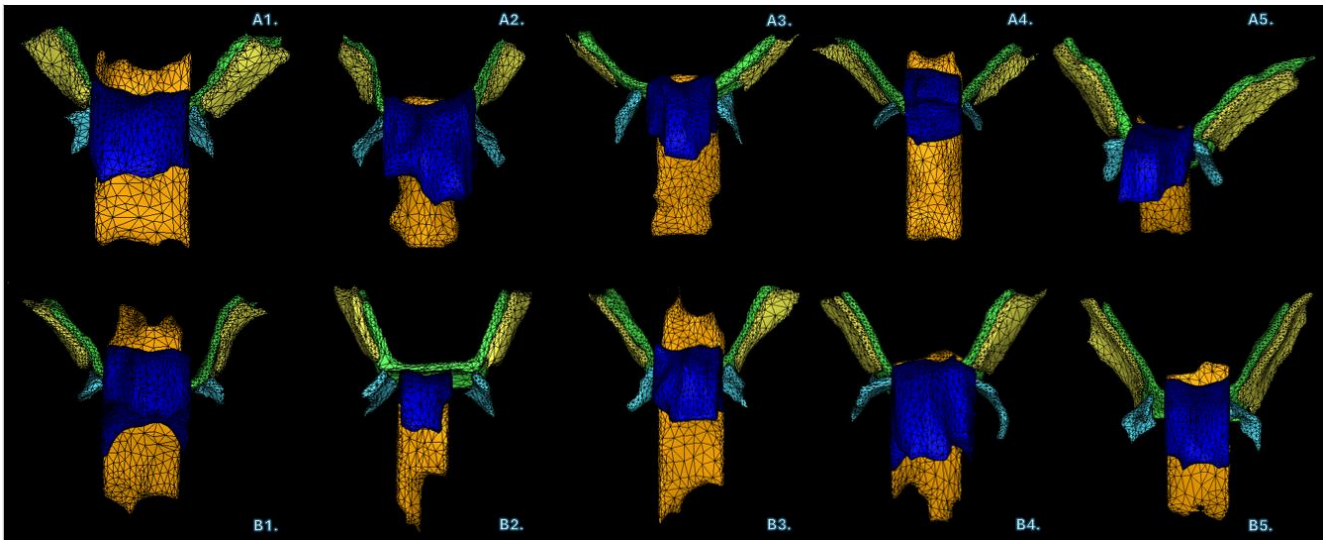

***Figure** 7. 3D models of all 10 patients. The velum is illustrated in dark blue, the LVP in green, the TVP in yellow, the palatoglossus in light blue, and the pharyngeal wall in orange. The A group consists of models from the Improved-VPI patients. The B group consists of models from VPI patients. **A1.** 3D model of patient 1. **A2**. 3D model of patient 2. **A3.** 3D model of patient 3. **A4**. 3D model of patient 4. **A5**. 3D model of patient 5. **B1**. 3D model of patient 6. **B2**. 3D model of patient 7. **B3**. 3D model of patient 8. **B4**. 3D model of patient 9. **B5.** 3D model of patient 10.*

3.3 PCA Landmark Point Selection

To obtain the coordinate point values needed to perform PCA, "landmarks" or "points" were selected on each structure in the 3D models. Efforts were made to choose the landmarks in the same order and same spacing on each patient model, to minimize inaccurate structural differences. However, without the use of automated landmark transfer or inter-rater and intra-rater reliability checks, it is likely that these manually selected points contributed to a part of the variance found in the study. In Table 3 the number of landmarks selected for each structure is provided and shown in Figure 8.

Table 3. Anatomical parts and their corresponding number of landmark nodes selected in MIMICS 27.0 [34].

Structure	# of landmarks
Velum	15 total
LVP	78 total
TVP	24 each side
Palatoglossus	12 each side
Pharyngeal Wall	10 total

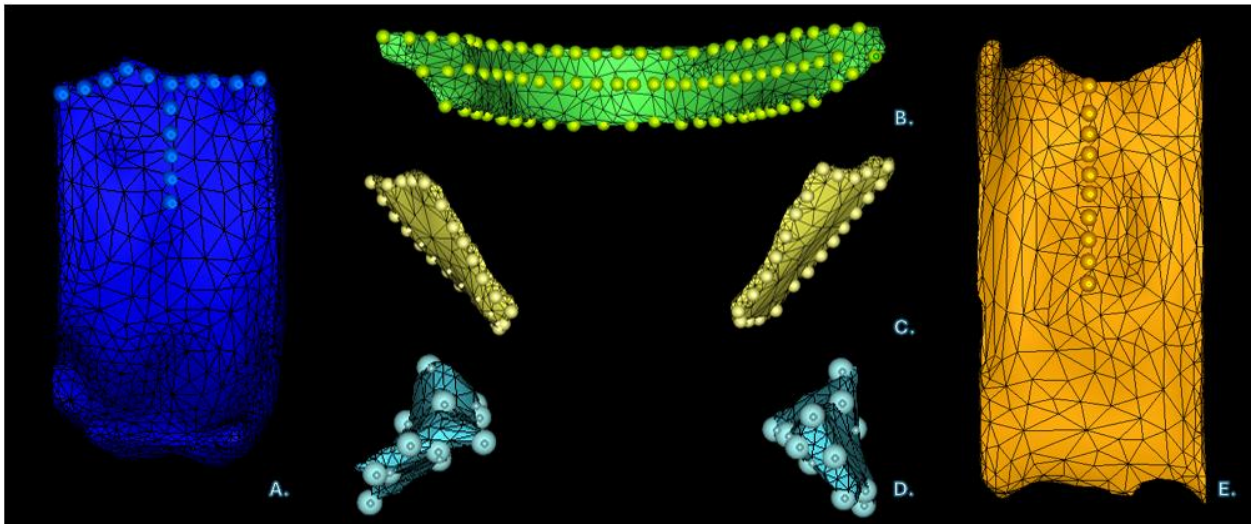

Figure 8*.Visualization of the points picked for each anatomical part.* ***A.*** *15 points picked on the velum.* ***B.*** *78 points picked on the LVP.* ***C.*** *24 points picked on both sides of the TVP.* ***D****. 12 points picked on each side of the palatoglossus.* ***E****. 10 points picked on the pharyngeal wall.*

Point picking was done in a consistent manner for all 10 patients. When selecting points for the velum, the first point was placed on the inferior left corner of the base, with 9 subsequent points running contralaterally. Five additional points were then placed beginning at the median of base and running in the anterior direction, totaling 15 points placed on each velum. An anatomical direction map can be found in Figure 9.

For the LVP, three rows of 26 points were selected beginning at the superior posterior left corner and running to the right superior posterior corner. The next row was made the same way, but anterior to the first row. The third row was made anterior to the second row, totaling 78 points on the LVP. The TVP points were picked in two parts. Points 1-24 were placed on the left segment's most anterior corner working in a counterclockwise direction. Points 25-48 were placed on the right segment, also beginning at the most anterior corner, but working in a clockwise direction, totaling 48 points on the TVP. The palatoglossus points were selected beginning with points 1-12 on the left segment, 4 points were placed on each face of the palatoglossus. The same was done

with points 13-24 on the right segment. A total of 10 points were placed on the pharyngeal wall, beginning at the median of proximal edge and running distal to the first point.

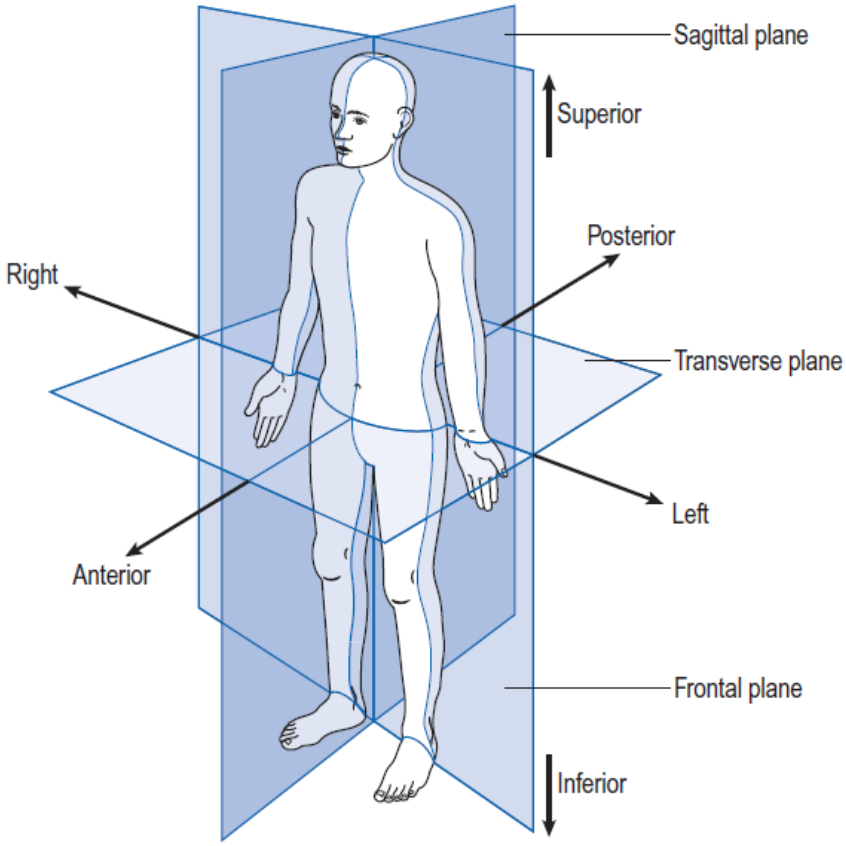

***Figure 9**. Visualization of anatomical directions relevant to the landmark point selecting process [38].*

3.4 Point Registration in 3-matic

The selected landmark points were imported into 3-matic for registration and alignment techniques [39]. Each patient was registered against Patient 1 using the N-Point registration tool. This approach, while convenient and reasonable for such a small sample, does not provide the same level of rigor as Procrustes alignment or an atlas-based registration strategy would provide for a larger sample. In the current study, the registration of other patients against Patient 1 was arbitrary and minimized to the extent possible of the concerns from potential imaging differences, including translational and rotational effects [40]. This method does not, however, reduce reference bias, thus hampering the predictive value of this approach. The N-point registration tool used selected reference points from a “fixed entity” and matched the points on the “moving entity”. The LVP part of Patient 1 was the selected fixed entity and had points selected on each end of the muscle, and one point in the center of the muscle (Figure 10). The LVP was chosen as the registration part because of its location near the center of the anatomical models, its many landmark points, and because it accounts for a significant difference in

velopharyngeal function. All other anatomical parts and previously selected points automatically shifted during registration to match the changes made in the LVP [41]. After registration, the models from each patient were overlayed with one another as shown in Figure 11. The newly registered coordinate points were then transferred back into MIMICS 27.0 and overlayed with Patient 1 to show the effects of registration on the landmark points (Figure 12). After registration was completed, the landmark coordinates were exported to MATLAB for further processing.

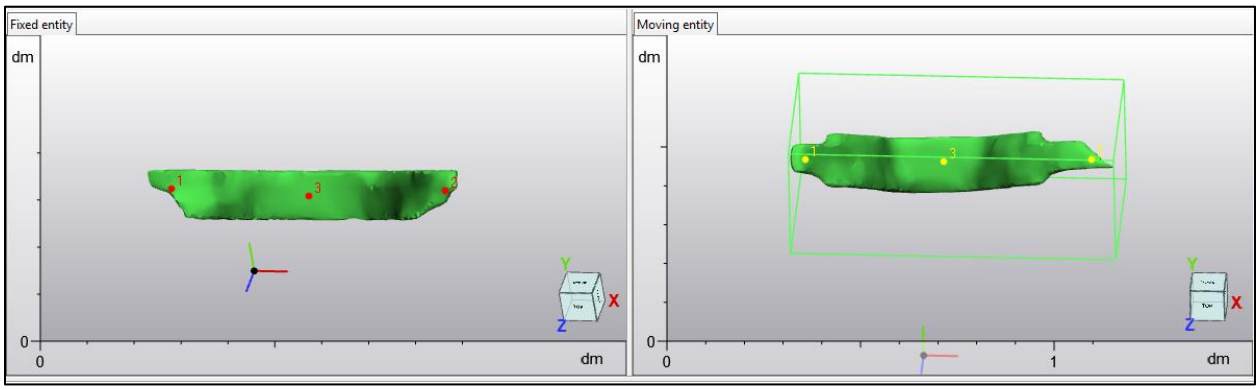

Figure 10. *Registration using the LVP from patient 1 and patient 5. The left side of the image indicates where the reference points were placed on patient 1's LVP (one on each end and one in the center). The right side of the image shows where the corresponding points were placed on patient 5's LVP. Registration eliminates effects from translation and rotation by using these reference points to overlay the models.*

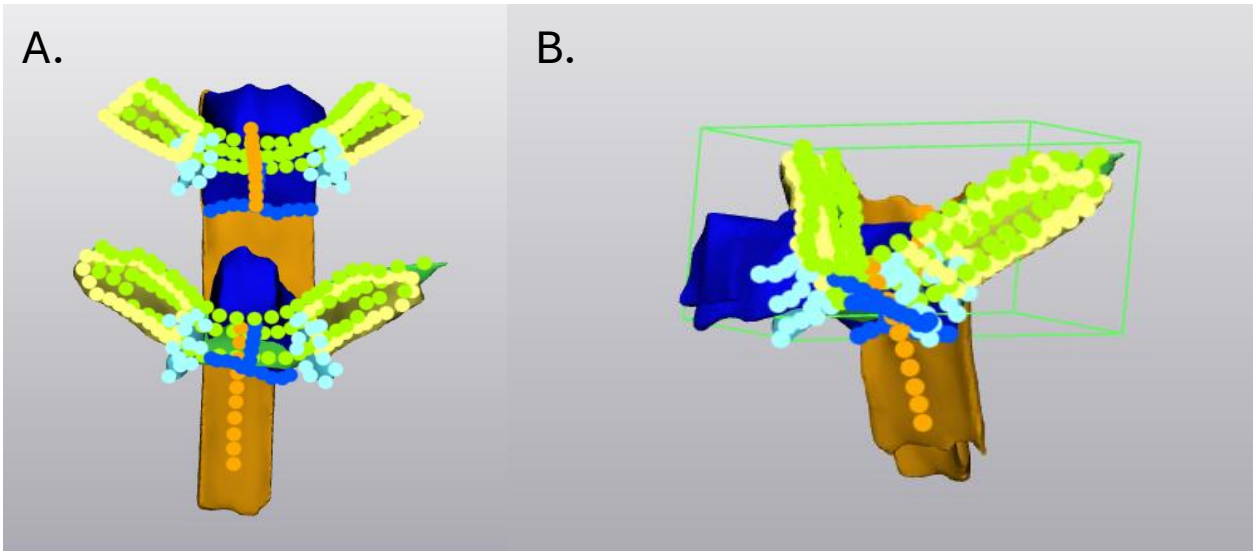

Figure 11. *Pre and Post registration of patient 5.* ***A.*** *Pre-registration there are translational and rotational effects evident in the models.* ***B.*** *Post-registration, the models are now overlayed and translational and rotational effects have been mitigated.*

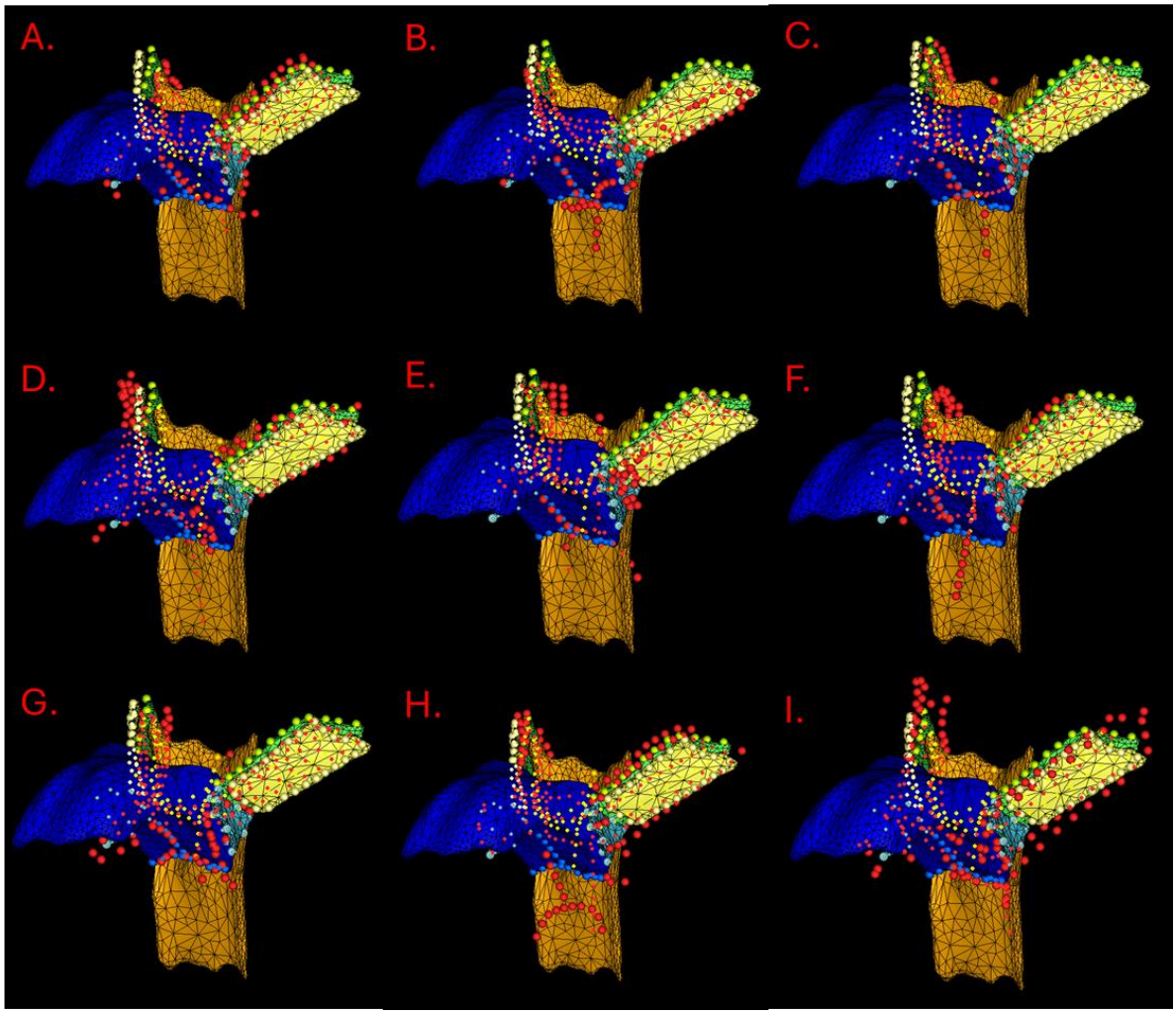

***Figure 12**. Registered points overlayed on the model from Patient 1. Overlayed points show up in red. **A.** Patient 2 points overlayed with patient 1 model. **B**. Patient 3 points overlayed with patient 1 model. **C**. Patient 4 points overlayed with patient 1 model. **D.** Patient 5 points overlayed with patient 1 model. **E**. Patient 6 points overlayed with patient 1 model. **F**. Patient 7 points overlayed with patient 1 model. **G**. Patient 8 points overlayed with patient 1 model. **H.** Patient 9 points overlayed with patient 1 model. **I.** Patient 10 points overlayed with patient 1 model.*

3.5 PCA Methods in MATLAB

PCA and data analysis was done using MATLAB R2024b [42]. The cartesian coordinates of the landmarks were exported into MxN matrices, where N represented the X, Y, and Z planes, and M represented the landmark point number. A matrix was created for all 5 structural parts of all 10 patients. Separately, matrices containing all X, Y, and Z coordinates for all parts of all patients were created in the same manner. The X, Y, and Z coordinate planes represented the sagittal, cortical, and axial anatomical planes respectively [43]. The X plane corresponded to left-right measurements, Y to inferior-superior measurements, and Z to anterior-postier measurements. This system allowed for direct correlation between coordinate points and distance measurements [44]. Examples of these matrices can be found in Appendix A.

To ensure that each point on a part was being compared to the same corresponding point on the other parts, each matrix was transposed to create NxM matrices where M still represented the landmark point number and N represents the coordinate planes. The transposed matrices were then used to create three distinct matrices per part. The velum, LVP, TVP, palatoglossus, and pharyngeal wall each have three PxM matrices where M represents the landmark point number and P represents the patient number for the separate X, Y, and Z measurements also found in Appendix A.

For the matrices containing the entire scope of X, Y, or Z matrices, points were entered into the matrix in the same order of their respective rows. Points were listed beginning with the velum, then the LVP, TVP, palatoglossus, and finally the pharyngeal wall. Patients 1-10 correlated to rows 1-10 in all matrices of this study. Examples of these matrices are also found in Appendix A.

To account for potential confounding measurements based on size (from different ages and sexes of patients) the data was scaled around a mean model. The mean of each matrix was found (for example: mean from all X values of the velum, all Y values of the velum, etc.). These mean calculations were used to divide the combined matrices, creating “scaled matrices” for all matrix sets (Example in Appendix A). This method of scaling applied provisional coordinate standardization before PCA to reduce gross differences in numerical magnitude across registered landmark sets. This step was used only as a pilot pre-processing procedure and should not be interpreted as formal anatomical size normalization. Therefore, the presented PCA results should be interpreted as exploratory shape-finding patterns after registration and provisional scaling, not as size estimates. Future landmark configurations should be analyzed after generalized Procrustes alignment and allometric effects should be evaluated where sample size permits.

Each X, Y, and Z scaled matrix for each anatomical part then underwent PCA using the intrinsic MATLAB [42] function, providing the resulting PC coefficients, scores, and percent explained matrices. These matrices were then interpreted to determine which points most influenced the PCs, how much shape variation was explained by the first PC, and if any patients could be deemed as outliers for each direction of each anatomical part. The outlying points were interpreted as exploratory descriptors of variation within this sample and cannot be interpreted as latent traits of the underlying population due to limitations of sample size and confounding differences in sex and age found in this data set. The same process occurred for the combined X, Y, and Z coordinate sets. An example can be found in Appendix A.

3.6 PCA Description

PCA is a statistical method used to reduce the dimensionality of a data set while simultaneously preserving variability [45]. It does this by finding variables (PCs) that maximize variance without correlating with each other. In the context of this study, PCs were the vectors that describe variations in the landmarks or points that affect VPI. PCA examined their influences on shape variation [46]. PCA was done using the “pca” MATLAB function, an intrinsic stepwise function that reduces the dimensionality of a large data set, while maintaining variance from

original data sets. The function automatically centered the input data by subtracting column means. To acquire PCs, the PCA function in MATLAB automatically used the singular value decomposition (SVD) method.

SVD begun with an M x N matrix A, with M ≥ N [47], [48]. Using Equation 1, let U and V be matrices orthogonal to A and let $\sum$ be a square diagonal matrix to A.

$$Equation\ 1:\ A = U\Sigma V^T \text{ [48]}$$

This equation contains the three steps of decomposition, a rotation (V^T), scaling (Σ), and another rotation (U) [48]. The V^T matrix contains the right singular vectors, which are eigenvectors of A^TA. The U matrix contains the left singular vectors, which are eigenvectors of AA^T. Finally, the Σ matrix contains singular values (non-negative diagonal entries, representing dimensional magnitude) which are the square roots of the eigenvalues of A^TA and AA^T.

After running the PCA function, the output data contained matrices called "coeff", "score", and "explained" that were used to identify the PCs, show shape variation in the reduced PC space, and quantify PCs explained variance [49]. The "coeff" matrix provided the PC vectors and when plotted showed which data points had positive or negative effects on the first two PCs. The "score" matrix showed where the original data set would appear in the new PC space. When plotted, data points that were similar clustered around the new mean of zero, while data points that varied, were farther from the center. The "explained" matrices quantified the percentage of variability each PC was responsible for. In most cases, the first three PCs made up almost the entirety of variation [50]. The PCs were listed in order of most variation explained to least explained.

3.7 Statistical Analysis using Interquartile Ranges

To identify potential outliers in the X, Y, and Z coordinate planes, which may indicate potential relationships between shape variation and clinical outcomes, the PC scores were plotted and analyzed using interquartile ranges (IQRs). This analysis was a small numbers data exercise that supported refinement of the method. The score plots represented the original data transformed into the lower dimension, PC space, with a new mean of 0 [51]. Even given these caveats, the manual placement of the picked points and subsequent registration could have acted as much to increase variance as to reduce it, making any predictive analytics suspect. The pilot nature of this project intended only to inform future analyses of larger, more homogeneous datasets.

The IQR for each set of scores were found (relating to the first 3 PCs), and if a point landed outside of the upper and lower limits (Quartile 1 -1.5*IQR and Quartile 3 +1.5*IQR) it was considered a statistical outlier (Appendix A) [52], [53], [54]. Due to problem of small numbers (N = 10) [55], statistical methods needed to be sensitive to deviations from the average, without being overly-sensitive to extreme variance, making the IQR method appropriate [52]. Box and whisker plots were also constructed for each data set to visually identify outliers [56]. Outliers in

each data set were considered to contain shape variations that have the potential to correlate with clinical outcomes.

3.8 Verification Using Residuals

To verify the modeling and properly identify potential outliers (which possibly identify shape variation), the PCA residuals were found for each data set in MATLAB (Appendix A). These calculations provided relative error measures to identify outliers and validate dimensionality [57]. In this context, a residual represented the vertical distance between the original data and resulting PCA coordinates after reduction. PCA residuals close to 0 indicated a strong fit between the PC and original data point. A PCA residual close to 1 indicated poor fit, with potential to identify an outlier. These residuals were calculated using the intrinsic “pcares” function in MATLAB as shown in Appendix A. The function required the number of PCs being retained to be indicated for each data set [58]. In this study, the first PC was retained and used to calculate residuals as the first PC was responsible for explaining the greatest percentage of shape variation. The amount of shape variation explained by each PC was found in the “explained” matrices from the PCA process. The residuals were plotted and values close to 0 were considered to have variation attributed to noise [59]. Residuals farther distributed from 0 were considered to have a weaker fit, with variation potentially explained by shape variation. A value of acceptable/unacceptable residuals was not selected, but this study allowed for a wider range of distribution to be deemed a good fit based on the exploratory nature of the project. Acceptable ranges of residual values are context dependent and can vary from study to study.

In future work, with larger data sets, and less confounding variables, a smaller range may be selected for more confirmatory analysis. However, since this is a small scale study with a heterogeneous data set, a wider range of acceptable residuals was appropriate [60]. Values presenting with a cluster around 0 were discussed as having a strong fit amongst the data set, while values with a wider distribution pattern were discussed as having a weaker fit by comparison.

CHAPTER 4: Results

The output of the PCA function provided coefficient matrices, percent explained matrices, and score matrices. The coefficient matrices showed positive and negative influence on PCs from each individual point in a data set. This explained which points may have a greater magnitude of variation between patients. The magnitude of influence on a PC may be indicative of shape variation in that region of the anatomical part. Coefficient plots were provided for each X, Y, and Z coordinate system for each part, and for combined X, Y, and Z sets. Percent explained matrices quantified the amount of variation each PC explained within its data set. In these data sets, the first three PCs showed almost all the variation in each anatomical part. The score matrices were representative of where the original coordinate points would land in the new PC space. The score plots used 0 as the mean of the new system and produced new coordinate points relative to this mean. For each part, patient outliers were identified by this plot if they were present within a system. PCA residuals were found from the original scaled coordinate systems to determine if the coordinates showed a strong fit within their respective systems, if variation could be explained by system noise, or if there was evidence of actual variation within the set.

4.1 Velum Results

The X coordinate system coefficient matrix values were plotted in Figure 13.A, showing each point's influence on the first two PCs. Since there were 15 points selected on the velum, there were 15 data points in Figure 13.A representing the comparison between all 10 patients. Points 1-6 and points 11-15 had a positive influence on PC 1, while points 7-10 had a negative influence on PC 1. A positive influence on a PC indicated that as the variable increases, the corresponding PC score would also increase. The first PC accounted for 97.01% of shape variation in the velum as indicated by Figure 13.B, and the second PC explained 1.83%. To determine if the X direction velum correspond to any outliers, Figure 13.C showed the scores of each of the 10 patients. Figure 16 contained box and whisker plots for the velum data sets, which identified outliers based on upper and lower limits (Q1 and Q3 ± 1.5 x IQR). There were no statistical outliers in the X plane as shown in Figure 16.A and indicated in Table 4.

The results of PCA performed on the Y direction of the velum can be found in Figure 14. Figure 14.A showed the individual point influence on the first two PCs. For the Y direction of the velum, all 15 points had a positive influence on PC 1; five out of 15 had a positive influence on PC 2. In Figure 14.B, 79.59% of shape variation could be linked to PC 1, with PC 2 accounting for 14.21%, and PC 3 with 4.05%. This indicated that variation in the Y direction may have been more distributed across the velum. Figure 14.C plotted the scores from the Y plane of the velum, with one statistical outlier from Patient 10's influence on PC 1 as shown in Figure 16.B and indicated in Table 4.

In the Z direction of the velum, individual point influence on PCs was shown in Figure 15.A where all 15 points positively influenced PC 1, and six positively influenced PC 2. In the Z direction, PC 1 explained 89.67% of shape variation, PC 2 explained 6.04% and PC 3 explained

3.03% as shown in Figure 15.B. Figure 15.C showed the score plots of the Z direction in the PC space, and Figure 16.C contained the box and whisker plot where outliers were identified as patients 6, 7, and 10, which were also indicated in Table 4.

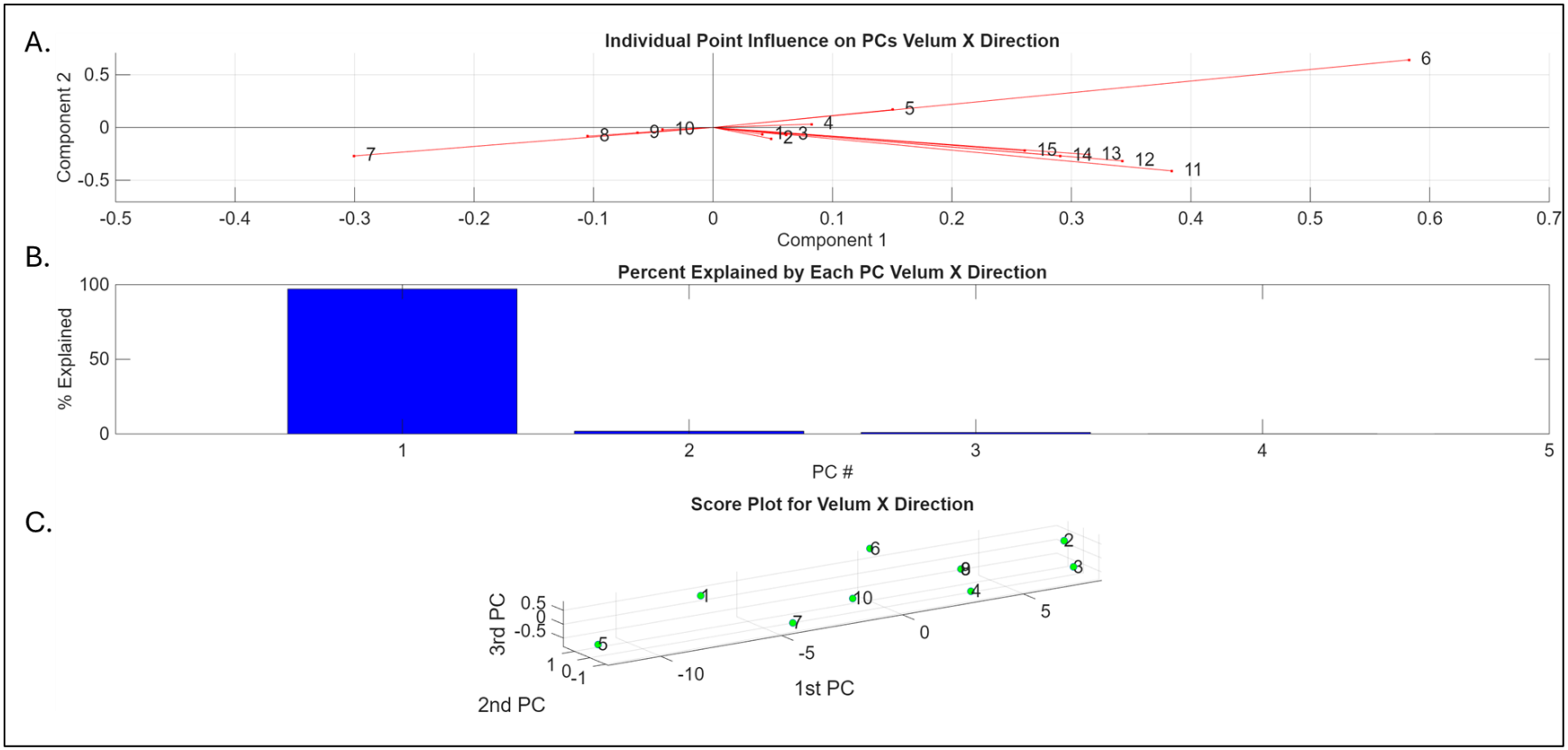

Figure 13. *PCA results for the X direction of the velum.* ***A.*** *Individual point influence on the first 2 principal components. Data points in the positive quadrants correspond to positive influence on the indicated principal component.* ***B.*** *Amount of shape variation that can be explained by the first 2-3 principal components quantified by percentage.* ***C***. *The score plot shows where the original data points will fall within the transformed PC shape. Points that create more similar shapes, cluster together around 0 after being transformed around the mean while variations may produce outliers.*

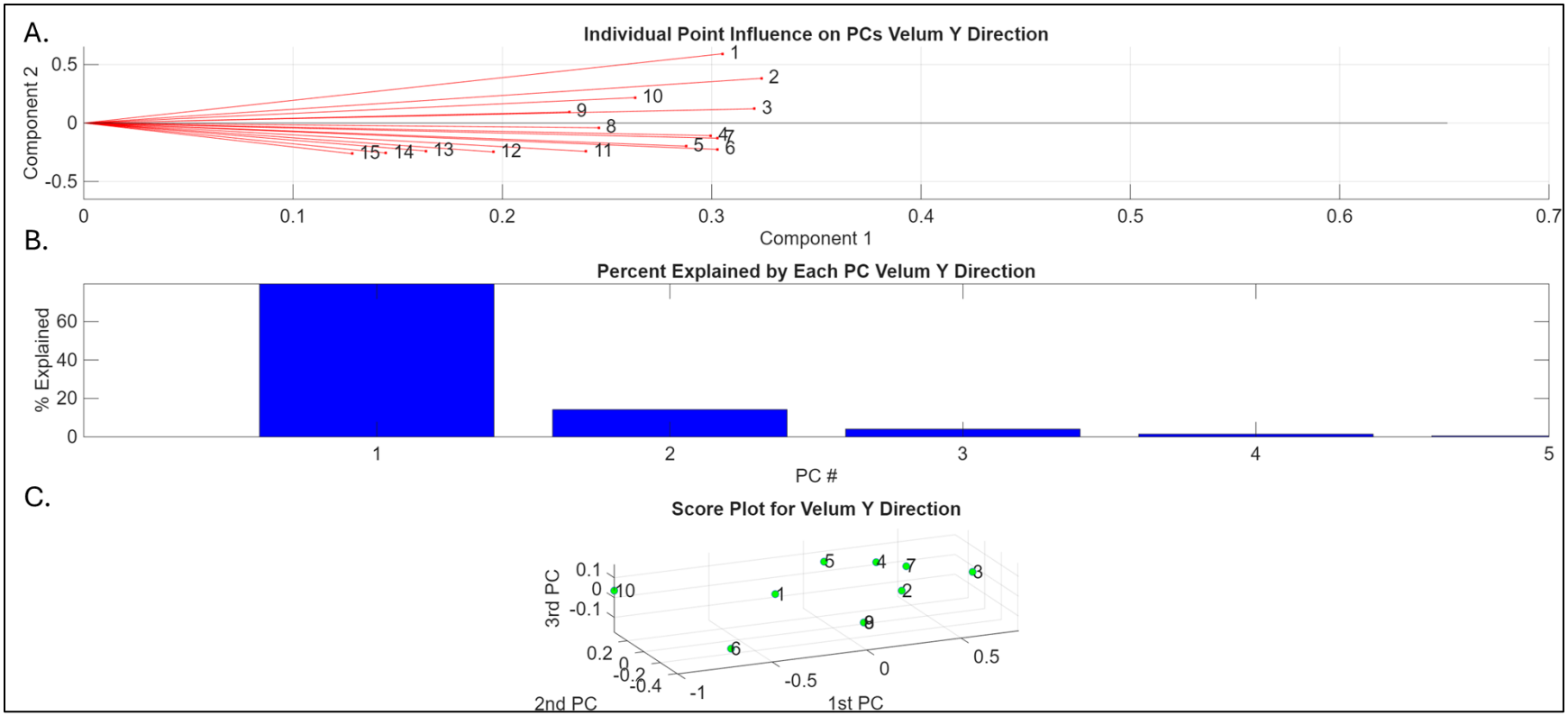

Figure 14. *PCA results for the Y direction of the velum.* ***A.*** *Individual point influence on the first 2 principal components. Data points in the positive quadrants correspond to positive influence on the indicated principal component.* ***B.*** *Amount of shape variation that can be explained by the first 2-3 principal components quantified by percentage.* ***C****. The score plot shows where the original data points will fall within the transformed PC shape. Points that create more similar shapes, cluster together around 0 after being transformed around the mean while variations may produce outliers.*

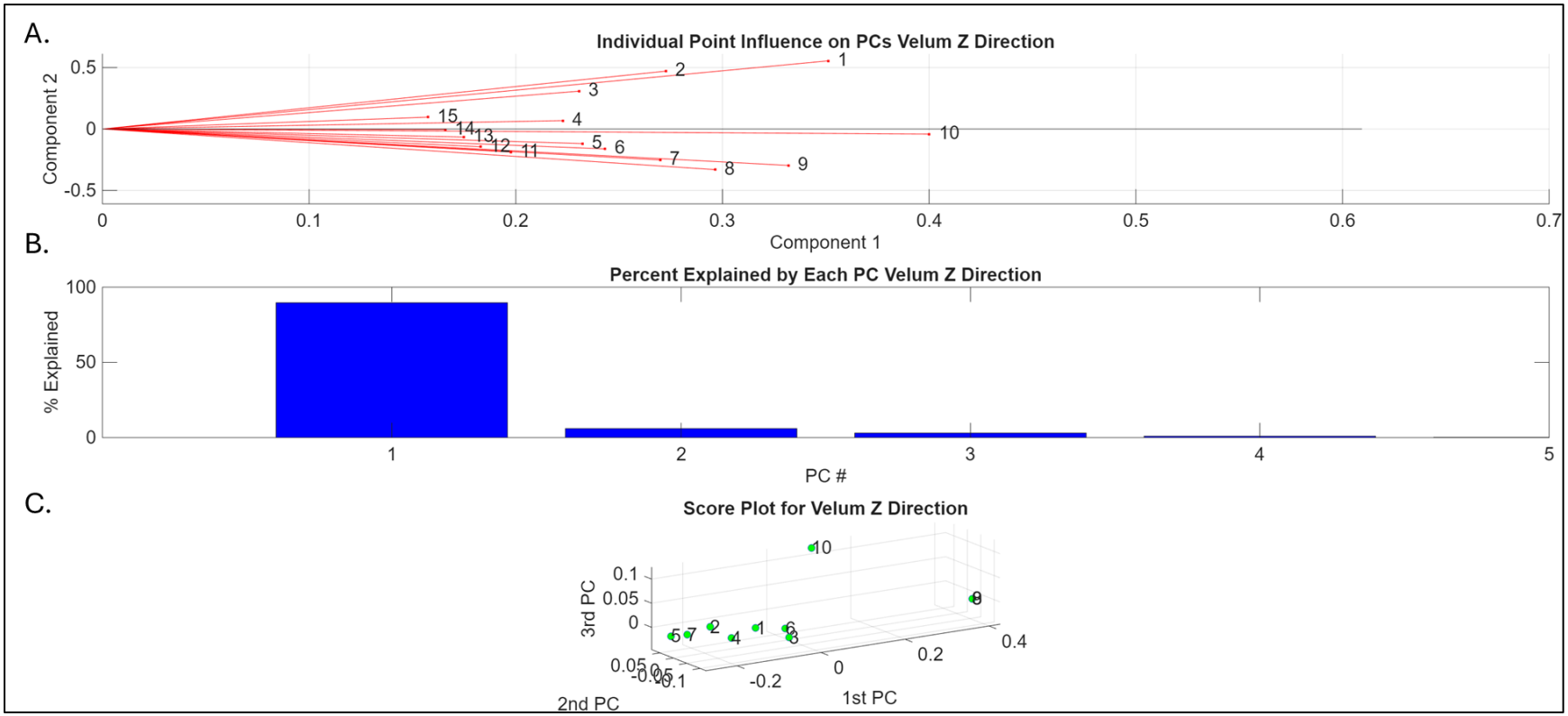

Figure 15. *PCA results for the Z direction of the velum.* ***A.*** *Individual point influence on the first 2 principal components. Data points in the positive quadrants correspond to positive influence on the indicated principal component.* ***B.*** *Amount of shape variation that can be explained by the first 2-3 principal components quantified by percentage.* ***C****. The score plot shows where the original data points will fall within the transformed PC shape. Points that create more similar shapes, cluster together around 0 after being transformed around the mean while variations may produce outliers.*

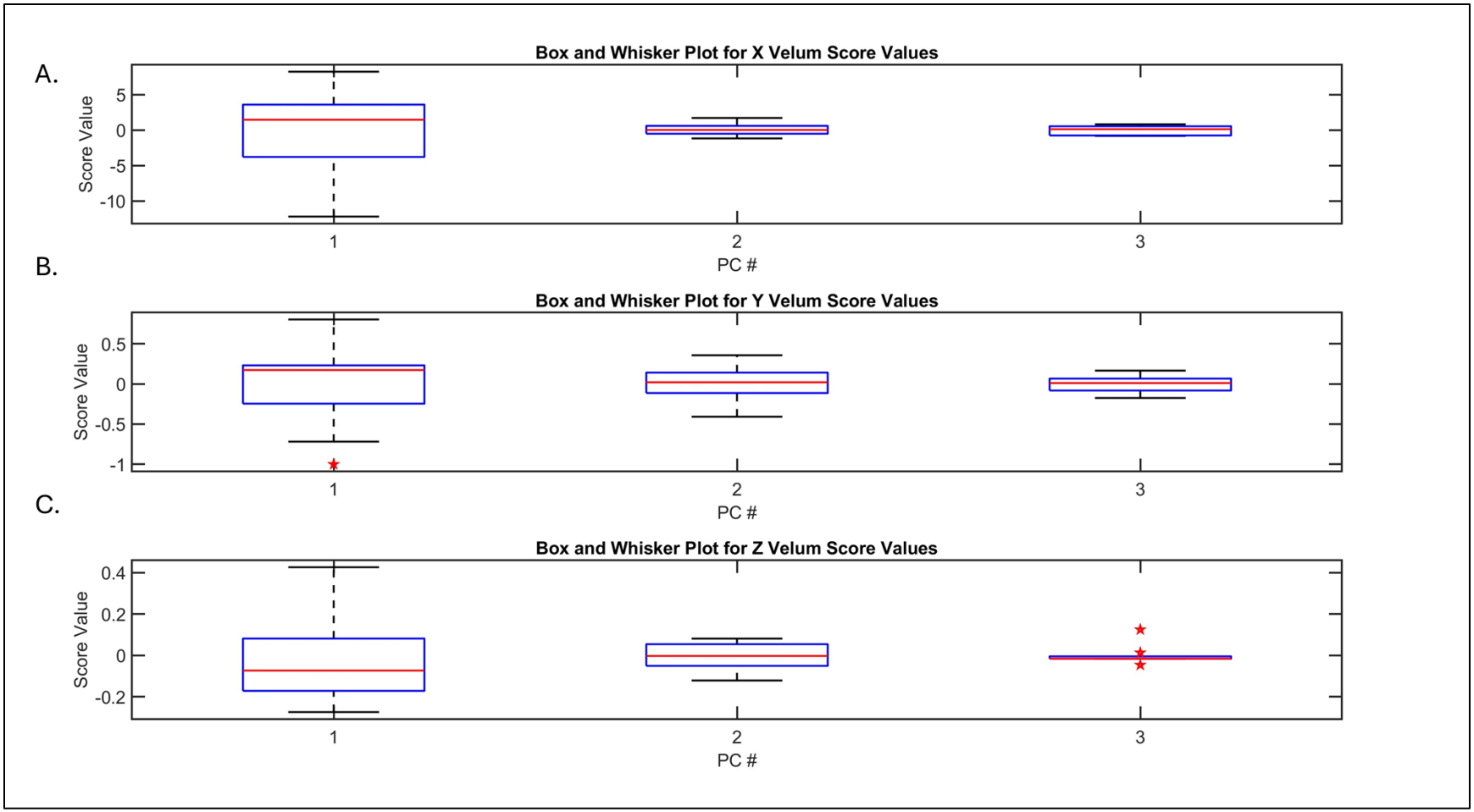

Figure 16. *Box-and-Whisker plots for velum data sets to identify potential outliers in patients 1-10. Statistical outliers are outside of upper and lower limits (± 1.5 x IQR) and are shown in red stars if present. Plots are created for score values of the first three PCs.* ***A.*** *Plots from the X plane data sets.* ***B.*** *Plots from the Y plane data sets.* ***C.*** *Plots from the Z plane data sets.*

Table 4. Outliers Found in Velum Data Sets

Plane	X	X	X	Y	Y	Y	Z	Z	Z
PC	**1**	**2**	**3**	**1**	**2**	**3**	**1**	**2**	**3**
Patient Number	None	None	None	10	None	None	None	None	6
Patient Number	None	None	None	None	None	None	None	None	7
Patient Number	None	None	None	None	None	None	None	None	10

4.2 LVP Results

The LVP had 78 points selected for analysis. In the X coordinate plane as shown in Figure B.20.A, there appeared to be a random distribution of positive and negative influence on PC 1 and PC 2. This made it difficult to identify an anatomical correlation between specific points. The first PC explained 99.79% shape variation, with PC 2 explaining 0.19% as shown in Figure B.20.B, meaning variation in X coordinate plane of the LVP was almost entirely explained in one directional vector. In Figure B.20.C, the score plot showed the PC scores for the X direction of the LVP with Figure B.23.A identifying patients 1 and 5 as outliers in PC 2, also indicated in Table 5.

Similarly in the Y directional plane, there was a visually random distribution of positive and negative influence on the first two PCs, as shown in Figure B.21.A. In Figure B.21.B, the first PC only explained 43.09% of shape variation, with PC 2 explaining 28.43%, and PC 3 explaining 15.37%. This indicated a wide distribution in variation of the Y coordinate plane of the LVP. There was not a cluster on the score plot, indicating no visual outliers in the Y direction (Figure B.21.C), with this being confirmed in Figure B.23.B and Table 5.

The Z direction of the LVP coefficient plot showed half of the points positively influencing the first PC and about half of them positively influencing the second PC (Figure B.22.A). This indicated two directional vectors of variation were present in this data set. Figure B.22.B showed shape variation explained by the first three PCs with PC 1, PC 2, and PC 3 explaining 36.85%, 28.06%, and 20.48% respectively, agreeing with the coefficient plot with a wide distribution of variation in this set. The Z direction did not have a defined cluster of score points, (Figure B.22.C), but had one statistical outlier at patient 10 as indicated by Figure B.23.C and Table 5

Table 5. Outliers Found in LVP Data Sets

Plane	X	X	X	Y	Y	Y	Z	Z	Z
PC	1	2	3	1	2	3	1	2	3
Patient Number	None	1	None	None	None	None	10	None	None
Patient Number	None	5	None	None	None	None	None	None	None

4.3 TVP Results

The TVP results of the X direction contained 48 points, most of which positively influenced the first two PCs (Figure B.24.A). In Figure B.24.B it was shown that the first PC explained 48.77% of the variance with the second PC explaining 27.93%, and the third explaining 16.97%, again showing a wide distribution of variation among this data set. The score plot for the X direction is found in Figure B.24.C with one statistical outlier at patient 5 on PC 1, as shown in Figure B.27.A and Table 6.

In the Y direction of the TVP, the points were split in half between positive and negative influence on PC 1 (Figure B.25.A.), and almost all positively influenced PC 2. The first PC in the Y direction explained 78.94% of the shape variation with the second and third explaining 7.70% and 6.50% respectively (Figure B.25.B). The score plot of the TVP showed a spread-out distribution in Figure B.25.C. There was a statistical outlier at patient 3 on PC 3 as shown in Figure B.27.B and Table 6.

The points in the Z direction had a split distribution on PC 1 and PC 2 with about half the points positively influencing both measurements (Figure B.26.A), again showing at least two directional vectors of variation in this data set. The first PC explained 54.35% of shape variation in the Z direction, with the second PC explaining 24.73%, and PC 3 explaining 13.42% (Figure B.26.B), agreeing with the coefficient plot of a wide distribution of variation. The Z direction of the TVP had a widespread distribution in the PC space in Figure B.26.C. Patient 10 was a statistical outlier on PC 2 in the Z direction as shown in Figure B.27.C and Table 6.

Table 6. Outliers Found in TVP Data Sets

Plane	X	X	X	Y	Y	Y	Z	Z	Z
PC	1	2	3	1	2	3	1	2	3
Patient Number	5	None	None	None	None	3	None	10	None

4.4 Palatoglossus Results

In Figure B.28.A, there were 24 points in the palatoglossus X direction, with all points positively influencing PC 1, and about half of them positively influencing PC 2, indicating a strong vector of variation. The first PC explained 91.36% of the shape variation in the X direction of the palatoglossus, with the second PC explain 3.62% and the third PC explaining 2.41% (Figure B.28.B), agreeing with the coefficient plot of a strong directional vector on PC 1. In Figure B.28.C it showed that patient 10 was a strong outlier on the score plot, landing on the opposite side of the point cluster which is centered around the mean of 0. This was confirmed in Figure B.31.A and Table 7 where patient 10 was an outlier on PC 1. Additionally, Patient 1 and Patient 5 were outliers on PC 2.

The points in the Y direction of the palatoglossus mostly had a positive influence on PC 1, with about half positively influencing PC 2 (Figure B.29.A). The first PC explained 38.66% shape variation, PC 2 explained 22.74%, and PC 3 explained 13.52% (Figure B.29.B) showing a widespread distribution of variation in this data set. Like other Y direction plots, the scores had a roughly even distribution on the plot with no visual outliers (Figure B.29.C). There were no statistical outliers in the Y direction as confirmed by Figure B.31.B and Table 7.

The points in the Z direction of the palatoglossus had mostly positive influence on PC 1 and PC 2 (Figure B.20.A). The first PC explained 39.55% of the shape variation in the Z direction, with the second PC explaining 28.48%, and PC 3 explaining 14.55% (Figure B.30.B), again indicating a wide distribution of variation in this set. The Z direction score plot had an even spread in Figure B.30.C, with no statistical outliers shown in Figure B.31.C and Table 7.

Table 7. Outliers Found in Palatoglossus Data Sets

Plane	**X**	**X**	**X**	**Y**	**Y**	**Y**	**Z**	**Z**	**Z**
PC	**1**	**2**	**3**	**1**	**2**	**3**	**1**	**2**	**3**
Patient Number	10	1	None	None	None	None	None	None	None
Patient Number	None	5	None	None	None	None	None	None	None

4.5 Pharyngeal Wall Results

The X direction of the pharyngeal wall provided a split distribution on PC 1, with patient 6 having the highest magnitude of influence (Figure B.32.A). The first PC explained 99.98% shape variation in the X direction, with the second PC explaining 0.01% (Figure B.32.B). The score plot showed a cluster around the mean with visual and IQR outliers at points 3 and 5 (Figure B.32.C), which was confirmed in Figure B.35.A and Table 8.

In the Y direction, the positive influence on PC 1 increased in numerical order while the positive influence on PC 2 decreased in numerical order (Figure B.33.A). The first PC explained 82.62%

of the shape variation in the Y direction of the pharyngeal wall, with PC 2 explaining 16.56%, and PC 3 explaining 0.63% (Figure B.33.B). The score plot showed a near even distribution between points (Figure B.33.C), with one statistical outlier at patient 5 on PC 2 as shown in Figure B.35.B and Table 8.

The Z direction of the pharyngeal wall behaved in the reverse of the Y direction. All 10 points still positively influenced PC 1, but positive influence on PC 2 increased in numerical order (Figure B.34.A). In the Z direction, PC 1 explained 91.78% of shape variation, and PC 2 explained 8.13% (Figure B.34.B). The score plot showed a spread-out distribution in Figure B.34.C. There were no statistical outliers in the Z direction as indicated by Figure B.35.C and Table 8.

Table 8. Outliers Found in Pharyngeal Wall Data Sets

Plane	**X**	**X**	**X**	**Y**	**Y**	**Y**	**Z**	**Z**	**Z**
PC	**1**	**2**	**3**	**1**	**2**	**3**	**1**	**2**	**3**
Patient Number	3	None	None	None	5	None	None	None	None
Patient Number	5	None	None	None	None	None	None	None	None

4.6 Combined Results

The combined data sets contained 175 points encompassing all five anatomical parts for all 10 patients. In the set of X coordinates, there was a strong influence on PC 1 and PC 2 from points 56 and 82, with most other points centered around 0 (Figure B.36.A), which could indicate specific regions of shape variation. The first PC explained 95.11% of shape variation, with the second PC explaining 3.87% in Figure B.36.B, indicative of one strong directional vector of variation. In Figure B.36.C. the score plot for the X direction combined data showed statistical outliers on PC 1 from patients 2 and 3, with outliers on PC 3 from patients 4 and 10 as confirmed in Figure B.39.A and Table 9.

The Y coordinate for the combined data set showed all 175 points influencing PC 1 positively (Figure B.37.A), indicating a strong directional vector of variation. The first PC in the Y coordinates explained 93.84% shape variation, with PC 2 explaining 3.10%, and PC 3 explaining 1.55% (Figure B.37.B), agreeing with the coefficient plot of a strong first PC vector. There were no visual outliers on the score plot in Figure B.37.C but there was one statistical outlier on PC 3 from Patient 1 as indicated by Figure B.39.B and Table 9.

Finally, in the Z coordinate plane for all combined data, the influence of each point was grouped close together with positive influence on PC 1 (Figure B.38.A.) that explained 99.05% of shape variation (Figure B.38.B). This indicated that almost all the variation in this coordinate set could be explained by one vector. The Z coordinate score plot showed an even distribution in Figure B.38.C with no statistical outliers indicated in Figure B.39.C and Table 9.

Table 9. Outliers Found in Combined Data Sets

Plane	X	X	X	Y	Y	Y	Z	Z	Z
PC	1	2	3	1	2	3	1	2	3
Patient Number	2	None	4	None	None	1	None	None	None
Patient Number	3	None	10	None	None	None	None	None	None

Specific patients stood out as repeat outliers on PC 1. Patients 3, 5, and 10 were all identified twice as being outside of the upper or lower limits based on IQR measurements of their score values. Patient 3 was from the improved-VPI group with minimal hypernasality after the addition of the PF. Patient 5 was from the improved-VPI group as well, but unique as the only patient in the set experiencing OSA symptoms and did not have a recorded speech score. Patient 10 was from the persistent VPI group and experiencing mild hypernasality after PF placement. These repetitive outliers could be indicative in true anatomical differences but would need to be further analyzed in a study with a larger and more homogenous data set. A summary of patient outlier identification counts can be found in Table 10.

Table 10. Patient Outlier Identification Counts

Patient number	# of Times Outlying in PC 1	# of Times Outlying in PC 2	# of Times Outlying in PC 3	Total Times as an Outlier	Speech Outcome
1	0	1	1	2	Normal
2	1	0	0	1	Minimal Hypernasality
3	2	0	1	3	Minimal Hypernasality
4	0	0	1	1	Normal
5	2	2	0	4	OSA (No Speech Recorded)
6	0	0	0	0	Mild Hypernasality
7	0	0	0	0	
8	0	0	0	0	Mild Hypernasality
9	0	0	0	0	Moderate Hypernasality
10	2	1	1	4	Mild Hypernasality

4.7 PCA Residuals for Model Validation

The PCA residuals for each data set were calculated in MATLAB using the “pcares” function (Appendix A) and plotted to indicate validity of the model and highlight potential outliers. Residual points with a cluster around 0 were considered to potentially have variance based on

noise in the system. Residual points with a wider distribution pattern were further discussed as potential outliers in the data.

Residual points for the X direction velum set are found in Figure 17 with most of the data presenting a clustered distribution pattern close to 0. Points with a more spread distribution mostly included points from the first half of the data set, which were the points found at the base of the velum. In the Y coordinates of the velum, almost all the residual points were close to 0 as shown in Figure 18, with one point on patient 2 and patient 6 showing a weaker correlation. In the Z direction of the velum, all the residual points were close to 0 as shown in Figure 19, with most of the points within 0.05, showing a strong correlation of data.

The residual points for the X direction of the LVP are shown in Figure B.40, where most of the points have a tighter distribution around 0, with points at the beginning of the set shown to have a larger distribution. These beginning points came from the points selected in the first row of LVP points. In the Y direction of the LVP, almost all the residual points had a tight distribution around 0, with a few points on patients 1, 2, 4, 5, and 10 showing a weaker correlation in Figure B.41. The Z direction of the LVP exhibited the same pattern as the Y direction, with most of the residuals close to 0 and patients 1, 2, 4, 5, and 10 having a weaker correlation in Figure B.42.

The residual points in the X direction of the TVP also mostly presented a tight distribution close to 0 for a strong correlation in Figure B.43. Patients 1, 3, 5, and 7 had a few points in the first half of the data set that had a more spread distribution. These points corresponded to the left side of the TVP where points were picked first. The Y direction of the TVP residuals also fell mostly close to 0, with a few points on patients 3, 4, 5, 6, 7, and 10 showing a weaker correlation in Figure B.44. The Z direction of the TVP had a similar pattern, with almost all the points having a tight distribution close to 0, and patients 3, 4, 5, 7, and 10 having a few points with a weaker correlation in Figure B.45.

On the palatoglossus X plane, there was a more spread distribution pattern, except on patient 10 where all the points were close to 0 in Figure B.46. The points with a spread distribution did not adhere to a pattern and were randomly distributed across the parts. The Y direction of the palatoglossus had a stronger correlation within the data set but had a few points indicating a weaker correlation for most of the patients in Figure B.47. Similarly, the Z direction of the palatoglossus mostly had points close to 0, with a few points on each patient showing a weaker correlation, except for patient 7 where all points indicated a strong fit as shown in Figure B.48.

Residual points from the X direction on the pharyngeal wall showed a poor fit amongst patients as shown in Figure B.49. The Y direction of the pharyngeal wall showed a better fit for most patients with patient 5 having the widest distribution in Figure B.50. The Z direction showed the same pattern as the Y direction with a strong fit except for patient 5 in Figure B.51.

For the combined X direction data set, the residual points clustered close together around the mean but still contained many points spreading farther from 0 in Figure B.52. In the Y direction,

there was a tight spread with most points close to 0, and points thinning in distribution as they got farther away from 0 in Figure B.53. The combined Z direction points were almost all close to 0, with a few points showing a weaker correlation for patients 1, 6, 7, and 9 in Figure B.54.

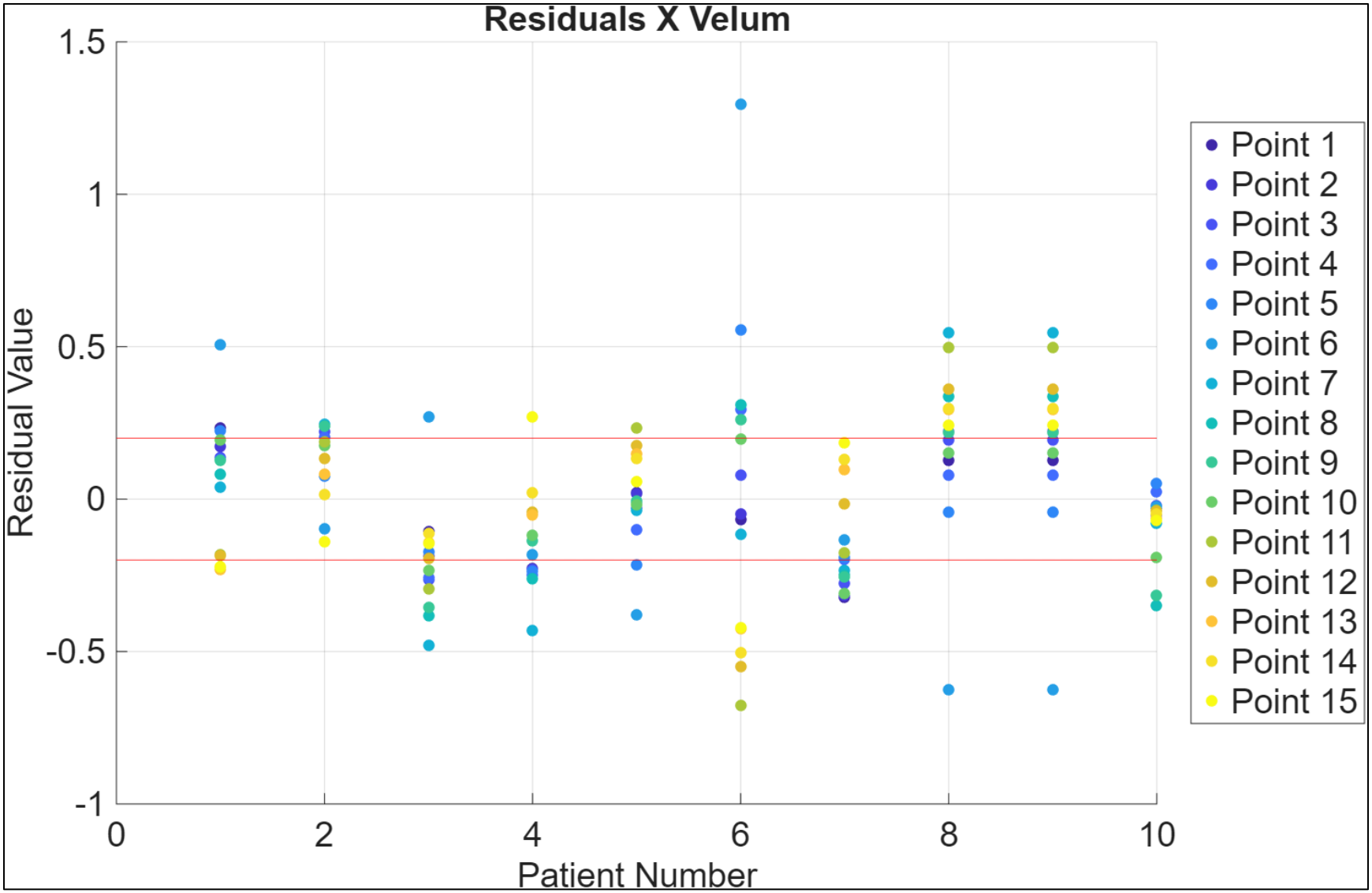

Figure 17. PCA residuals for the X direction of the Velum. Points close to 0 indicate a strong fit with points farther away from 0 indicating a weaker fit.

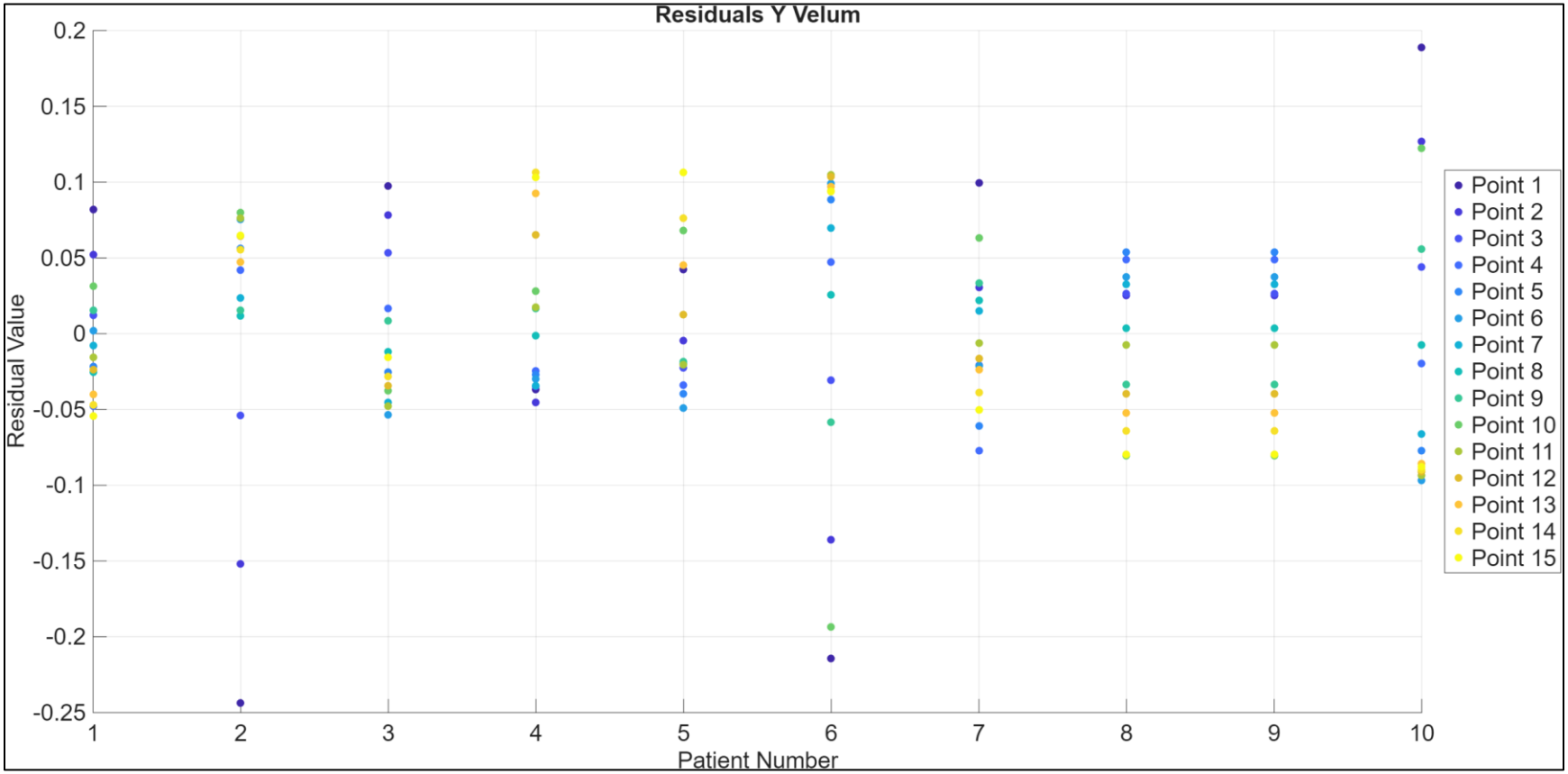

Figure 18. *PCA residuals for the Y direction of the Velum. Points close to 0 indicate a strong fit with points farther away from 0 indicating a weaker fit.*

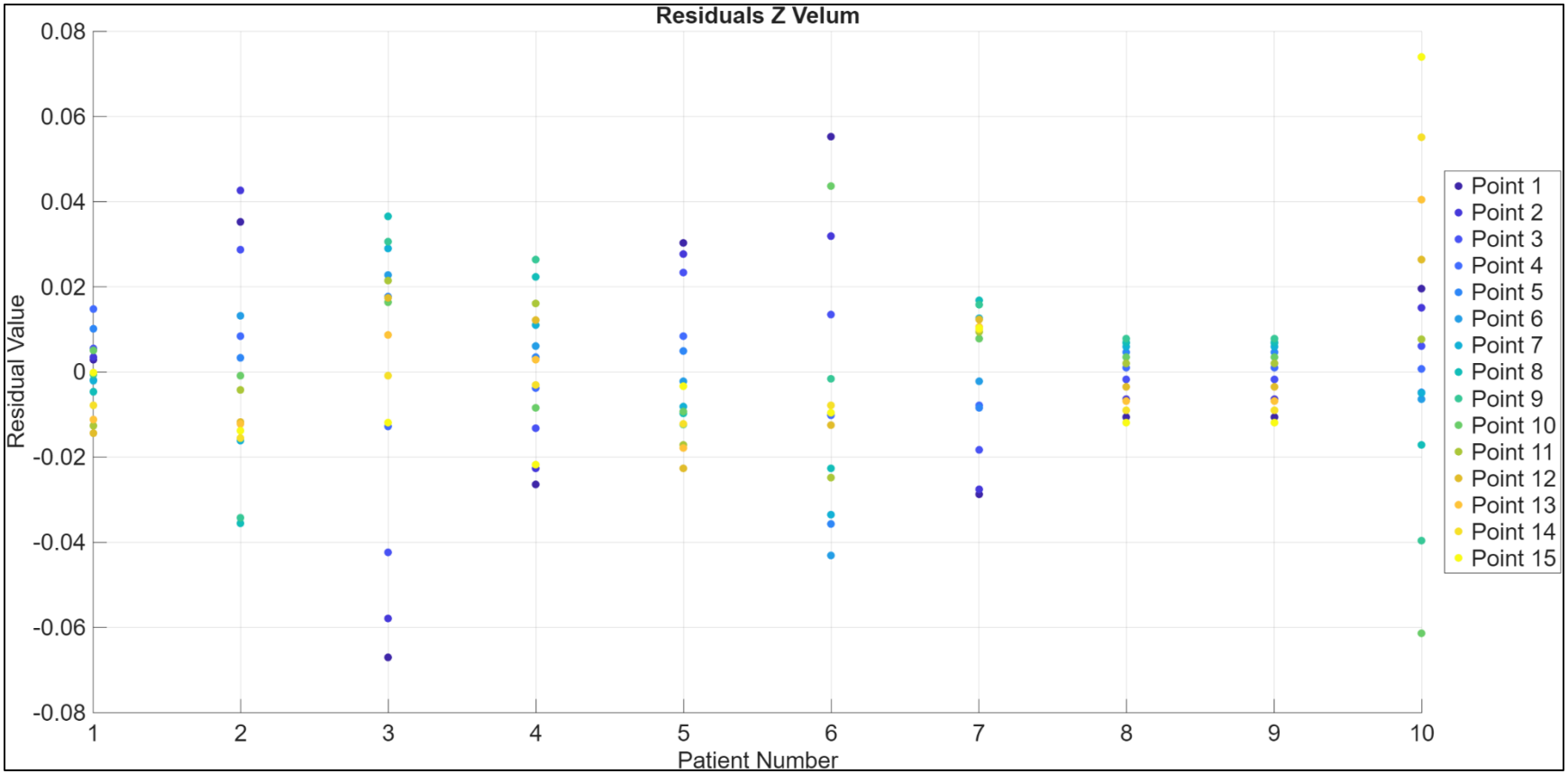

Figure 19. *PCA residuals for the Z direction of the Velum. Points close to 0 indicate a strong fit with points farther away from 0 indicating a weaker fit.*

CHAPTER 5: Discussion and Conclusions

5.1 Interpretation of Results

This study provided the framework for future patient-specific modeling by producing hypothesis-generating results after identifying outlying data in the PC space and developing a method for using PCA in coordinate point analysis. The results from the models broken down into specific anatomical parts provided insight into the anatomical variations found in specific regions. This approach depended on grouping of individual landmark points based upon positive or negative influence on PCs. Points that positively influenced a PC showed correlation between themselves and the vector explaining shape variation. Points with a greater vector magnitude were indicative of a greater influence and highlighted an anatomical region of potential shape variation. Percent explained plots indicated the amount of variation the first three PCs contained for each data set. When there was a wider distribution of variation amongst the PCs, this indicated that variation in that anatomical part was spread out amongst the shape and not stemming from one specific region that could be identified in this study. Score plots showed where the original data would transform to in the reduced PC space. Individual patients were identified as having outlier points in this space and were considered to potentially have shape varying from the rest of the data set at these locations. Residual values were found to provide evidence that shape variation from specific patients could be explained either by system noise or the possibility of actual variation in each anatomical part. This pilot study method is applicable for future analysis in biomedical applications and highlights the need for further repetitions and iterations in patient specific research. The following paragraphs identify the importance of the PCA results for future applications.

In the X directional plane of the velum, points 1-6 and 11-15 positively influenced PC 1, meaning the first six points and last five points selected along the base of the velum explained shape variation found in this specific orientation. PC 1 in the X direction of the velum explained 97.01% of shape variation in this plane, further confirming that points 1-6 and 11-15 are where the most variance occurred in the set. Since PC 2 only explained 1.83% of variation in this coordinate system, the effects that individual points have on this vector were not significant. With no statistical outliers in this set, there was little concern for the PCs being heavily influenced by one specific point. The PCA residuals further confirmed that the first five points selected in the beginning of the set had greater variance than other points as they had a wider distribution pattern. These first 5-6 points were located on the inferior side of the velum, starting on the left side, indicating that the patients may have had different orientations in their velums.

In the Y direction all 15 points had a positive influence on the first PC, which explained 79.59% shape variation, with the first seven points having greater magnitude of influence than the subsequent points. Patient 10 was an outlier on the first PC in the Y direction but showed a positive influence on the first PC so it did not interfere with the direction of the PC vector. Almost all the residual points indicated a strong fit in the Y direction except for point 1 on

patients 2 and 6. These results indicated again that the points picked on the left inferior side of the velum had the strongest influence on shape variation, and patient 10 had the potential to vary the greatest in this orientation. In this system, PC 2 explained 14.21% of the shape variation orthogonal to PC 1, with the points influence being split between positive and negative. In PC 2, the last 5 points had the smallest magnitude of influence on PC 2. These points were selected on the inferior side of the velum and run in the anterior direction towards the tip of the tongue. With these points having less influence on PC 2, it showed that the points on the base of the velum again had more variation between them as they greatly affect the PC vector.

All 15 points in the Z direction had a positive influence on PC 1 with the first 10 points having a greater magnitude of influence. This aligned with the results from the X and Y directions, where the points running along the base of the velum had a larger variation than the five points running anteriorly. In this coordinate system the first PC explained 89.67% of shape variation, again confirming these points strong effects on overall shape variation. The PCA residuals in this data set showed a strong fit, with most of the data centered very close to 0. The Z direction had statistical outliers on PC 3 at patients 6, 7, and 10, but since PC 3 only explained 3.03% of total shape variation, the effects of these outliers on the rest of the data were minimal.

Overall, results in the velum data sets indicated that the greatest shape variation was found along the base of the velum on points 1-10. This area is where the PF is attached to each patient and where a seal is formed during speech and swallowing. Variations in anatomical structure here have the possibility to effect hypernasality. Patient 10 was the only patient in this data set to be a statistical outlier on a first PC (Y direction). This patient was a 13-year-old female with mild hypernasality after PF surgery. These results highlight the need for further investigations into PF placement, velum shape, and resulting VPI symptoms.

The results in the X direction of the LVP were more difficult to interpret than the velum data points. With 78 points on this structure, each point had less influence on a PC than the 15 points of the velum. While PC 1 explained 99.79% of shape variation, the points influence had weaker magnitudes. There were no statistical outliers in the first PC of the X direction either, indicating that variation was spread out among the points and patients in this orientation. The PCA residuals in this set indicated a weak fit among the data set. In this context, a weak fit may have indicated that each patient's coordinates were different than the others, with no patient having greater influence.

Points in the Y direction of the LVP had a split influence on PC 1. There were fewer points positively influencing PC 1, but they had a greater magnitude than the points negatively influencing PC 1. These higher magnitude points included selected landmark points from all three rows of the LVP selection process. This indicated that there was variation spread among the LVP's X direction and not concentrated in one region. The first PC only explained 43.09% of shape variation in this orientation, meaning PC 2 (28.43%) and PC 3 (15.37%) were more significant than in previous cases. With lower percentage of explained variation, this indicated

that the Y direction of the LVP potentially contained more noise or the increase in points may have made it more difficult to explain individual influence. The Y direction had no statistical outliers on any of its PCs, and most of the residual points showed a strong fit with a distribution pattern close to 0. For patients 1, 2, 4, 5, and 10, points in the first row of the LVP landmark points fell outside of the strong fit, meaning there was potential that variation was more significant on the superior posterior region of the muscle.

Like the Y coordinate plane, the Z coordinate plane had a non-uniform influence on the first PC. Points positively influencing PC 1 had greater magnitude than the PCs negatively influencing PC 1 and again contained points from all three rows of LVP point selection. In this data set, the first PC explained only 36.85% of shape variation, with PC 2 and PC 3 explaining 28.06% and 20.48% respectively. These low percentages highlighted the complexity of the LVP point data and made it difficult to pinpoint one region of variation. There is one statistical outlier on PC 1 in the Z direction at patient 10, which indicated a potential shape difference. The residual plots of the Z direction of the LVP also mostly presented close to 0, but patients 1, 2, 4, 5, and 10 had points from the first row of LVP selection that were further away. This agreed with the Y direction residuals, supporting that differences may have occurred in the superior posterior region of the muscle.

The shape variation of the LVP was difficult to pinpoint to one region on the muscle, especially in the X coordinate direction where the data did not show a strong fit. This was potentially caused by the increased number of data points selected for this part. With more coordinates to analyze, each point was less responsible individually for shape variation. There was potentially shape variation identified in patient 10 based on the outlying PC scores in the Z coordinate plane. This was the same patient from the velum outlier with mild hypernasality. Differences in LVP shape could coincide with challenges faced in the velum, making it difficult to lift the velum to form a full seal during speech and swallowing.

Of the 48 points in the X direction of the TVP, most of them had a positive influence on PC 1. Points 1-3 and 18-24 had a negative influence on PC 1. These points with negative influence came from the same region on the muscle. Points 1-3 stemmed from the left segments most anterior corner, while points 18-24 finished the clockwise placement, and ended at the most anterior corner of the same segment. However, the first PC only explained 48.77% of shape variation, indicating that there was only a potential for significant shape variation, not definitively identifying it. The PCA residuals were mostly close to 0, but patients 1, 3, 5, and 7 contained points from the left segment that presented a weaker fit. There was one statistical outlier in the X direction on PC 1, at patient 5. This patient was a 15-year-old male suffering from OSA but did not have hypernasality scores recorded at the time of imaging. This observation introduced questions about potential anatomical differences in those suffering from OSA versus those with hypernasality.

In the Y coordinate plane of the TVP, the points were split in influence on PC 1. In this case there were negative points of influence on PC 1 from both the left and right segments, and since it explained 78.94% of shape variation, this indicated a more spread distribution of responsibility. The Y coordinate plane had one outlier on PC 3, at patient 3. However, PC 3 only explained 6.5% of total shape variation in this data set, so it is unlikely that patient 3 had significant influence on overall variation of the LVP. Most of the PCA residuals indicated a strong fit to the data set. Patients 3, 4, 5, 7, and 10 had a few points from both the left and right segments of the TVP that showed a weaker fit. This supported the spread distribution of influence on PC 1, making it difficult to pinpoint a specific region in the Y coordinate plane that showed significant shape variation.

The Z coordinate plane of the TVP showed a similar spread as the X and Y planes, with about half of the points positively influencing PC 1. Like the Y plane, there were points from multiple sides of both the left and right segments of the TVP that negatively influenced PC 1, again making it difficult to pinpoint a specific region of variation. Additionally, the first PC only explained 54.35% of shape variation, with PC 2 explaining 24.73%. This also made it difficult to assign responsibility to a specific region due to a more spread-out distribution of variation amongst the muscle. Patient 10 was an outlier on PC 2 in the Z direction of the TVP. This concurred with the LVP, and velum sets where a patient with mild hypernasality showed possible differences in anatomical structure. Again, the PCA residual mostly clustered close to 0, with patients 1, 2, 4, 5, and 10 having points mostly from the left segment, with a more spread-out distribution.

Overall, the TVP is like the LVP where it was difficult to identify definitive regions of variation. However, the outliers of patient 3 and patient 10 highlighted potential clinical differences caused by the shape of the TVP. The patients with residuals showing a weaker fit were mostly from the Improved-VPI group, and patient 10. This showed potential differences in the groups and highlights the greater difference in patient 10 from all other patients.

In the X coordinate plane of the palatoglossus muscle, all 24 points had a positive influence on PC 1, which explained 91.36% of shape variation. The points with greater magnitude stem from different regions of the palatoglossus, failing to pinpoint a specific point on the muscle that was mostly responsible for shape variation. However, patient 10 was also an outlier in this data set on PC 1. Since PC 1 explained such a larger percentage of variation, it was possible that patient 10 exhibited significantly different X coordinate points. Patients 1 and 5 were shown to be outliers on PC 2 in this coordinate set but this vector only explained 3.62% of shape variation so it was unlikely for them to influence the overall variation of the palatoglossus. The PCA residuals for this set showed regions of strong and weak fit, distributed amongst the structures and all patients. There were points from both the left and right segments of the palatoglossus that were distributed farther away from 0, again making a specific region of variation difficult to identify.

The Y direction of the palatoglossus showed all points except 1 and 7 positively influenced PC 1. These two points were from the left segment of the palatoglossus, but from opposite faces of the muscle. Their magnitude of negative influence was much weaker than the points with a positive influence and PC 1 only explained 38.66% of shape variation in this data set so this did not necessarily infer significant variation at points 1 and 7. The second PC explained the next 22.74% of shape variation in the Y plane but the points were again split on positive and negative influence, making it difficult to confirm a specific region of strong variation. There were no statistical outlying patients in the Y coordinate plane and the PCA residuals mostly indicated a strong fit. There were a few points with a wider distribution, but this was spread amongst all patients except for patient 7. This failed to identify a specific patient with more significant shape variation.

Like the Y coordinate plane, the Z coordinate plane had mostly positive influence on PC 1. In this set, points 5, 6, and 16-18 had negative influences. Points 5 and 6 were from the left segment of the palatoglossus, while points point 16-18 were from the right segment. While this indicated the potential for specific regions of variation, the first PC only explained 39.55% of total shape variation in this set, so it did not provide a strong argument. The Z coordinate plane also did not have any outliers at specific patients, again failing to pinpoint exact regions of variation. The PCA residuals also failed to pinpoint specific regions of variation or specific patients, as most of the points were close to 0, with 1-2 points on each patient showing a weaker fit.

The strongest argument to be made in the palatoglossus data sets was patient 10 being an outlier in the X coordinate plane. In the Y and Z planes, the first PCs did not explain most of the shape variation, and there were no outliers identified in these planes. If patient 10 also had different anatomical characteristics in the palatoglossus, this could have exacerbated the negative effects from shape variation found in previous muscles.

The X coordinates of the pharyngeal wall had a split distribution on influence on PC 1. Points 1-6 had a positive influence on the first PC which explained 99.98% of shape variation in this coordinate plane. Point 6 had the greatest magnitude of influence on PC 1 which was a point located about halfway down the pharyngeal wall. Patients 3 and 5 were shown to be statistical outliers in this coordinate plane and were both patients from the Improved-VPI group. Patient 3 was an 8-year-old male experiencing minimal hypernasality after PF surgery and patient 5 was the 15-year-old male experiencing OSA. Potential differences in the shape of the pharyngeal wall could impact where the PF contacts wall and its ability to fully seal the pharyngeal cavity. The PCA residuals showed a weak fit amongst the data across all points and patients. This potentially highlighted differences in shape or could be caused by other limitations of the study such as segmentation issues from MRI visibility challenges.

The Y direction of the pharyngeal wall showed a distinct correlation between point number and influence on PC 1. Magnitude of influence increased sequentially, meaning as points were picked further down the wall, they had a greater influence on PC 1. In this coordinate set the first PC

explained 82.62% of shape variation, supporting the likelihood that variation occurred further down the pharyngeal wall. Patient 5 was an outlier on the second PC in this set, but PC 2 was only responsible for 16.56% of total shape variation so it was unlikely to affect the overall system. Like the X coordinates, the Y coordinates residuals showed a weak fit among the data set. This was again potentially explained by difficulties with segmentation and MRI visibility.

Inverse to the Y coordinate system, the points in the Z coordinate system of the pharyngeal wall decreased magnitude of positive influence on PC 1 in sequential order. As points were picked further down the wall, they had less influence on overall variation in the Z direction. The first PC explained 91.78% of shape variation and the Z coordinate system had no statistical outliers, so a specific patient could not be identified as a significant influence on variation. Unlike the X and Y coordinate system, the Z PCA residuals mostly showed a strong fit among the data set. Patients 1 and 2 had one point that fell further away from 0, and patient 5 had 4 points that were further away from 0. These points could have had a weak fit due to true variance or could stem from segmenting issues previously mentioned.

The pharyngeal wall contained the constrictor muscles, which contract during speech and swallowing, assisting in the seal of the pharyngeal port. In the X direction it is possible that patients 3 and 5 had a shape variation that may make their anatomy function better than those patients in the VPI group. However, this is a preliminary observation that would need to be further evaluated with constrictor muscle specific studies using a larger data set with more homogeneous patient groups. This observation was used to support the use of PCA in identifying data points that vary from an overall set but cannot be interpreted as a definitive correlation between shape and clinical outcomes.

The combined data sets provided a more generalized set of results with 175 points used in each coordinate set. The X direction showed points 56 and 82 (both from the LVP) had a strong influence on PC 1, while all other points have a weaker influence. In this set, the first PC explained 95.11% of shape variation in the X direction, so it is possible that points 56 and 82 had significant influence. However, the residual plot showed a weak fit among the data, with almost no points indicating a strong correlation. This was possibly due to the number of points being analyzed in this set, with each one impacting the mean shape. Patients 2 and 3 were shown to be statistical outliers in the X coordinate direction, and both were from the Improved-VPI group. Patient 2 was a 7-year-old female experiencing minimal hypernasality and patient 3 was an 8-year-old male also experiencing minimal hypernasality. While not definitive, these results alluded to the possibility of anatomical characteristics coinciding with clinical outcomes.

In the Y coordinate plane combined set, all 175 points had a positive influence on PC 1. This indicated that variation in the Y direction was spread among the different anatomical parts in the system and did not pinpoint a specific region of greater variation. The first PC in this set explained 93.84% of shape variation, confirming that each point had individual influence on the vector. There was one statistical on PC 3, from patient 1, however, PC 3 only explained 1.55% of

shape variation so it was unlikely that patient 1 was overly influential on the mean shape. The PCA residuals in the Y direction contained many points showing a strong fit but contained regions of weak fit as well. The points of weaker fit stemmed from different anatomical parts in the system and from different patients, failing to pinpoint a specific region of weakness.

The combined Z coordinates showed very similar results to the combined Y coordinates with all points positively influencing PC 1, with no point showing extremely high magnitude. With PC 1 explaining nearly all variation in this set (99.05%), there was not a distinct region of variation in the Z plane. There were no statistical outliers in the Z coordinate plane, also failing to identify a specific patient with increased variation in the system. The residual plots for this set were mostly close to 0, with patients 1, 2, 6, 7, and 9 having 3-5 total points with a weaker fit. Overall, this indicated that variation was evenly distributed amongst points in the Z coordinate plane across the entire pharyngeal system and did not identify a specific region of variation.

The X coordinates highlighted the possibility for overall variation in patients 2 and 3, but these results were not confirmed in the Y and Z directions. There was also a suggestion that from the X coordinate system that the LVP may have been more significantly responsible for overall shape variation, but again, was not confirmed in the Y and Z coordinate planes. These results generated the need for further analysis in coordinate system models.

The results from the individual part models provided greater insight into anatomical variations than the combined coordinate sets as they allowed for focus on smaller regions. In the velum, LVP, TVP, and pharyngeal wall model's patient 10 arose as a potential outlier but was not identified in the combined coordinate sets. When the models were broken down into part specific sets, it allowed each point to have greater influence on a mean shape, illuminating more specific regions of shape variation. Patient 10 was a member of the VPI group and experienced mild hypernasality after PF placement. These results highlighted the need for further, anatomy specific research, without confounding variables presented in this study.

Patient 3 also arose as an outlier in more than one case. In the TVP, pharyngeal wall, and combined X coordinates, this patient demonstrated variation from the mean. As a member of the Improved-VPI group, with minimal hypernasality, these results indicated the potential for favorable anatomical shapes and further support the need for more extensive research.

5.2 Limitations

The most significant limitation of this study is the problem of small numbers [55], created by the nature of this pilot study. The results, while informative, highlighted the need for replication using larger sample sizes. Many patients were deemed an outlier in at least one coordinate direction. With a larger sample size, each patient will not have such a large effect on the mean shape, which may lead to more definitive results.

Confounding variables arise from the data set itself. With patients ranging from 4-26 years old and one patient having 22q11.2 deletion syndrome, there are likely anatomical differences based

on human developmental stages. With the addition of diverse VPI symptoms (OSA and varying levels of hypernasality) in this sample data set, this study can only be interpreted as exploratory and not as identifying of true shape variation linked to clinical outcomes. The different subtypes of clefts were also not factored into this small data set. Including patients who began with drastically different anatomical complications made it difficult to determine post-operative shape differences that may have affected VPI symptoms.

The convenience sample of MRI images provide a significant limitation in this study. A larger interventional study would have pre-operative and post-operative MRIs which would be able to account for the anatomical differences among patients. It is possible that some shape differences were created by the surgery itself or during the healing process.

Other limitations include system selection noise from hand-picking landmark points on the three-dimensional models. Using an algorithm to uniformly select points based on spacing or proportions, or inter-rater intra-rater methods in future studies would lead to a more reliable data set, especially in anatomical parts that vary drastically from person to person.

The N-point registration produced another limitation in this study. This approach was appropriate for a small sample size with no reference figure but did not provide the same rigor as Procrustes alignment or an atlas-based method. The registration against Patient 1 was done arbitrarily to minimize translational and rotational effects in this small data set, but registration against a reference figure would provide more confidence in the registered shapes.

To combat variation from different sizes, scaling was performed on the coordinate points, as natural differences between pediatric and adult patients, and male and female patients are likely. Separating the patients by sex in this study would have made the problem of small numbers more drastic, so they were kept in one set. However, scaling each patient based on a mean shape was a provisional coordinate standardization again based on the lack of a specified reference figure. This limitation meant that PCA results were only able to be interpreted as exploratory patterns, and not true size estimates.

The outlier analysis was also interpreted as exploratory descriptors of variation due to the above-mentioned limitations from the data set. These outlying points did not consider differences caused by age, sex, or cleft subtype.

Finally, the residual analysis was only able to provide patterns of strong and weak fit. A distinct value of acceptable and unacceptable could not be chosen as residuals are context dependent and extremely variable from study to study. To identify a smaller range of acceptable residuals, a larger data set with more confirmatory results would be needed.

5.3 Future Directions of Research

In future work, the potential use of PCA as an efficient and economical approach to identifying anatomical differences in groups of patients could be confirmed using the framework provided by this study. This pilot study established 3D MRI as a valuable method for anatomical imaging supported by PCA to segment and construct accurate models of regions of interest.

Future works should stratify by age and sex specific subject groups to minimize natural anatomical differences from these categories. Complications arising from different subtypes of clefts should also be considered when obtaining more homogenous patient sets. Future data sets should be significantly larger so appropriate statistical methods can be used for more definitive outlier results. Future data sets should also include pre-operative and post-operative imaging for comparison, to eliminate concerns of shape variation occurring due to the surgical process or during healing.

During the PCA process, more selective methods should be utilized during the point picking segment. Advanced software includes algorithm-based abilities to ensure points are at corresponding locations across patients. The use of inter-rater intra-rater validation would also increase confidence that points were anatomically equal across patients. During the registration of points, a reference figure with known desired anatomy should be used instead of a patient selected arbitrarily from the data set. This study did not have a reference figure for use, but such a reference would have built more confidence in the translated points. The reference figure needed for future work should also be used during scaling applications. Scaling against a mean was done in this study due to the lack of a reference figure, but this would have provided additional confidence that variations from age and sex were accounted for.

Future statistical methods from larger data sets should include mean and standard deviation methods in addition to the IQR method. This was not possible in this study due to the problem of small numbers, which prevented statistical claims from being definitive. Additionally, the use of residuals should include a specified cut-off value for acceptable and unacceptable values. This would provide more definitive arguments for noise vs shape variation debates.

5.4 Conclusions

This study generated a reusable methodology for testing hypotheses that could be instrumental in future explorations into anatomical effects on surgical outcomes. Identifying the potential for outlying coordinate points shows the value of PCA in biomedical applications such as optimizing surgical intervention approaches. The possibility of linking patient specific anatomy to clinical outcomes lays important framework for further modeling research, with the potential to implement statistical methods into future pre-operative planning projects.

If eventually implemented into clinical spaces, using PCA to identify anatomical shape variations could assist surgeons in a personalized PF placement. This has the potential to decrease the number of children experiencing persistent VPI, decrease repetitive surgeries, and improve

quality of life for thousands every year. While this exploratory coordinate point pilot analysis requires repetition with much larger sample sizes, it lays the foundation for further research in anatomical modeling.

REFERENCES

[1] A. Babai and M. Irving, “Orofacial Clefts: Genetics of Cleft Lip and Palate,” *Genes*, vol. 14, no. 8, p. 1603, Aug. 2023, doi: 10.3390/genes14081603.

[2] E. J. Leslie and M. L. Marazita, “Genetics of cleft lip and cleft palate,” *Am. J. Med. Genet. C Semin. Med. Genet.*, vol. 163, no. 4, pp. 246–258, 2013, doi: 10.1002/ajmg.c.31381.

[3] J. J. Cubitt, A. M. Hodges, K. M. Van Lierde, and M. C. Swan, “Global Variation in Cleft Palate Repairs: An Analysis of 352,191 Primary Cleft Repairs in Low- to Higher-Middle-Income Countries,” *Cleft Palate Craniofacial J.*, vol. 51, no. 5, pp. 553–556, Sep. 2014, doi: 10.1597/12-270.

[4] D. H. Rochlin, L. W. Ma, C. C. Sheckter, and H. P. Lorenz, “Out-of-Pocket Costs and Provider Payments in Cleft Lip and Palate Repair,” *Ann. Plast. Surg.*, vol. 88, no. 4, p. S343, May 2022, doi: 10.1097/SAP.0000000000003081.

[5] T. O. Abdurrazaq, A. O. Micheal, A. W. Lanre, O. M. Olugbenga, and L. L. Akin, “Surgical outcome and complications following cleft lip and palate repair in a teaching hospital in Nigeria,” *Afr. J. Paediatr. Surg. AJPS*, vol. 10, no. 4, pp. 345–357, 2013, doi: 10.4103/0189-6725.125447.

[6] S. R. Sullivan, E. M. Marrinan, and J. B. Mulliken, “Pharyngeal flap outcomes in nonsyndromic children with repaired cleft palate and velopharyngeal insufficiency,” *Plast. Reconstr. Surg.*, vol. 125, no. 1, pp. 290–298, Jan. 2010, doi: 10.1097/PRS.0b013e3181c2a6c1.

[7] A. D. Buys Roessingh *et al.*, “Palatal cleft: Results after 18 years, one surgeon, one primary technique,” *Otorhinolaryngol.-Head Neck Surg.*, vol. 5, no. 2, 2020, doi: 10.15761/OHNS.1000235.

[8] J. L. Williams *et al.*, “Velopharyngeal Gap Size During Sustained Vowel Production Correlates With Perceptual Ratings of Hypernasality in Connected Speech,” 12:00:00, doi: 10.1044/2024_JSLHR-24-00221.

[9] M. E. Tavsanli, A. Zeynalova, and M. Seckin, “The effect of pharyngeal structures on the severity of obstructive sleep apnea,” *Sleep Breath.*, vol. 28, no. 2, pp. 849–857, May 2024, doi: 10.1007/s11325-023-02973-3.

[10] D. H. Rosero Salazar, R. Grewal, A. Vimawala, D. F. Leotta, S. R. Levendovszky, and Z.-J. Liu, “Pharyngeal airway dimensions and adipose distribution in the minipig,” *J. Oral*

Biol. Craniofacial Res., vol. 15, no. 1, pp. 77–83, Jan. 2025, doi: 10.1016/j.jobcr.2024.12.004.

[11] J. L. Perry *et al.*, "Morphology of the Musculus Uvulae In Vivo Using MRI and 3D Modeling Among Adults With Normal Anatomy and Preliminary Comparisons to Cleft Palate Anatomy," *Cleft Palate. Craniofac. J.*, Feb. 2019, doi: 10.1177/1055665619828226.

[12] J. L. Perry, D. P. Kuehn, and B. P. Sutton, "Morphology of the Levator Veli Palatini Muscle Using Magnetic Resonance Imaging," *Cleft Palate Craniofacial J.*, vol. 50, no. 1, pp. 64–75, Jan. 2013, doi: 10.1597/11-125.

[13] J. L. Perry, T. D. Snodgrass, I. R. Gilbert, J. L. Williams, D. J. Singh, and T. J. Sitzman, "The Levator Veli Palatini: Are all Segments Created Equal?," *Cleft Palate Craniofacial J.*, Aug. 2024, doi: 10.1177/10556656241271666.

[14] J. L. Perry, B. P. Sutton, D. P. Kuehn, and J. K. Gamage, "Using MRI for Assessing Velopharyngeal Structures and Function," *Cleft Palate Craniofacial J.*, vol. 51, no. 4, pp. 476–486, Jul. 2014, doi: 10.1597/12-083.

[15] K. N. Mason, B. Hanson, and J. S. Black, "Measurement Matters: MRI Analysis of Differing Anatomic Measurement Techniques for Velar Length and the Velopharyngeal Needs Ratio," *Plast. Reconstr. Surg. – Glob. Open*, vol. 12, no. 2, p. e5617, Feb. 2024, doi: 10.1097/GOX.0000000000005617.

[16] J. S. Chauhan and S. Sharma, "Modified Uvuloplasty for Achieving Aesthetically Desired Uvula in Cleft Palate Repair," *J. Maxillofac. Oral Surg.*, vol. 21, no. 2, pp. 454–459, Jun. 2022, doi: 10.1007/s12663-020-01478-w.

[17] E. B. Katzel *et al.*, "Speech Outcomes After Clinically Indicated Posterior Pharyngeal Flap Takedown," *Ann. Plast. Surg.*, vol. 77, no. 4, pp. 420–424, Oct. 2016, doi: 10.1097/SAP.0000000000000632.

[18] J. L. Perry, "Anatomy and physiology of the velopharyngeal mechanism," *Semin. Speech Lang.*, vol. 32, no. 2, pp. 83–92, May 2011, doi: 10.1055/s-0031-1277712.

[19] J. L. Perry *et al.*, "Variations in velopharyngeal structure in adults with repaired cleft palate," *Cleft Palate-Craniofacial J. Off. Publ. Am. Cleft Palate-Craniofacial Assoc.*, vol. 55, no. 10, pp. 1409–1418, Nov. 2018, doi: 10.1177/1055665617752803.

[20] P.-K. Lu, "Modified surgical procedure for velopharyngeal closure in adults: A preliminary report," *J. Oral Maxillofac. Surg.*, vol. 45, no. 6, pp. 556–559, Jun. 1987, doi: 10.1016/S0278-2391(87)80023-X.

[22] T. N. George, K. J. Kotlarek, D. P. Kuehn, B. P. Sutton, and J. L. Perry, “Differences in the Tensor Veli Palatini Between Adults With and Without Cleft Palate Using High-Resolution 3-Dimensional Magnetic Resonance Imaging,” *Cleft Palate Craniofacial J.*, vol. 55, no. 5, pp. 697–705, May 2018, doi: 10.1177/1055665617752802.

[23] J. L. Perry *et al.*, “Differences in the Tensor Veli Palatini Muscle and Hearing Status in Children With and Without 22q11.2 Deletion Syndrome,” *Cleft Palate Craniofacial J.*, vol. 57, no. 3, pp. 302–309, Mar. 2020, doi: 10.1177/1055665619869142.

[24] S. Power and K. J. Kotlarek, “An Exploratory Investigation of the Palatoglossus Muscle in Children Using Magnetic Resonance Imaging,” *J. Speech Lang. Hear. Res.*, vol. 65, no. 11, pp. 4151–4158, Nov. 2022, doi: 10.1044/2022_JSLHR-22-00303.

[25] R. Anandan, K. C. Lakshmi, A. Ganesan, and Y. AniyanK, “Assessment of pharyngeal airway space with MRI In oral submucous fibrosis: A cross-sectional observational study,” *J. Oral Biol. Craniofacial Res.*, vol. 14, no. 6, pp. 669–675, Nov. 2024, doi: 10.1016/j.jobcr.2024.09.003.

[26] C. J. Boyd, L. Slowikowski, R. L. Flores, and L. A. Schuster, “Anatomy of cleft lip and palate,” in *Cleft and Craniofacial Orthodontics*, John Wiley & Sons, Ltd, 2023, pp. 61–73. doi: 10.1002/9781119778387.ch5.

[27] T. D. Snodgrass, J. L. Perry, and T. J. Sitzman, “Development and evaluation of a training program for implementation of velopharyngeal MRI in the clinical setting,” *Pediatr. Radiol.*, vol. 55, no. 5, pp. 965–975, May 2025, doi: 10.1007/s00247-025-06186-6.

[28] T. J. Sitzman, J. L. Williams, D. J. Singh, M. Temkit, T. D. Snodgrass, and J. L. Perry, “Magnetic Resonance Imaging of the Velopharynx: Clinical Findings in Patients with Velopharyngeal Insufficiency,” *Plast. Reconstr. Surg.*, vol. 153, no. 6, p. 1155e, Jun. 2024, doi: 10.1097/PRS.0000000000010798.

[29] S. Das, *Optimizing Prediction of MGMT Promoter Methylation from MRI Scans using Adversarial Learning*. 2022. doi: 10.48550/arXiv.2201.04416.

[30] T. Tran, J. Perry, S. Blemker, and K. Mason, “Simulation of Velopharyngeal Biomechanics Identifies Differences in Sphincter Pharyngoplasty Outcomes: A Matched Case-Control Study,” *Cleft Palate-Craniofacial J. Off. Publ. Am. Cleft Palate-Craniofacial Assoc.*, vol. 61, no. 2, pp. 339–349, Feb. 2024, doi: 10.1177/10556656221122634.

[31] F. Ambellan, H. Lamecker, C. von Tycowicz, and S. Zachow, “Statistical Shape Models: Understanding and Mastering Variation in Anatomy,” *Adv. Exp. Med. Biol.*, vol. 1156, pp. 67–84, 2019, doi: 10.1007/978-3-030-19385-0_5.

[32] C. Klop, “A three-dimensional statistical shape model of the growing mandible,” *Sci. Rep.*, vol. 11, no. 1, p. 18843, Sep. 2021, doi: 10.1038/s41598-021-98421-x.

[33] H. van der Wel, B. Qiu, F. K. L. Spijkervet, J. Jansma, R. H. Schepers, and J. Kraeima, “Morphological Variation of the Mandible in the Orthognathic Population—A Morphological Study Using Statistical Shape Modelling,” *J. Pers. Med.*, vol. 13, no. 5, p. 854, May 2023, doi: 10.3390/jpm13050854.

[34] Materialise, *Matreialise Mimics Core 27.0*. (2026).

[35] N. Rodriguez-Florez *et al.*, “Statistical shape modelling to aid surgical planning: associations between surgical parameters and head shapes following spring-assisted cranioplasty,” *Int. J. Comput. Assist. Radiol. Surg.*, vol. 12, no. 10, pp. 1739–1749, Oct. 2017, doi: 10.1007/s11548-017-1614-5.

[36] K. Bettens, L. Bruneel, Y. Maryn, M. De Bodt, A. Luyten, and K. M. Van Lierde, “Perceptual evaluation of hypernasality, audible nasal airflow and speech understandability using ordinal and visual analogue scaling and their relation with nasalance scores,” *J. Commun. Disord.*, vol. 76, pp. 11–20, Nov. 2018, doi: 10.1016/j.jcomdis.2018.07.002.

[37] A. S. Lam, E. M. Kirkham, J. P. Dahl, S. L. Kinter, J. A. Perkins, and K. C. Sie, “Speech Outcomes After Sphincter Pharyngoplasty for Velopharyngeal Insufficiency,” *The Laryngoscope*, vol. 131, no. 6, pp. E2046–E2052, Jun. 2021, doi: 10.1002/lary.29189.

[38] “Figure 1. The anatomical position, with three reference planes and six...,” ResearchGate. Accessed: Mar. 17, 2026. [Online]. Available: https://www.researchgate.net/figure/The-anatomical-position-with-three-reference-planes-and-six-fundamental-directions-24_fig1_355203662

[39] Materialise, *3-matic*. Leuven, Belgium.

[40] R. Wu, X. Jin, X. Yang, P. Yu, and Z. Qi, “Comparative Study of Three-Dimensional Volume Measurement for Facial Fat Grafting,” *J. Craniofac. Surg.*, vol. 32, no. 4, p. 1341, Jun. 2021, doi: 10.1097/SCS.0000000000007395.

[41] N. J. Chargo *et al.*, “Keel bone differences in laying hens housed in enriched colony cages,” *Poult. Sci.*, vol. 98, no. 2, pp. 1031–1036, Feb. 2019, doi: 10.3382/ps/pey421.

[42] The MathWorks Inc., “MATLAB Version R2024b,” 2024.

[43] J. E. Rood *et al.*, “Towards a Common Coordinate Framework for the Human Body,” *Cell*, vol. 179, no. 7, pp. 1455–1467, Dec. 2019, doi: 10.1016/j.cell.2019.11.019.

[44] R. L. Lawrence, A. M. Ellingson, and P. M. Ludewig, “Validation of single-plane fluoroscopy and 2D/3D shape-matching for quantifying shoulder complex kinematics,” *Med. Eng. Phys.*, vol. 52, pp. 69–75, Feb. 2018, doi: 10.1016/j.medengphy.2017.11.005.

[45] I. T. Jolliffe and J. Cadima, “Principal component analysis: a review and recent developments,” *Philos. Transact. A Math. Phys. Eng. Sci.*, vol. 374, no. 2065, p. 20150202, Apr. 2016, doi: 10.1098/rsta.2015.0202.

[46] P. de B. Harrington, N. E. Vieira, J. Espinoza, J. K. Nien, R. Romero, and A. L. Yergey, “Analysis of variance–principal component analysis: A soft tool for proteomic discovery,” *Anal. Chim. Acta*, vol. 544, no. 1, pp. 118–127, Jul. 2005, doi: 10.1016/j.aca.2005.02.042.

[47] K. Lange, “Singular Value Decomposition,” in *Numerical Analysis for Statisticians*, K. Lange, Ed., New York, NY: Springer, 2010, pp. 129–142. doi: 10.1007/978-1-4419-5945-4_9.

[48] A. G. Akritas and G. I. Malaschonok, “Applications of singular-value decomposition (SVD),” *Math. Comput. Simul.*, vol. 67, no. 1, pp. 15–31, Sep. 2004, doi: 10.1016/j.matcom.2004.05.005.

[49] “pca - Principal component analysis of raw data - MATLAB.” Accessed: Mar. 18, 2026. [Online]. Available: https://www.mathworks.com/help/stats/pca.html

[50] Z. Zhang and A. Castelló, “Principal components analysis in clinical studies,” *Ann. Transl. Med.*, vol. 5, no. 17, p. 351, Sep. 2017, doi: 10.21037/atm.2017.07.12.

[51] M. Hubert, P. J. Rousseeuw, and K. Vanden Branden, “ROBPCA: A New Approach to Robust Principal Component Analysis,” *Technometrics*, vol. 47, no. 1, pp. 64–79, Feb. 2005, doi: 10.1198/004017004000000563.

[52] S. Ahmad, Z. Lin, S. A. Abbasi, and M. Riaz, “On Efficient Monitoring of Process Dispersion using Interquartile Range,” *Open J. Appl. Sci.*, vol. 02, no. 04, pp. 39–43, 2012, doi: 10.4236/ojapps.2012.24B010.

[53] L. Greco, G. Luta, and R. Wilcox, “On testing the equality between interquartile ranges,” *Comput. Stat.*, vol. 39, no. 5, pp. 2873–2898, Jul. 2024, doi: 10.1007/s00180-023-01415-8.

[54] H.-Y. Kim, “Statistical notes for clinical researchers: Nonparametric statistical methods: 1. Nonparametric methods for comparing two groups,” *Restor. Dent. Endod.*, vol. 39, no. 3, pp. 235–239, Aug. 2014, doi: 10.5395/rde.2014.39.3.235.

[55] R. K. Guy, “The Strong Law of Small Numbers,” *Am. Math. Mon.*, vol. 95, no. 8, pp. 697–712, Oct. 1988, doi: 10.1080/00029890.1988.11972074.

[56] P. J. Rousseeuw and M. Hubert, “Robust statistics for outlier detection,” *WIREs Data Min. Knowl. Discov.*, vol. 1, no. 1, pp. 73–79, 2011, doi: 10.1002/widm.2.

[57] R. G. Brereton, “Introduction to residuals and estimation by principal components analysis,” *J. Chemom.*, vol. 36, no. 10, p. e3407, 2022, doi: 10.1002/cem.3407.

[58] “pcares - Residuals from principal component analysis - MATLAB.” Accessed: Mar. 24, 2026. [Online]. Available: https://www.mathworks.com/help/stats/pcares.html

[59] M. Straume and M. L. Johnson, “[5] Analysis of Residuals: Criteria for determining goodness-of-fit,” in *Methods in Enzymology*, vol. 210, Elsevier, 1992, pp. 87–105. doi: 10.1016/0076-6879(92)10007-Z.

[60] N. J.Salkind, “Residuals,” in *Encyclopedia of Measurement and Statistics*, Sage Publications, Inc., 2007, pp. 839–840. doi: 10.4135/9781412952644.

Appendix A: MATLAB CODE

```
% Appendix A: Matlab Code
% Author: Taylor Falk
% Last Date Updated: 3-26-2026

% Example of creation of original matrices for each part of each patient
% Velum coordinates for patient 1 in MxN matrix
% M = Point number
% N = x, y, z coordinate plane

NV1_Velum = [10.723 -21.1989     -75.6837
8.0318 -20.5219     -75.5392
5.3963 -19.455      -75.2941
2.9304 -18.3529     -75.7798
0.4368 -19.0003     -75.1102
-2.2117      -19.6782     -74.2734
-4.8824      -19.4716     -74.1011
-7.3078      -19.5741     -74.066
-10.0415     -20.5827     -75.1752
-12.6507     -20.9368     -76.3653
-2.0557      -22.1903     -73.0254
-1.9022      -24.7794     -71.5511
-1.8443      -26.9119     -70.1145
-1.7083      -29.1155     -68.6368
-1.5611      -31.4912     -67.2873];

% Transpose all matrices to flip rows and columns.
% In PCA, Rows are observances and columns are variables.
% Variables = point number.
% observances = patient number

NV1_Velum_Transposed = NV1_Velum';
NV1_LVP_Transposed = NV1_LVP';
NV1_TVP_Transposed = NV1_TVP';
NV1_PG_Transposed = NV1_PG';
NV1_Wall_Transposed = NV1_Wall';
NV2_Velum_Transposed = NV2_Velum';
NV2_LVP_Transposed = NV2_LVP';
NV2_TVP_Transposed = NV2_TVP';
NV2_PG_Transposed = NV2_PG';
NV2_Wall_Transposed = NV2_Wall';
NV3_Velum_Transposed = NV3_Velum';
NV3_LVP_Transposed = NV3_LVP';
NV3_TVP_Transposed = NV3_TVP';
NV3_PG_Transposed = NV3_PG';
NV3_Wall_Transposed = NV3_Wall';
NV4_Velum_Transposed = NV4_Velum';
NV4_LVP_Transposed = NV4_LVP';
NV4_TVP_Transposed = NV4_TVP';
NV4_PG_Transposed = NV4_PG';
NV4_Wall_Transposed = NV4_Wall';
NV5_Velum_Transposed = NV5_Velum';
NV5_LVP_Transposed = NV5_LVP';
NV5_TVP_Transposed = NV5_TVP';
NV5_PG_Transposed = NV5_PG';
NV5_Wall_Transposed = NV5_Wall';
```

```
V1_Velum_Transposed = V1_Velum';
V1_LVP_Transposed = V1_LVP';
V1_TVP_Transposed = V1_TVP';
V1_PG_Transposed = V1_PG';
V1_Wall_Transposed = V1_Wall';
V2_Velum_Transposed = V2_Velum';
V2_LVP_Transposed = V2_LVP';
V2_TVP_Transposed = V2_TVP';
V2_PG_Transposed = V2_PG';
V2_Wall_Transposed = V2_Wall';
V3_Velum_Transposed = V3_Velum';
V3_LVP_Transposed = V3_LVP';
V3_TVP_Transposed = V3_TVP';
V3_PG_Transposed = V3_PG';
V3_Wall_Transposed = V3_Wall';
V4_Velum_Transposed = V4_Velum';
V4_LVP_Transposed = V4_LVP';
V4_TVP_Transposed = V4_TVP';
V4_PG_Transposed = V4_PG';
V4_Wall_Transposed = V4_Wall';
V5_Velum_Transposed = V5_Velum';
V5_LVP_Transposed = V5_LVP';
V5_TVP_Transposed = V5_TVP';
V5_PG_Transposed = V5_PG';
V5_Wall_Transposed = V5_Wall';

% For each part, combine all X, all Y, and all Z into PxM separate matrices
% P = patient number
% M = point number
% Find average of combined data for scaling
% Scale each point around the mean
% For velum data sets:

allX_Velum = [NV1_Velum_Transposed(1,:);
    NV2_Velum_Transposed(1,:);
    NV3_Velum_Transposed(1,:);
    NV4_Velum_Transposed(1,:);
    NV5_Velum_Transposed(1,:);
    V1_Velum_Transposed(1,:);
    V2_Velum_Transposed(1,:);
    V3_Velum_Transposed(1,:);
    V4_Velum_Transposed(1,:);
    V5_Velum_Transposed(1,:)];

meanXVelum = mean(allX_Velum);
scaledX_Velum = allX_Velum./meanXVelum;

% PCA for X, Y, and Z coordinate sets of the velum
[coeff_XV, score_XV, latent_XV, tsquared_XV, explained_XV, mu_XV] =
pca(scaledX_Velum);
[coeff_YV, score_YV, latent_YV, tsquared_YV, explained_YV, mu_YV] =
pca(scaledY_Velum);
[coeff_ZV, score_ZV, latent_ZV, tsquared_ZV, explained_ZV, mu_ZV] =
pca(scaledZ_Velum);

% PCA Residual Calculations for Velum Data Sets
residualXVelum = pcares(scaledX_Velum,1);
```

```
residualYVelum = pcares(scaledY_Velum,1);
residualZVelum = pcares(scaledZ_Velum,1);

%IQR for X Coordinate plane of the Velum
XVQ1 = quantile(score_XV, 0.25);
XVQ3 = quantile(score_XV, 0.75);
IQRXV = iqr(score_XV);
XVlowerlimit = XVQ1 - (1.5 * IQRXV);
XVupperlimit = XVQ3 + (1.5 * IQRXV);
XVoutliers = score_XV(score_XV < XVlowerlimit | score_XV > XVupperlimit);
```

Appendix B: Additional Figures

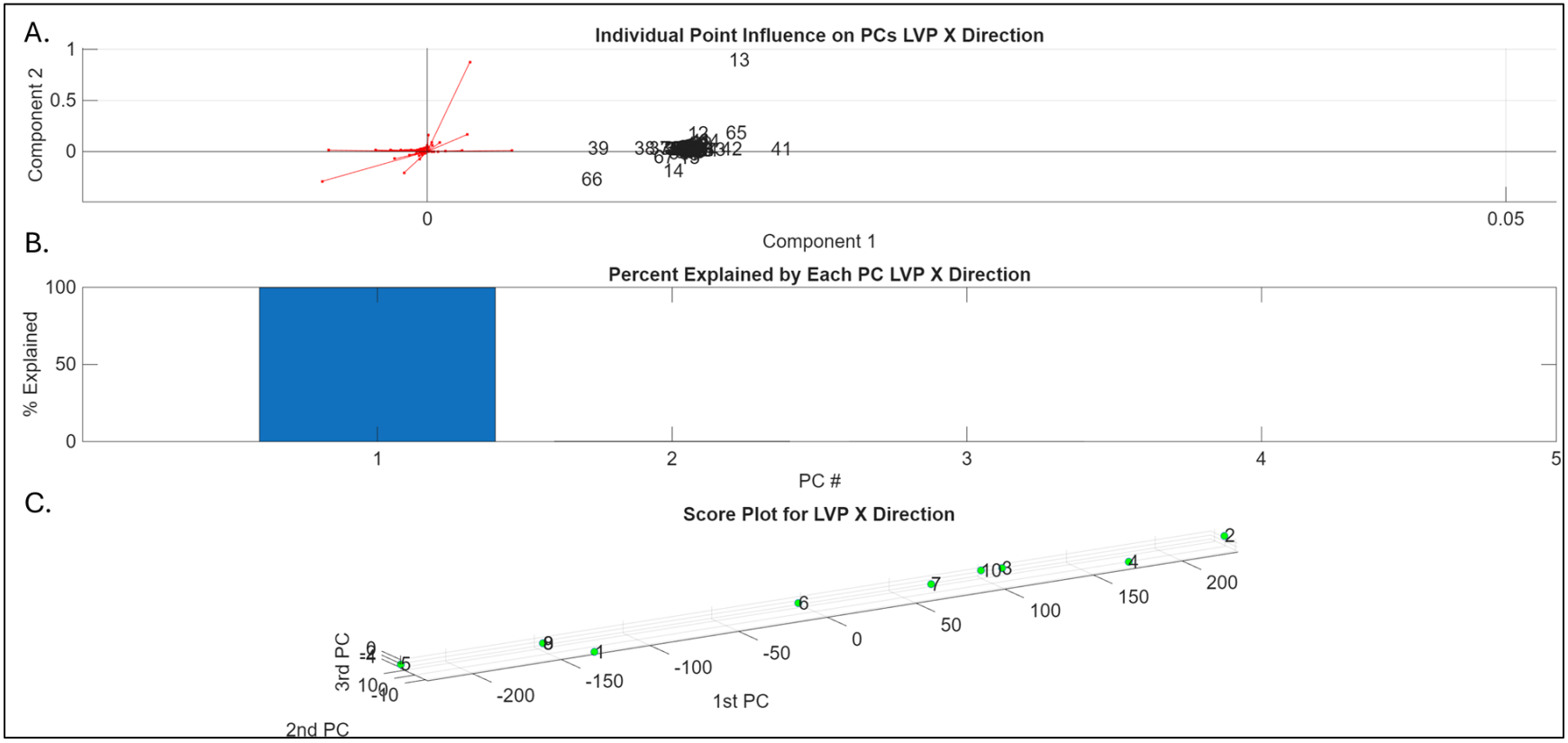

Figure B.20. *PCA results for the X direction of the LVP.* ***A.*** *Individual point influence on the first 2 principal components. Data points in the positive quadrants correspond to positive influence on the indicated principal component.* ***B.*** *Amount of shape variation that can be explained by the first 2-3 principal components quantified by percentage.* ***C****. The score plot shows where the original data points will fall within the transformed PC shape. Points that create more similar shapes, cluster together around 0 after being transformed around the mean while variations may produce outliers.*

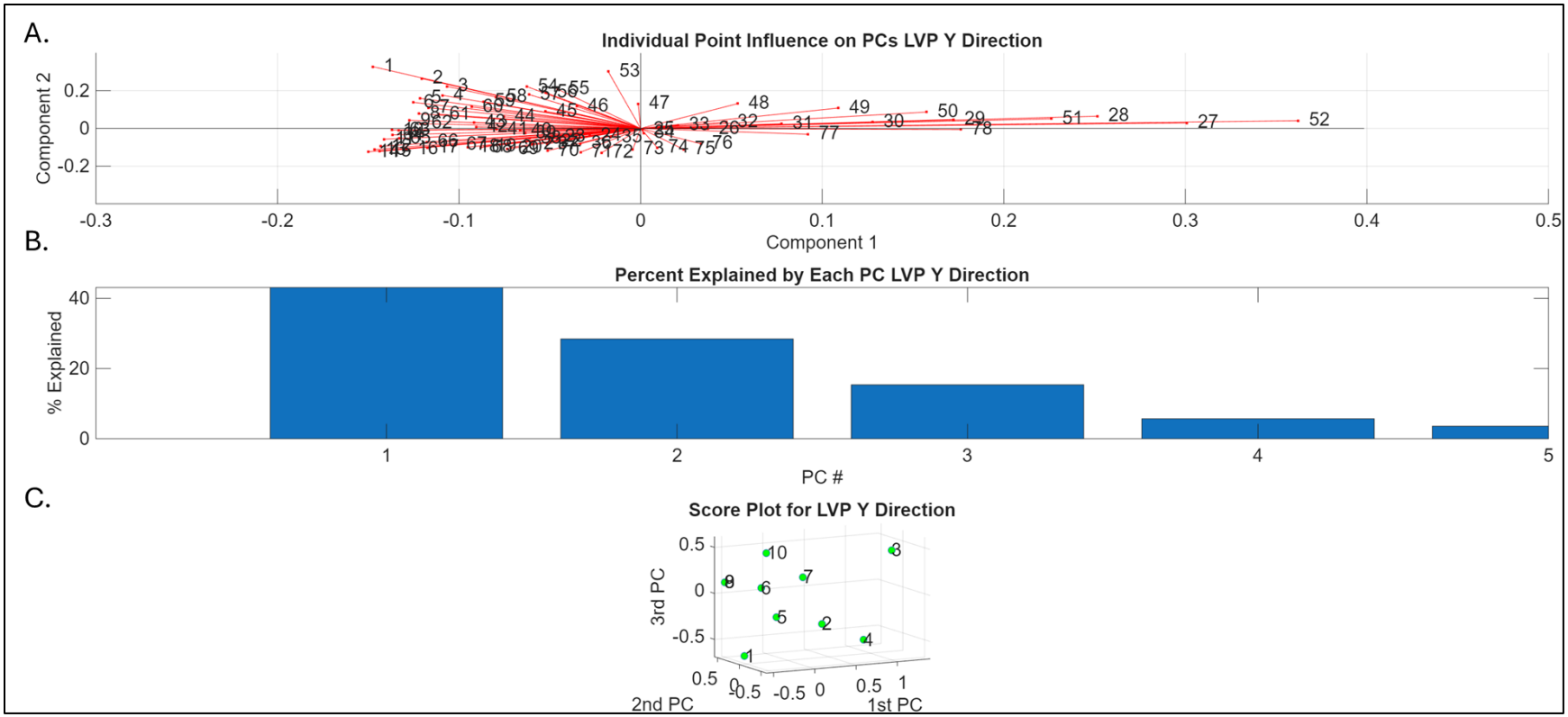

Figure B.21 *PCA results for the Y direction of the LVP.* ***A.*** *Individual point influence on the first 2 principal components. Data points in the positive quadrants correspond to positive influence on the indicated principal component.* ***B.*** *Amount of shape variation that can be explained by the first 2-3 principal components quantified by percentage.* ***C****. The score plot shows where the original data points will fall within the transformed PC shape. Points that create more similar shapes, cluster together around 0 after being transformed around the mean while variations may produce outliers.*

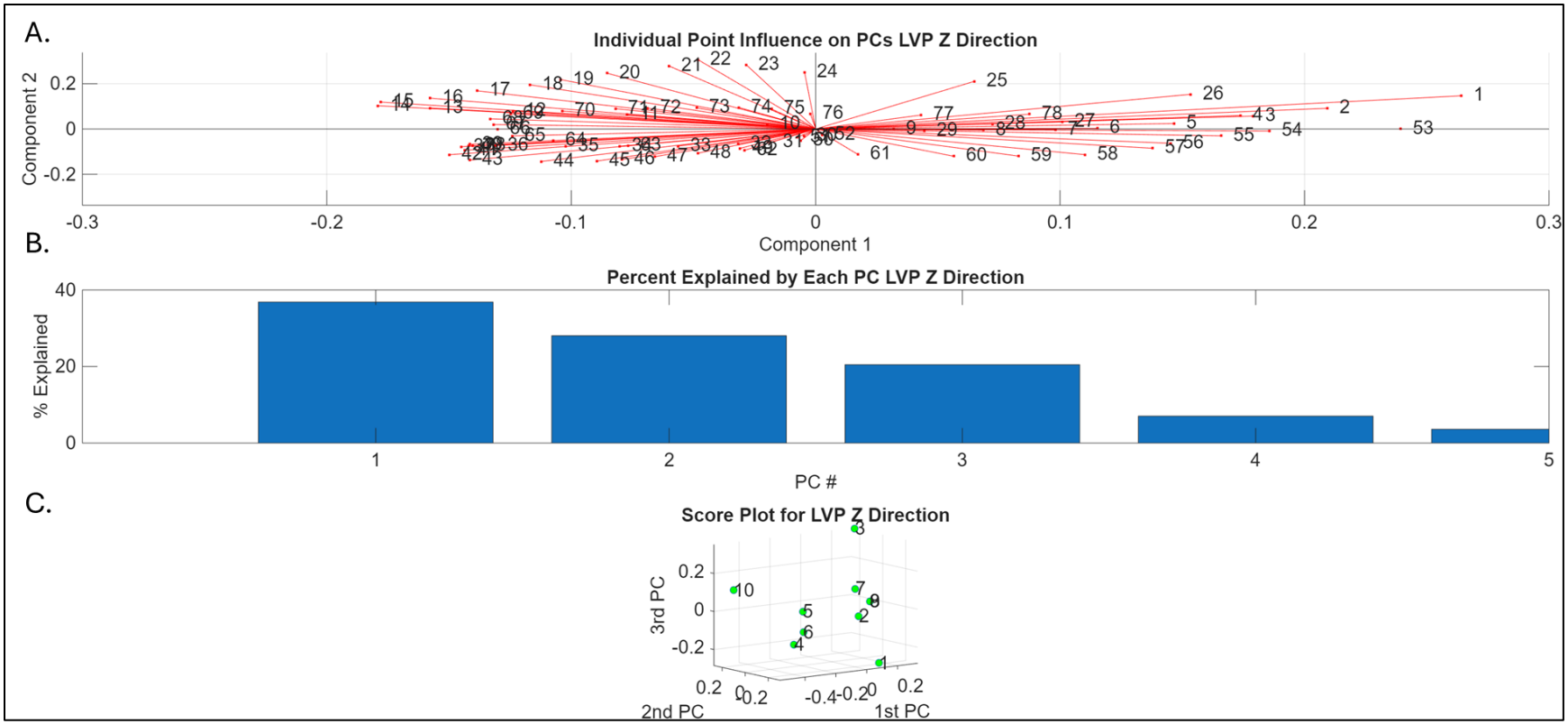

Figure B.22. *PCA results for the Z direction of the LVP.* ***A.*** *Individual point influence on the first 2 principal components. Data points in the positive quadrants correspond to positive influence on the indicated principal component.* ***B.*** *Amount of shape variation that can be explained by the first 2-3 principal components quantified by percentage.* ***C****. The score plot shows where the original data points will fall within the transformed PC shape. Points that create more similar shapes, cluster together around 0 after being transformed around the mean while variations may produce outliers.*

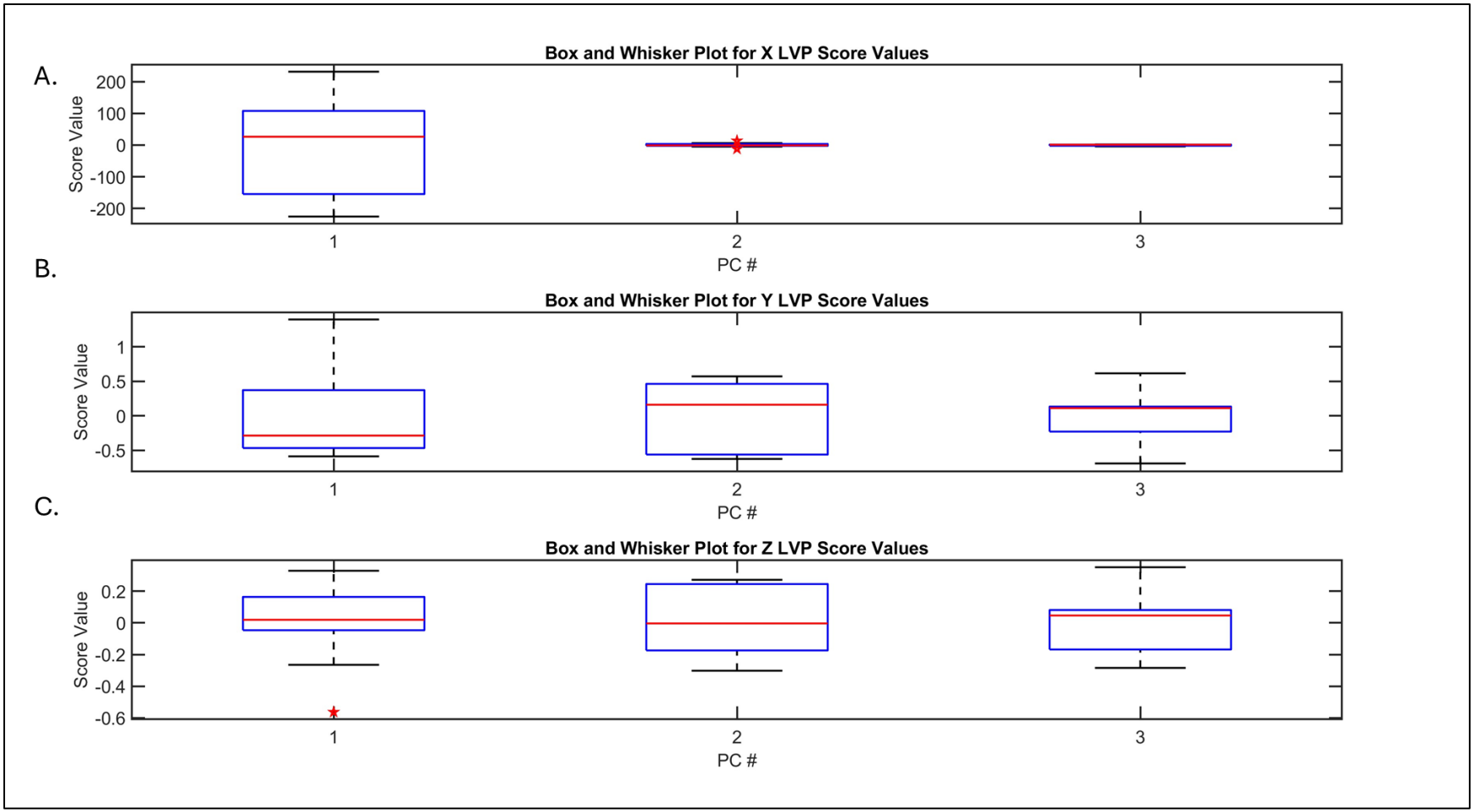

Figure B.23. *Box-and-Whisker plots for LVP data sets to identify potential outliers in patients 1-10. Statistical outliers are outside of upper and lower limits (± 1.5 x IQR) and are shown in red stars if present. Plots are created for score values of the first three PCs.* ***A.*** *Plots from the X plane data sets.* ***B.*** *Plots from the Y plane data sets.* ***C.*** *Plots from the Z plane data sets.*

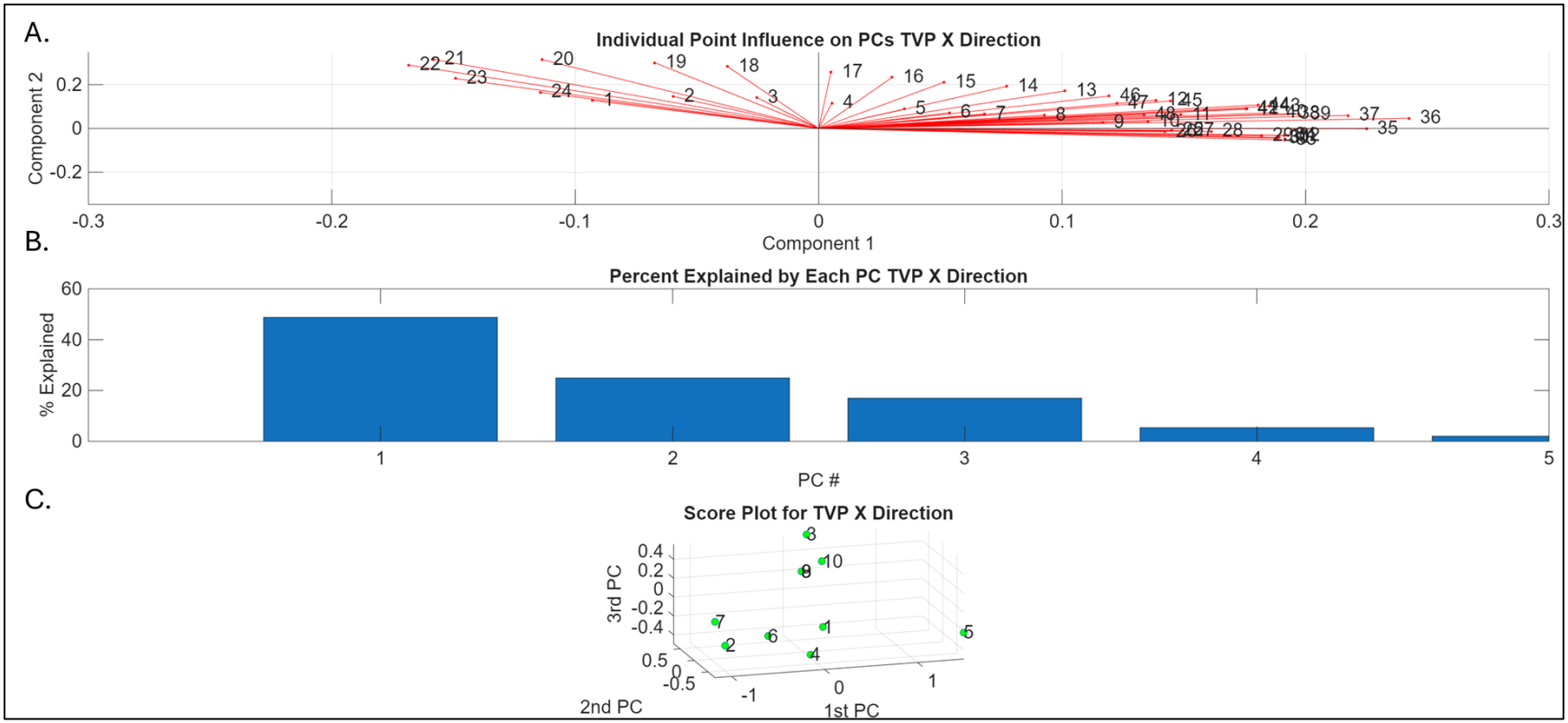

Figure B.24. *PCA results for the X direction of the TVP.* ***A.*** *Individual point influence on the first 2 principal components. Data points in the positive quadrants correspond to positive influence on the indicated principal component.* ***B.*** *Amount of shape variation that can be explained by the first 2-3 principal components quantified by percentage.* ***C****. The score plot shows where the original data points will fall within the transformed PC shape. Points that create more similar shapes, cluster together around 0 after being transformed around the mean while variations may produce outliers*

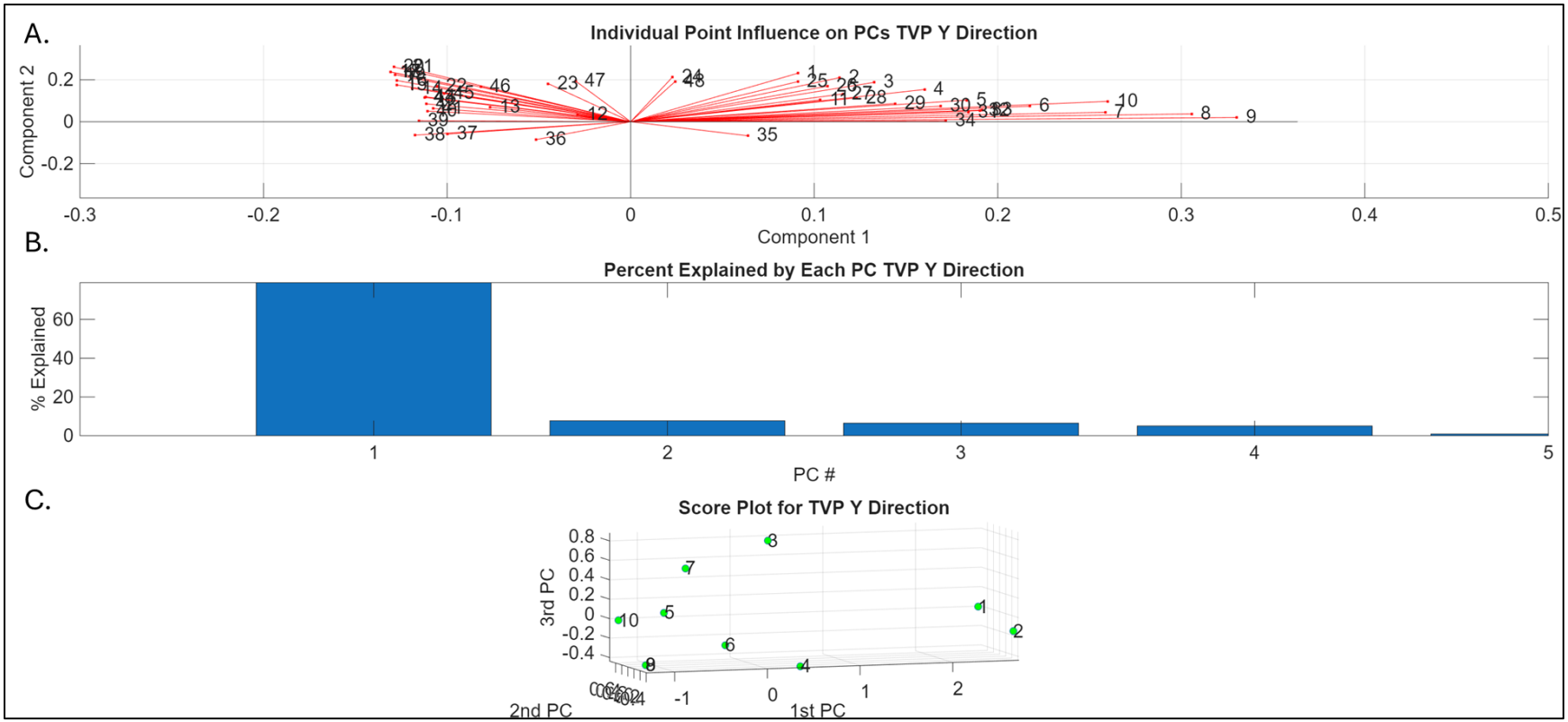

Figure B.25. *PCA results for the Y direction of the TVP.* ***A.*** *Individual point influence on the first 2 principal components. Data points in the positive quadrants correspond to positive influence on the indicated principal component.* ***B.*** *Amount of shape variation that can be explained by the first 2-3 principal components quantified by percentage.* ***C****. The score plot shows where the original data points will fall within the transformed PC shape. Points that create more similar shapes, cluster together around 0 after being transformed around the mean while variations may produce outliers.*

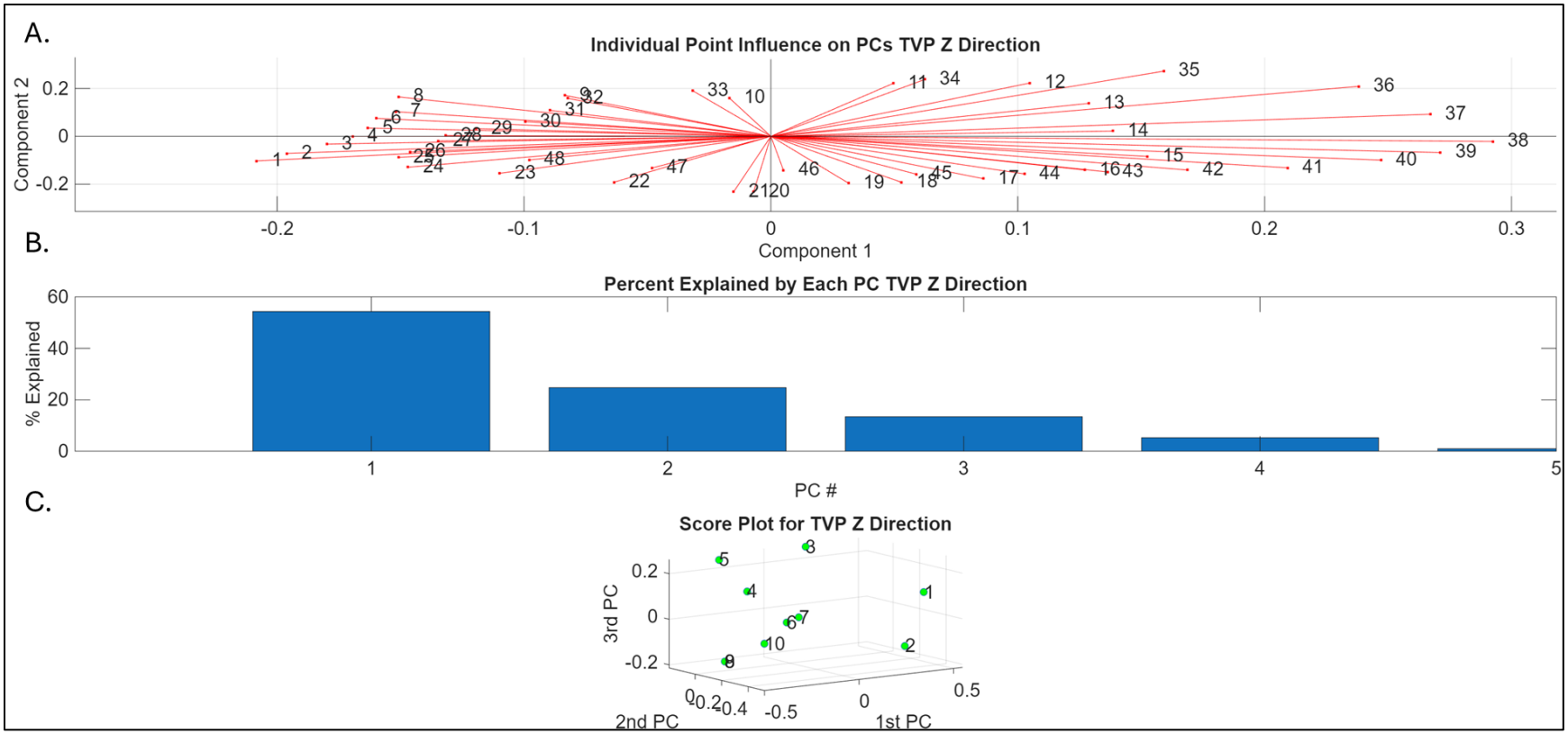

Figure B.26. *PCA results for the Z direction of the TVP.* ***A.*** *Individual point influence on the first 2 principal components. Data points in the positive quadrants correspond to positive influence on the indicated principal component.* ***B.*** *Amount of shape variation that can be explained by the first 2-3 principal components quantified by percentage.* ***C****. The score plot shows where the original data points will fall within the transformed PC shape. Points that create more similar shapes, cluster together around 0 after being transformed around the mean while variations may produce outliers.*

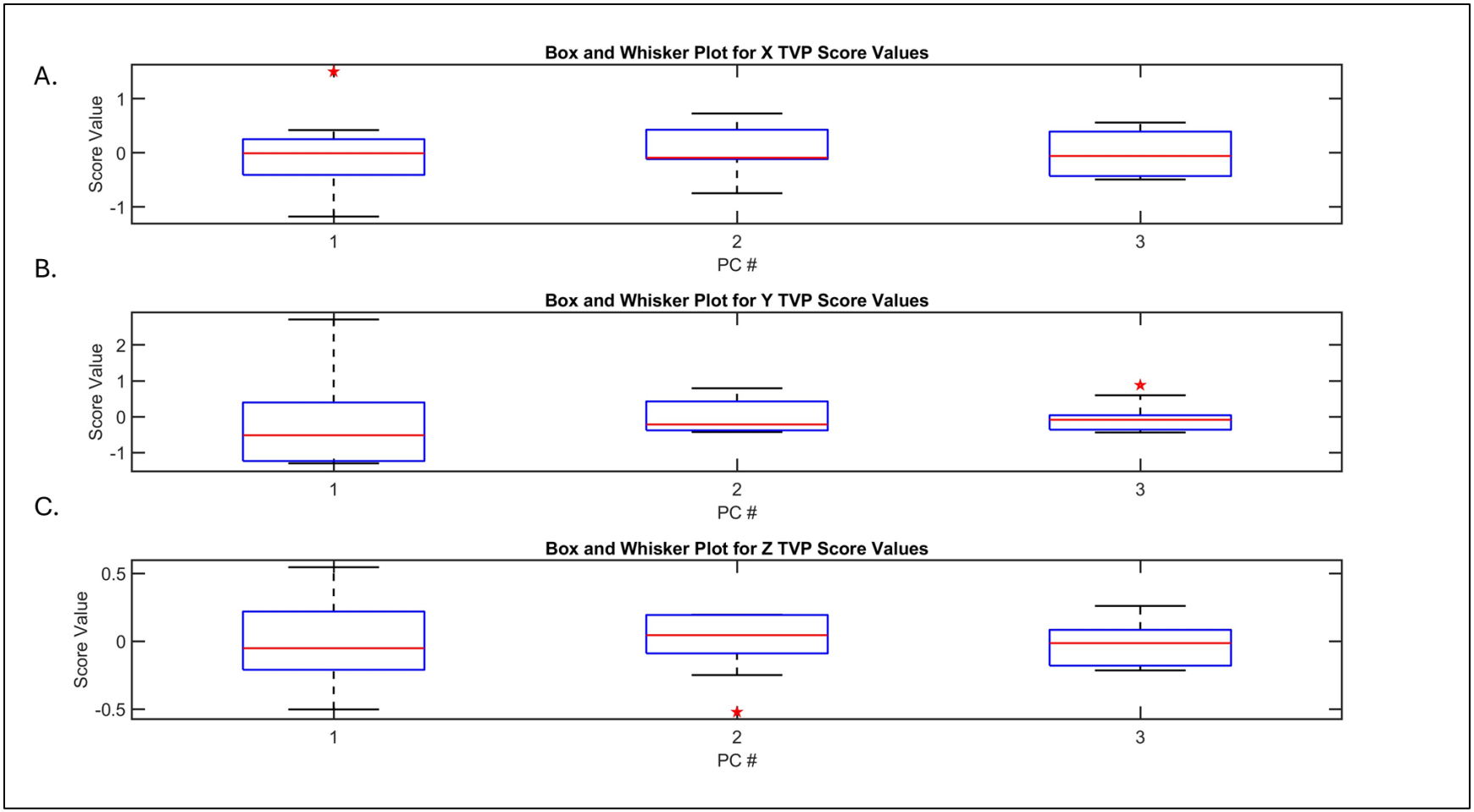

Figure B.27. *Box-and-Whisker plots for TVP data sets to identify potential outliers in patients 1-10. Statistical outliers are outside of upper and lower limits (± 1.5 x IQR) and are shown in red stars if present. Plots are created for score values of the first three PCs.* ***A.*** *Plots from the X plane data sets.* ***B.*** *Plots from the Y plane data sets.* ***C.*** *Plots from the Z plane data sets.*

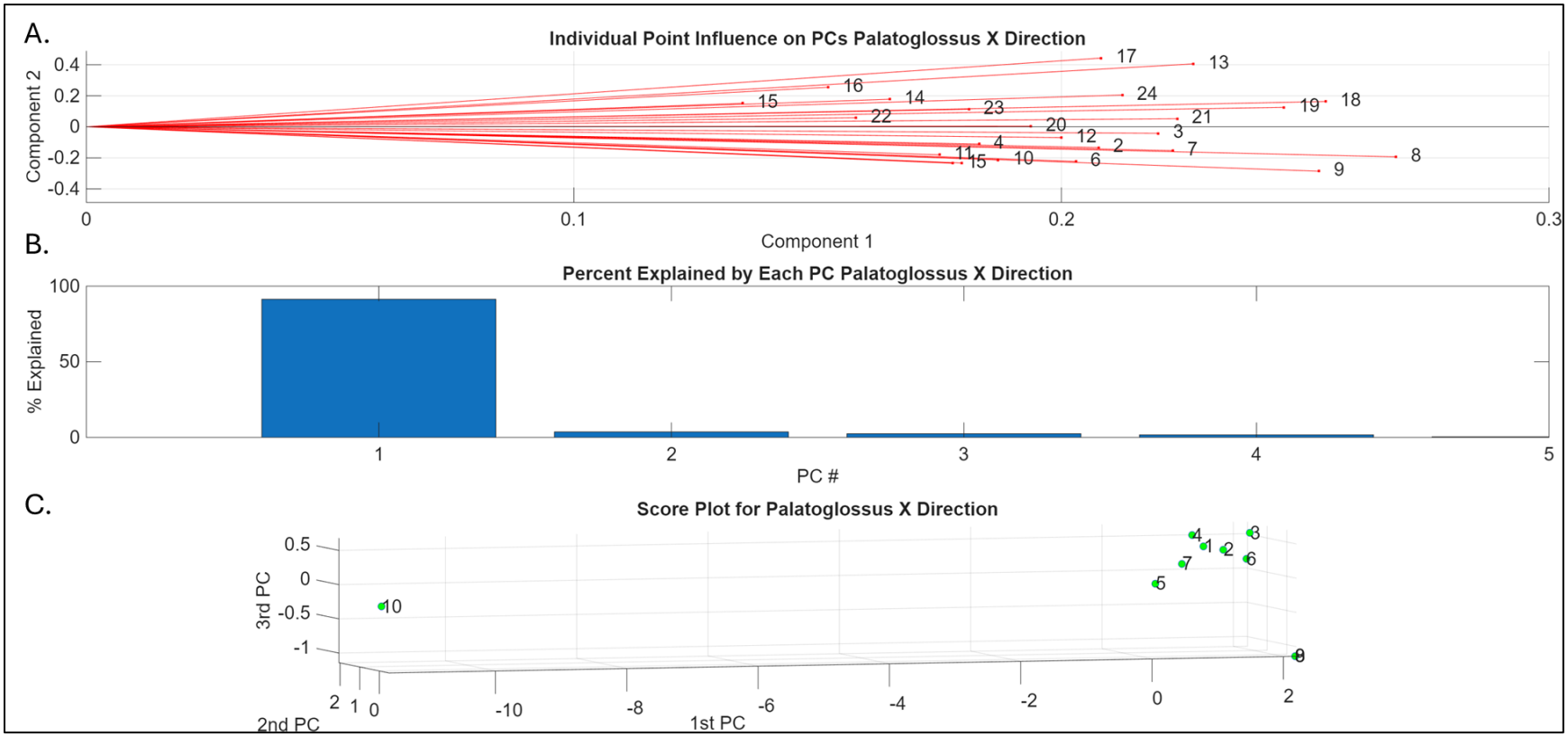

Figure B.28. *PCA results for the X direction of the palatoglossus.* ***A.*** *Individual point influence on the first 2 principal components. Data points in the positive quadrants correspond to positive influence on the indicated principal component.* ***B.*** *Amount of shape variation that can be explained by the first 2-3 principal components quantified by percentage.* ***C***. *The score plot shows where the original data points will fall within the transformed PC shape. Points that create more similar shapes, cluster together around 0 after being transformed around the mean while variations may produce outliers.*

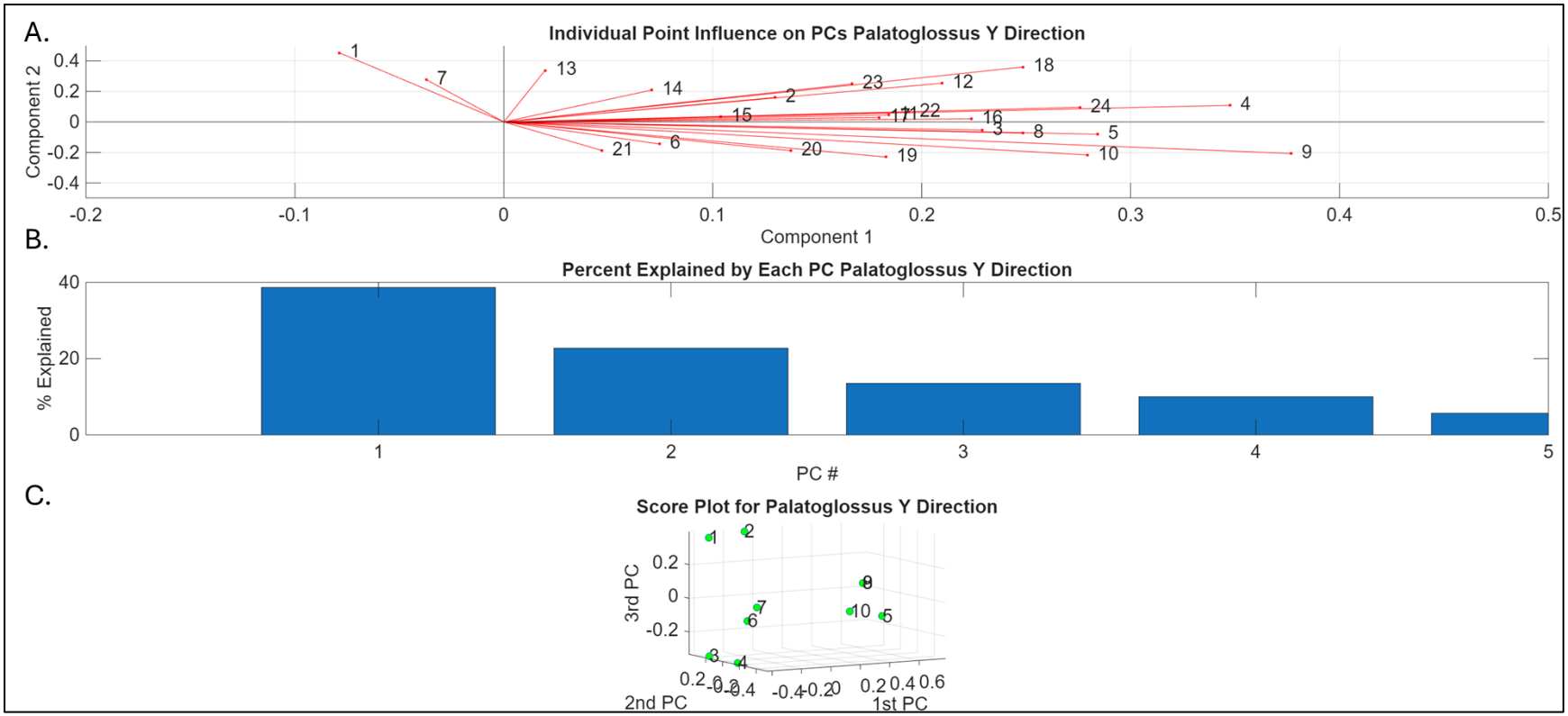

Figure B.29. *PCA results for the Y direction of the palatoglossus.* ***A.*** *Individual point influence on the first 2 principal components. Data points in the positive quadrants correspond to positive influence on the indicated principal component.* ***B.*** *Amount of shape variation that can be explained by the first 2-3 principal components quantified by percentage.* ***C****. The score plot shows where the original data points will fall within the transformed PC shape. Points that create more similar shapes, cluster together around 0 after being transformed around the mean while variations may produce outliers.*

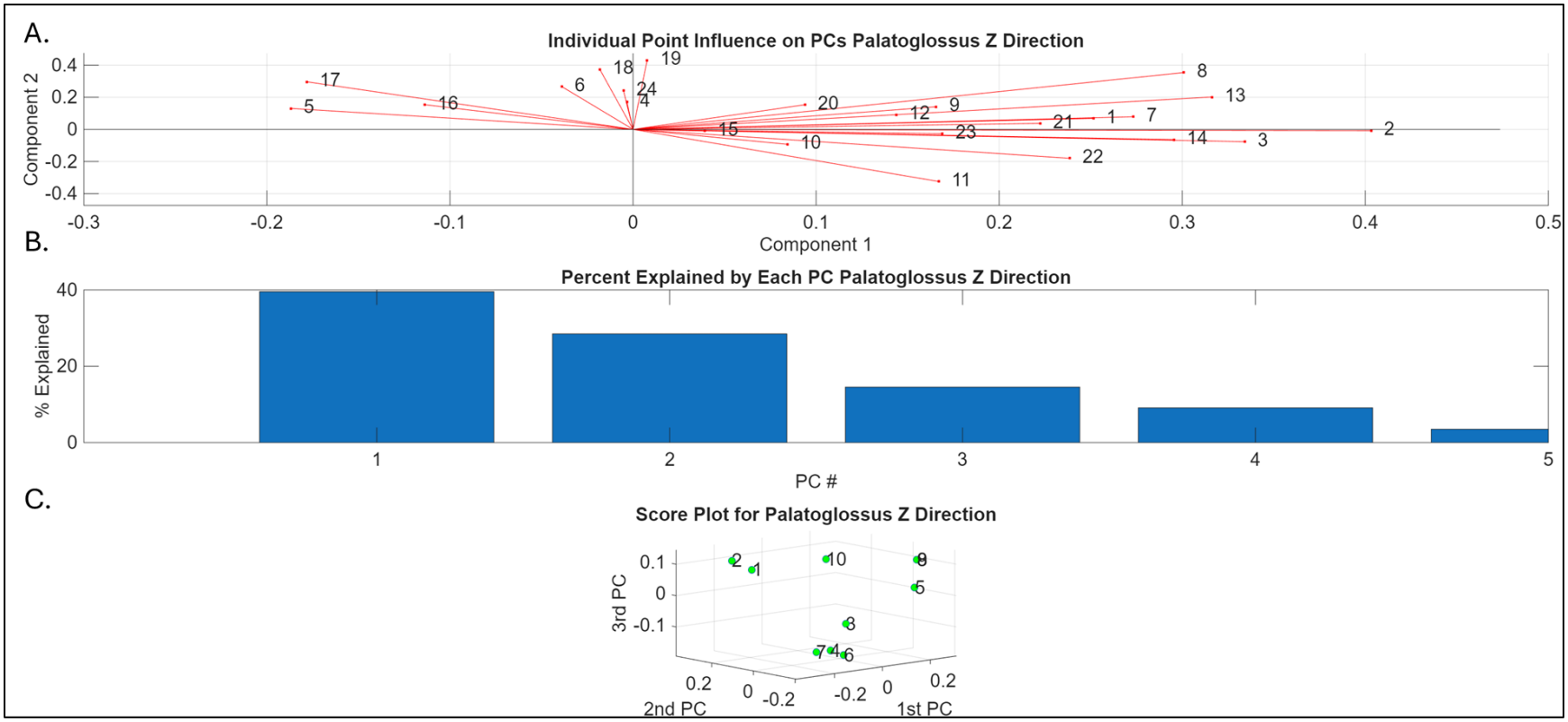

Figure B.30. *PCA results for the Z direction of the palatoglossus.* ***A.*** *Individual point influence on the first 2 principal components. Data points in the positive quadrants correspond to positive influence on the indicated principal component.* ***B.*** *Amount of shape variation that can be explained by the first 2-3 principal components quantified by percentage.* ***C****. The score plot shows where the original data points will fall within the transformed PC shape. Points that create more similar shapes, cluster together around 0 after being transformed around the mean while variations may produce outliers.*

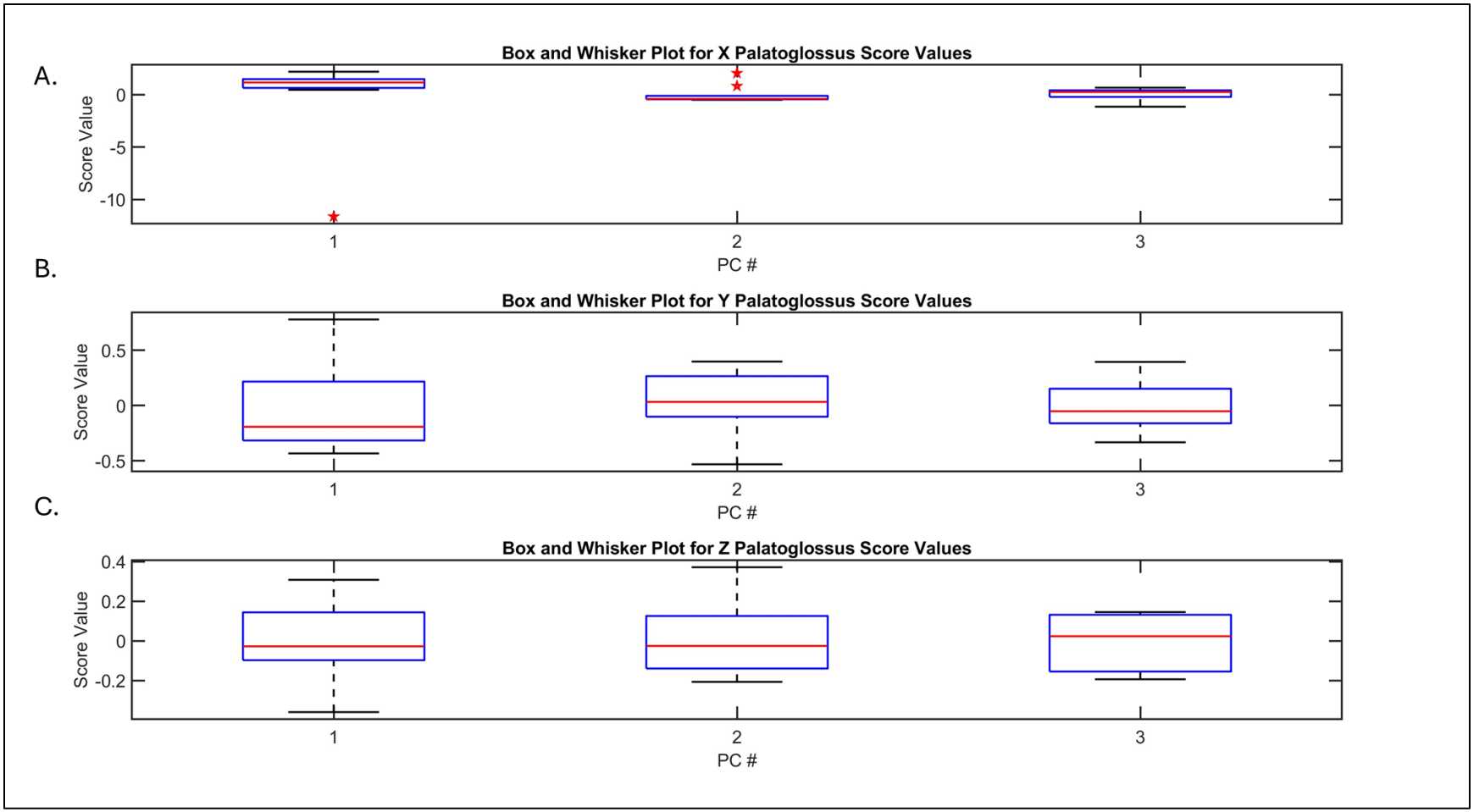

Figure B.31. *Box-and-Whisker plots for palatoglossus data sets to identify potential outliers in patients 1-10. Statistical outliers are outside of upper and lower limits (± 1.5 x IQR) and are shown in red stars if present. Plots are created for score values of the first three PCs.* ***A.*** *Plots from the X plane data sets.* ***B.*** *Plots from the Y plane data sets.* ***C.*** *Plots from the Z plane data sets*

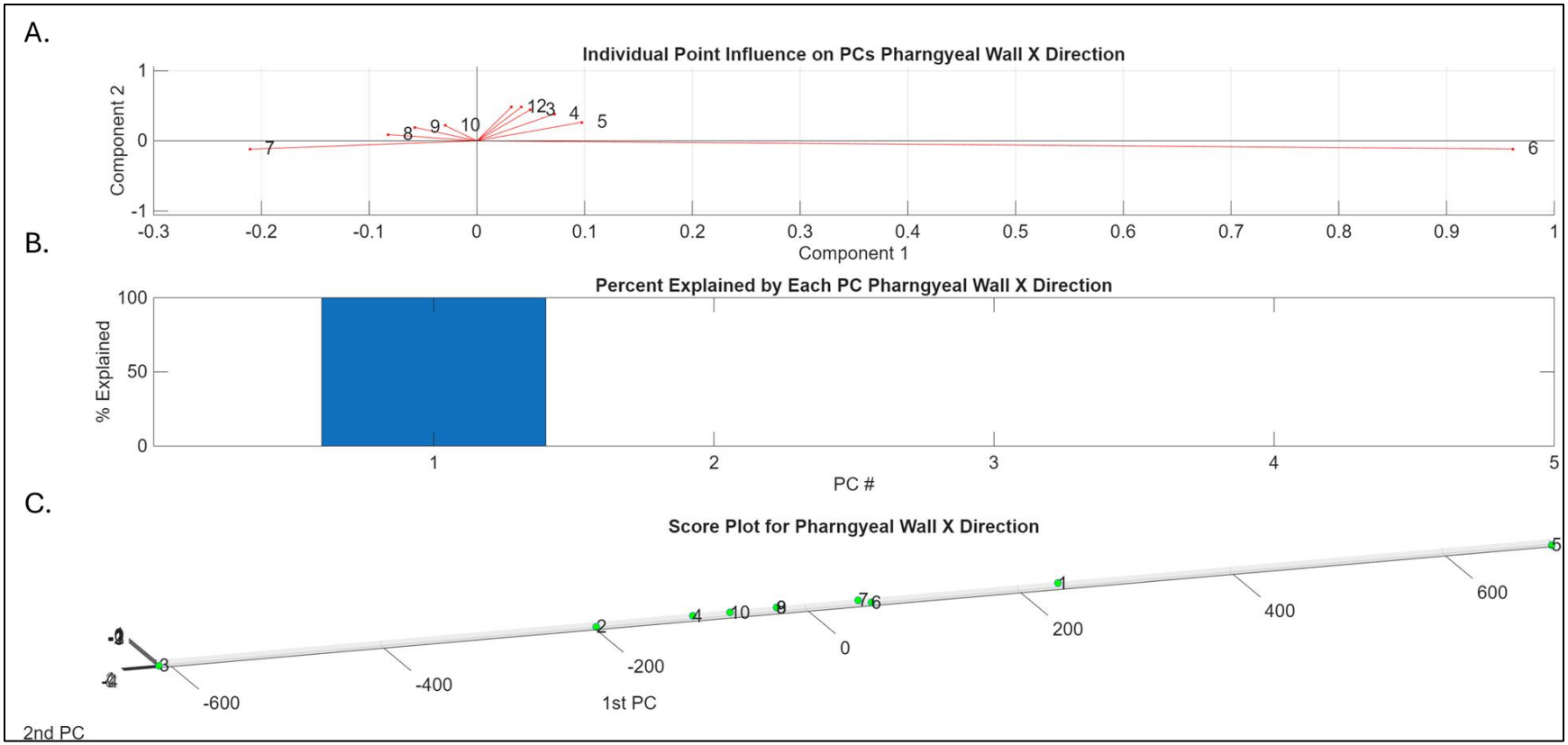

Figure B.32. *PCA results for the X direction of the pharyngeal wall.* ***A.*** *Individual point influence on the first 2 principal components. Data points in the positive quadrants correspond to positive influence on the indicated principal component.* ***B.*** *Amount of shape variation that can be explained by the first 2-3 principal components quantified by percentage.* ***C****. The score plot shows where the original data points will fall within the transformed PC shape. Points that create more similar shapes, cluster together around 0 after being transformed around the mean while variations may produce outliers.*

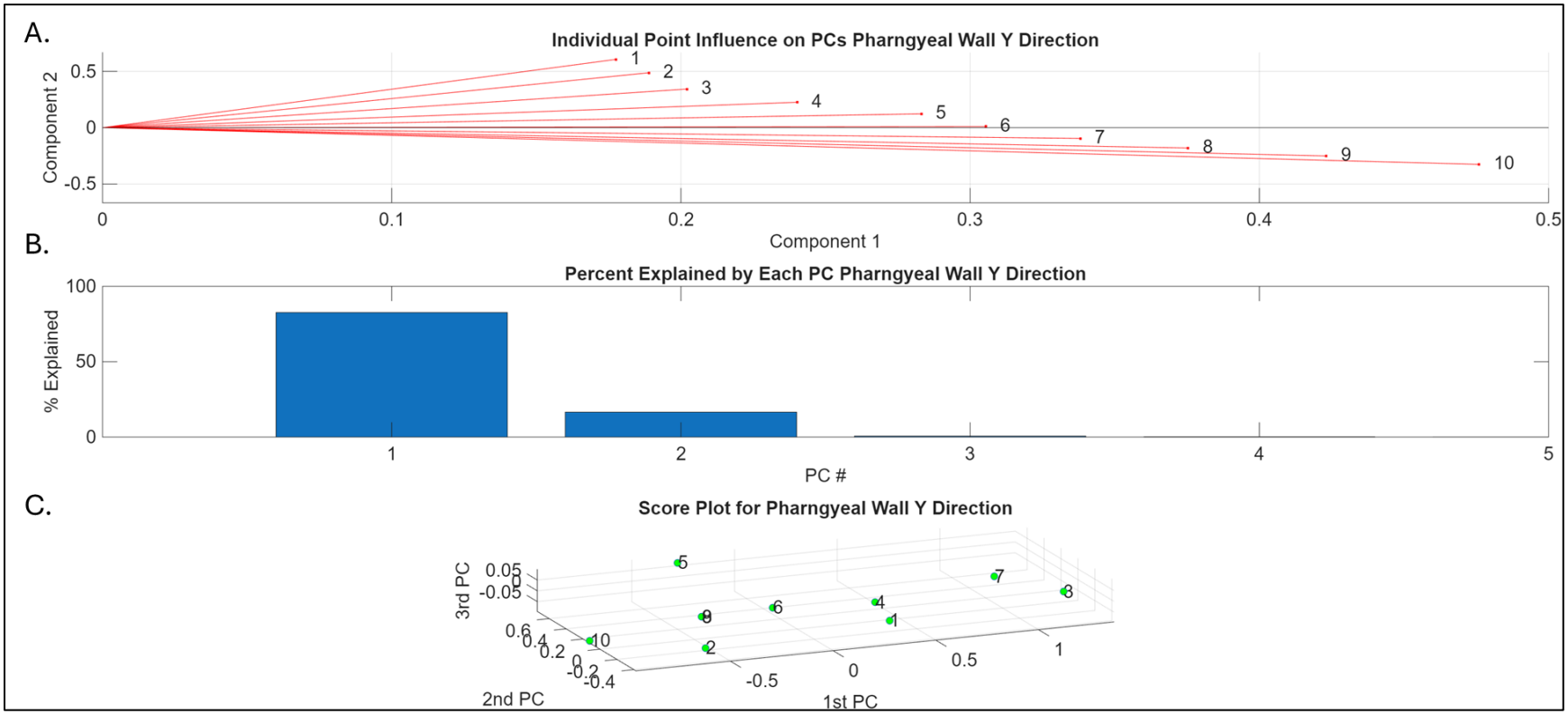

Figure B.33. *PCA results for the Y direction of the pharyngeal wall.* ***A.*** *Individual point influence on the first 2 principal components. Data points in the positive quadrants correspond to positive influence on the indicated principal component.* ***B.*** *Amount of shape variation that can be explained by the first 2-3 principal components quantified by percentage.* ***C****. The score plot shows where the original data points will fall within the transformed PC shape. Points that create more similar shapes, cluster together around 0 after being transformed around the mean while variations may produce outliers.*

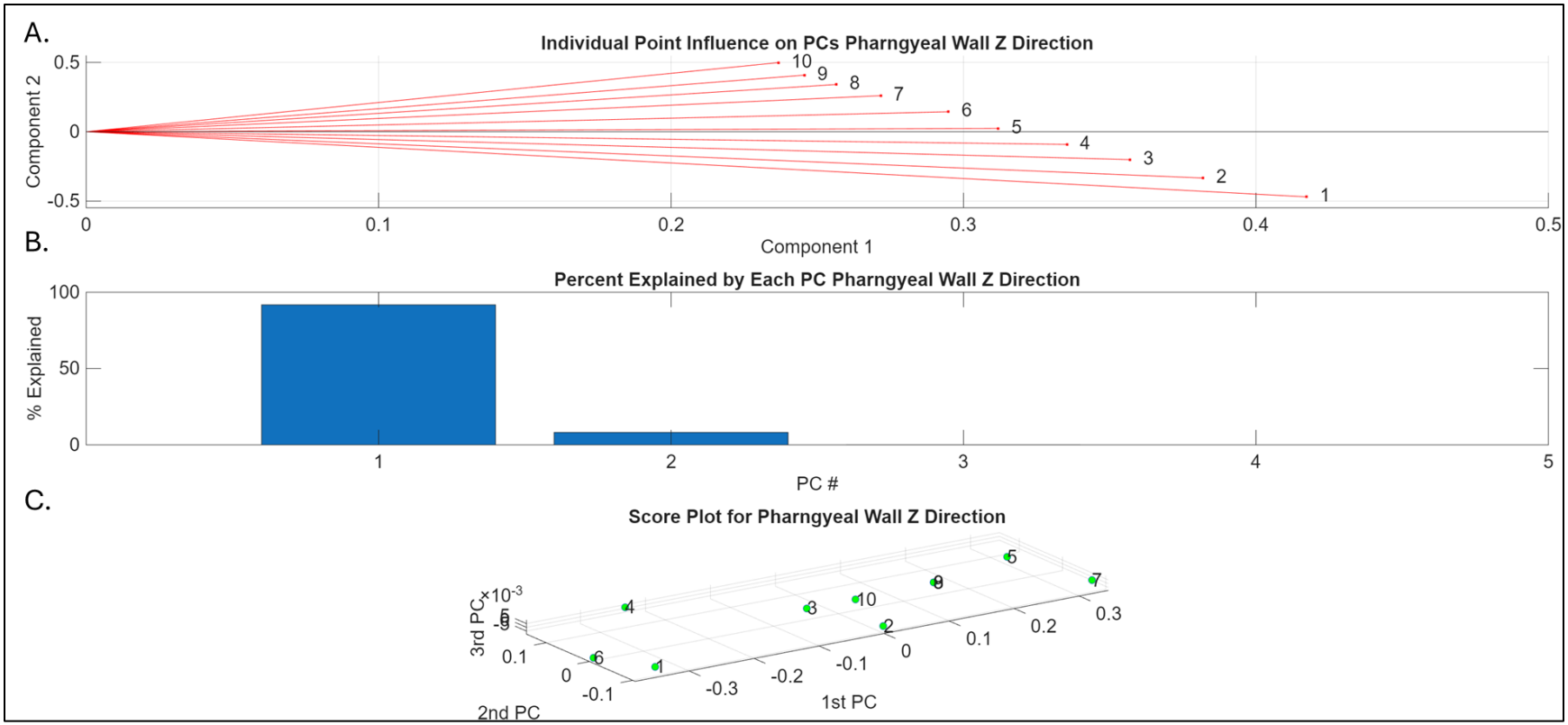

Figure B.34. *PCA results for the Z direction of the pharyngeal wall.* ***A.*** *Individual point influence on the first 2 principal components. Data points in the positive quadrants correspond to positive influence on the indicated principal component.* ***B.*** *Amount of shape variation that can be explained by the first 2-3 principal components quantified by percentage.* ***C****. The score plot shows where the original data points will fall within the transformed PC shape. Points that create more similar shapes, cluster together around 0 after being transformed around the mean while variations may produce outliers.*

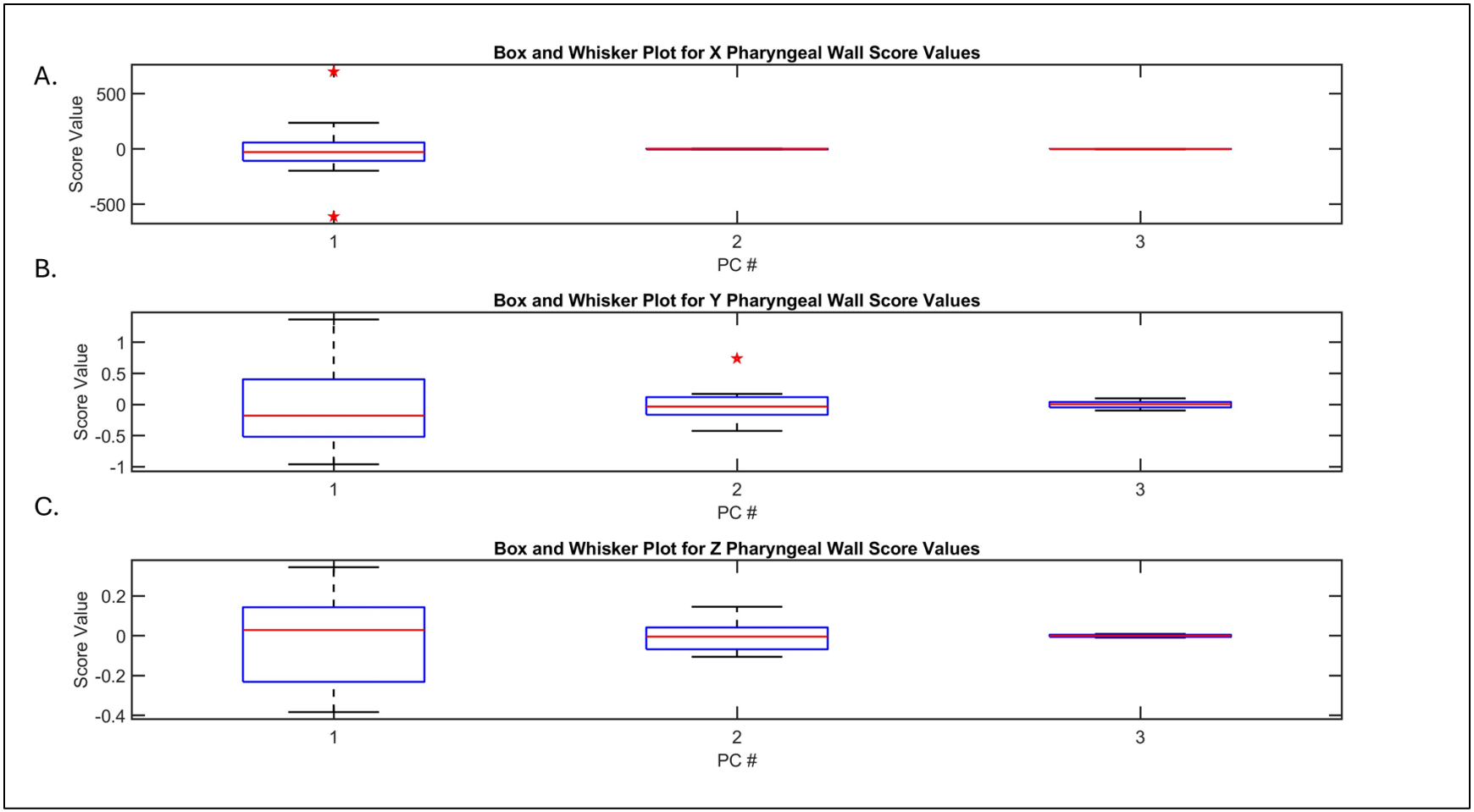

Figure B.35. *Box-and-Whisker plots for pharyngeal wall data sets to identify potential outliers in patients 1-10. Statistical outliers are outside of upper and lower limits (± 1.5 x IQR) and are shown in red stars if present. Plots are created for score values of the first three PCs.* ***A.*** *Plots from the X plane data sets.* ***B.*** *Plots from the Y plane data sets.* ***C.*** *Plots from the Z plane data sets.*

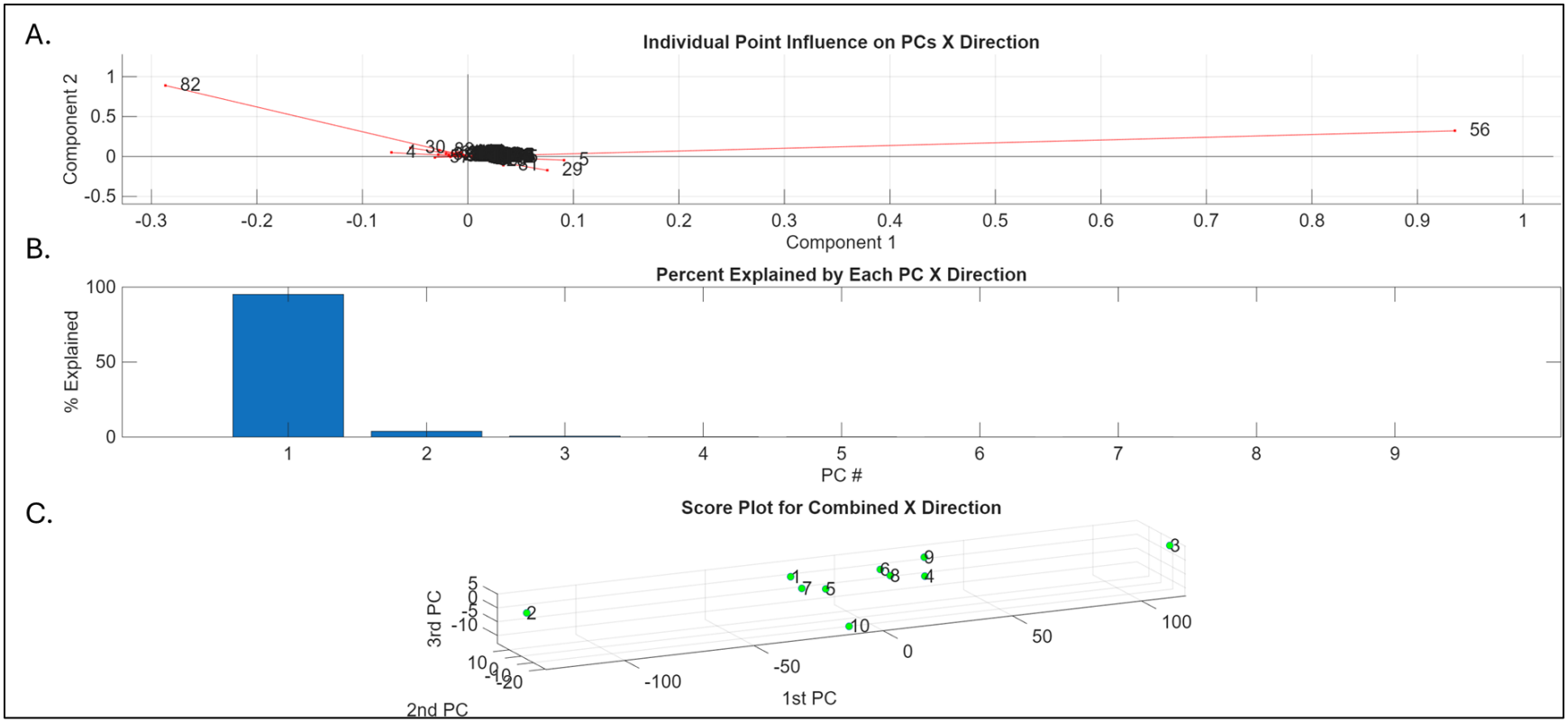

Figure B.36. *PCA results for the X direction of all combined parts.* ***A.*** *Individual point influence on the first 2 principal components. Data points in the positive quadrants correspond to positive influence on the indicated principal component.* ***B.*** *Amount of shape variation that can be explained by the first 2-3 principal components quantified by percentage.* ***C****. The score plot shows where the original data points will fall within the transformed PC shape. Points that create more similar shapes, cluster together around 0 after being transformed around the mean while variations may produce outliers*

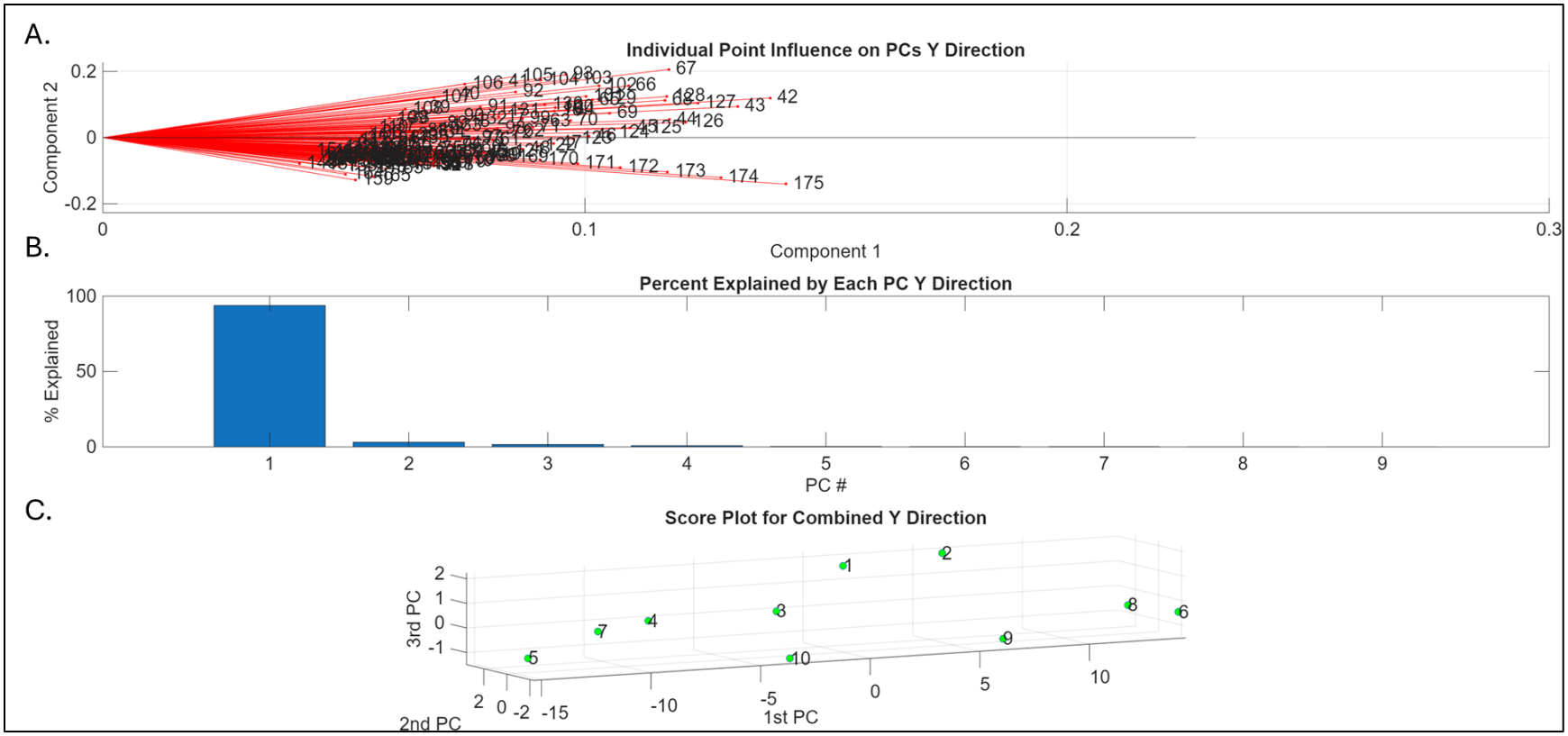

Figure B.37. *PCA results for the Y direction of all combined parts.* ***A.*** *Individual point influence on the first 2 principal components. Data points in the positive quadrants correspond to positive influence on the indicated principal component.* ***B.*** *Amount of shape variation that can be explained by the first 2-3 principal components quantified by percentage.* ***C****. The score plot shows where the original data points will fall within the transformed PC shape. Points that create more similar shapes, cluster together around 0 after being transformed around the mean while variations may produce outliers.*

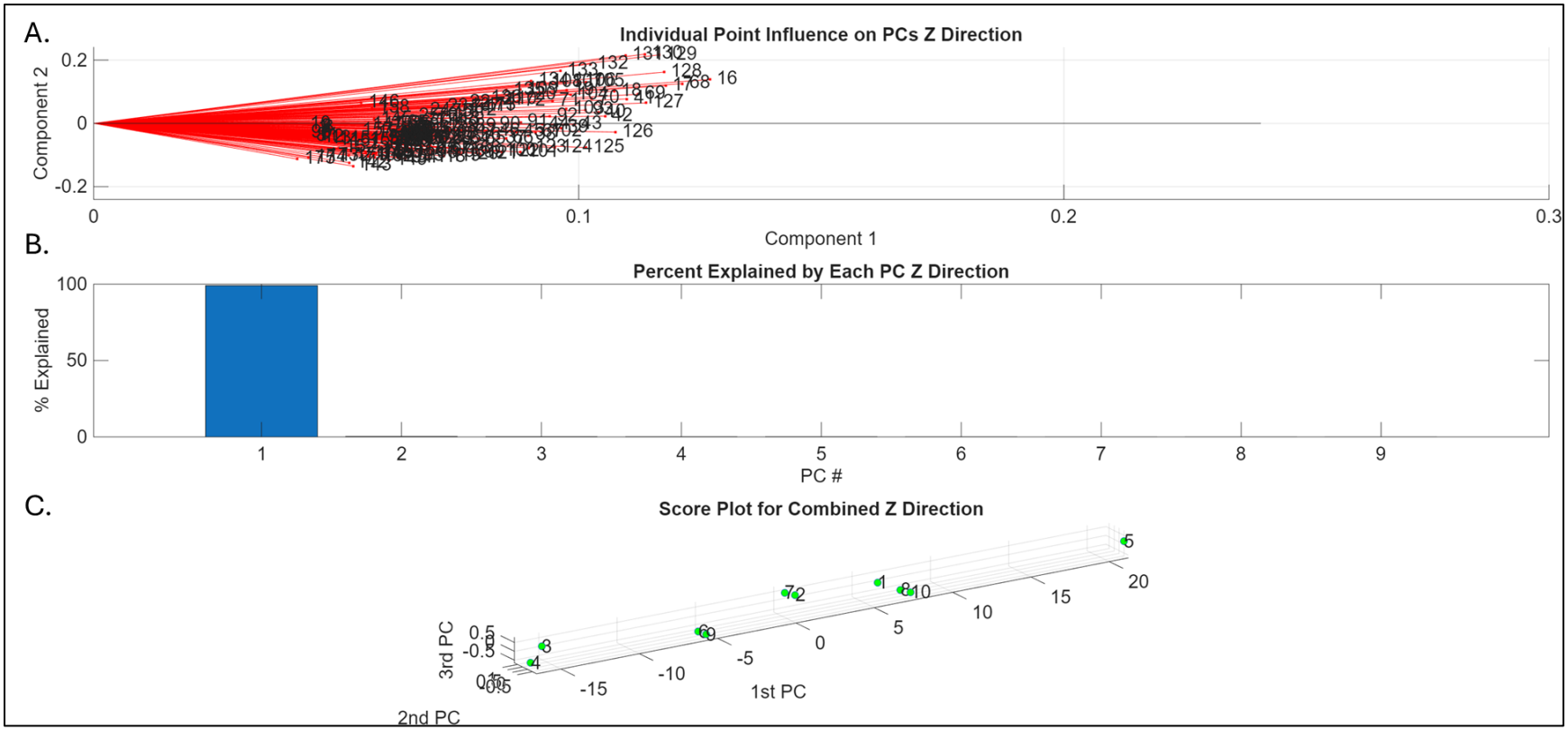

Figure B.38. *PCA results for the Z direction of all combined parts.* ***A.*** *Individual point influence on the first 2 principal components. Data points in the positive quadrants correspond to positive influence on the indicated principal component.* ***B.*** *Amount of shape variation that can be explained by the first 2-3 principal components quantified by percentage.* ***C****. The score plot shows where the original data points will fall within the transformed PC shape. Points that create more similar shapes, cluster together around 0 after being transformed around the mean while variations may produce outliers.*

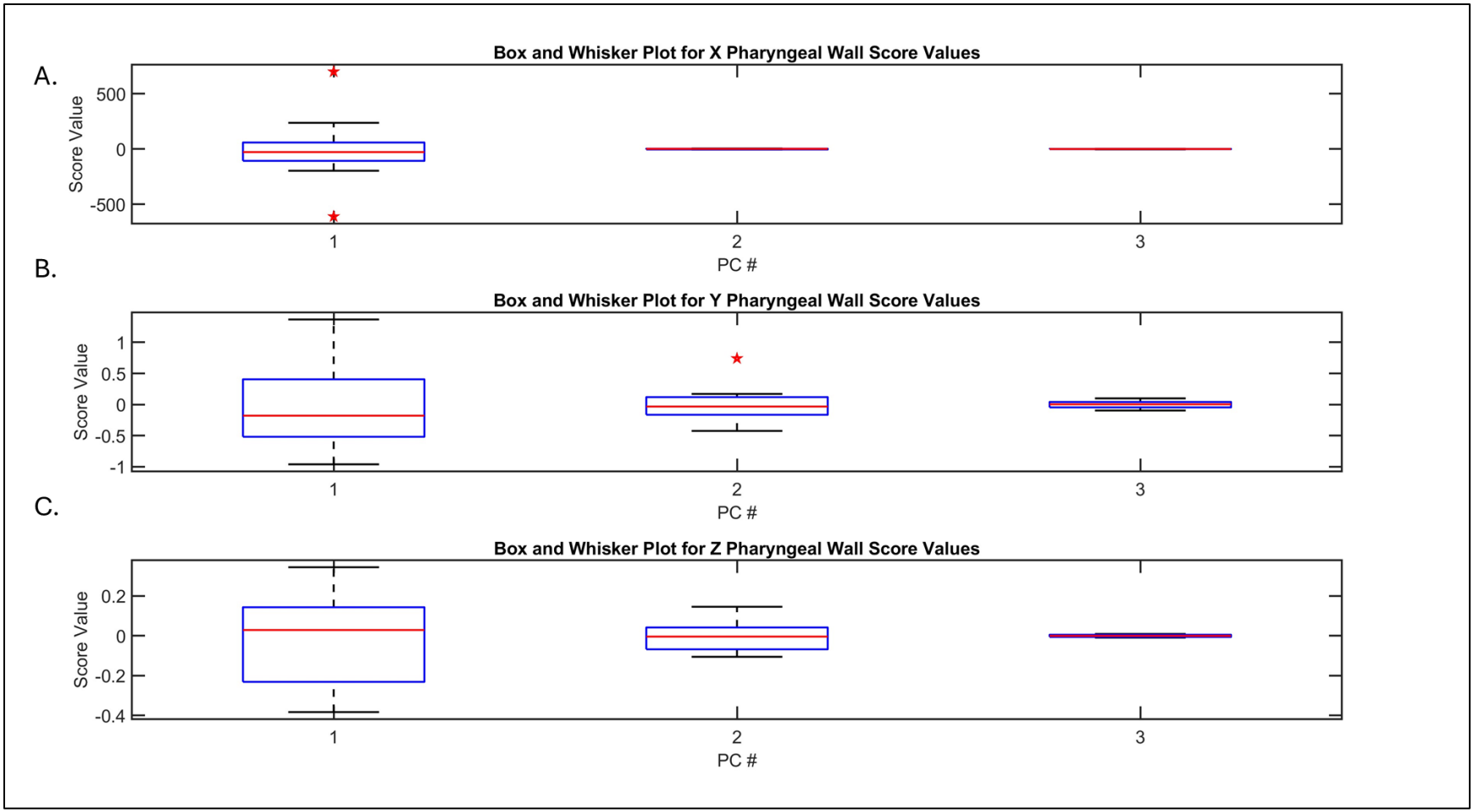

Figure B.39. *Box-and-Whisker plots for combined data sets to identify potential outliers in patients 1-10. Statistical outliers are outside of upper and lower limits (± 1.5 x IQR) and are shown in red stars if present. Plots are created for score values of the first three PCs.* ***A.*** *Plots from the X plane data sets.* ***B.*** *Plots from the Y plane data sets.* ***C.*** *Plots from the Z plane data sets.*

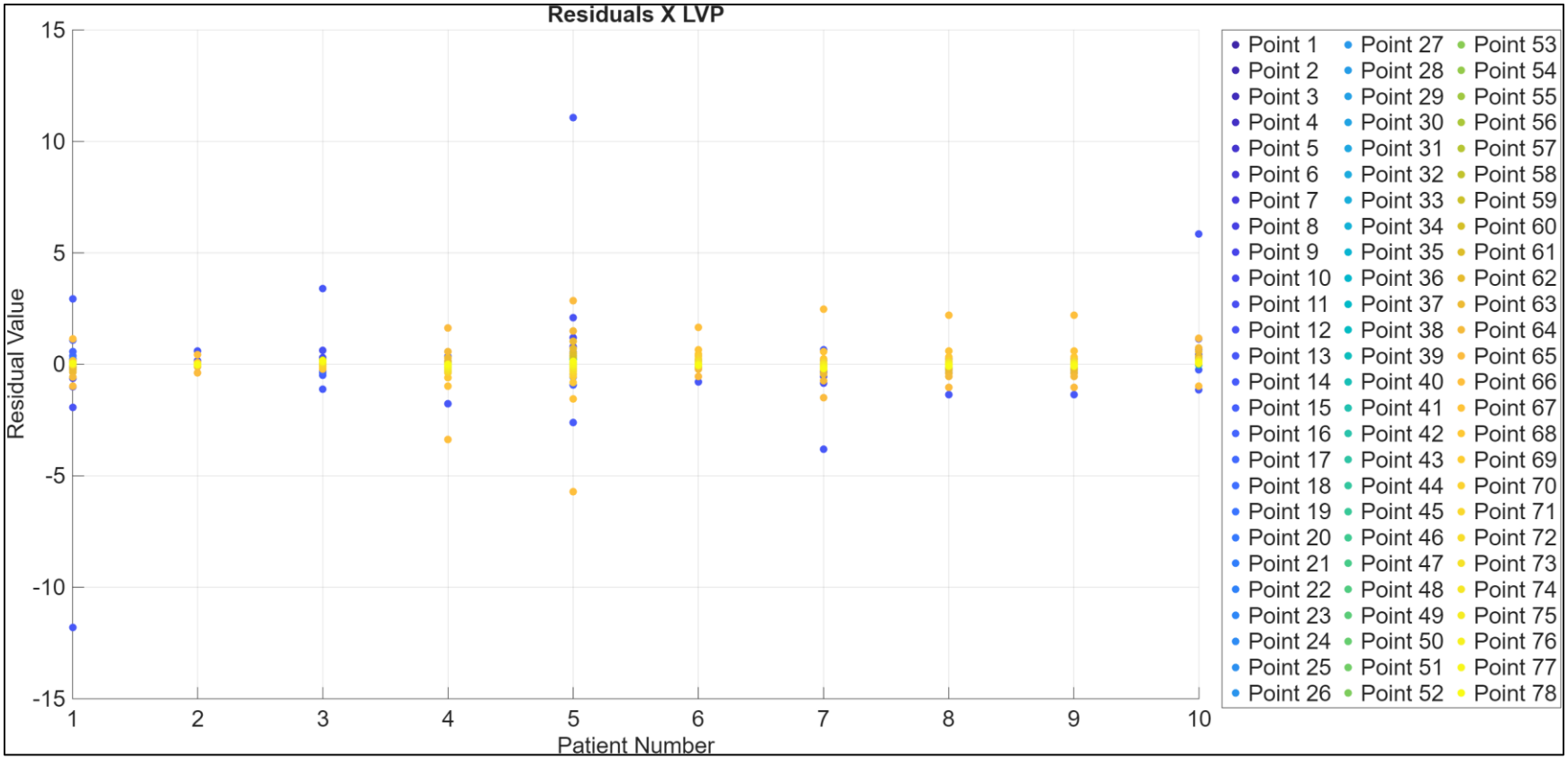

Figure B.40. *PCA residuals for the X direction of the LVP. Points close to 0 indicate a strong fit with points farther away from 0 indicating a weaker fit.*

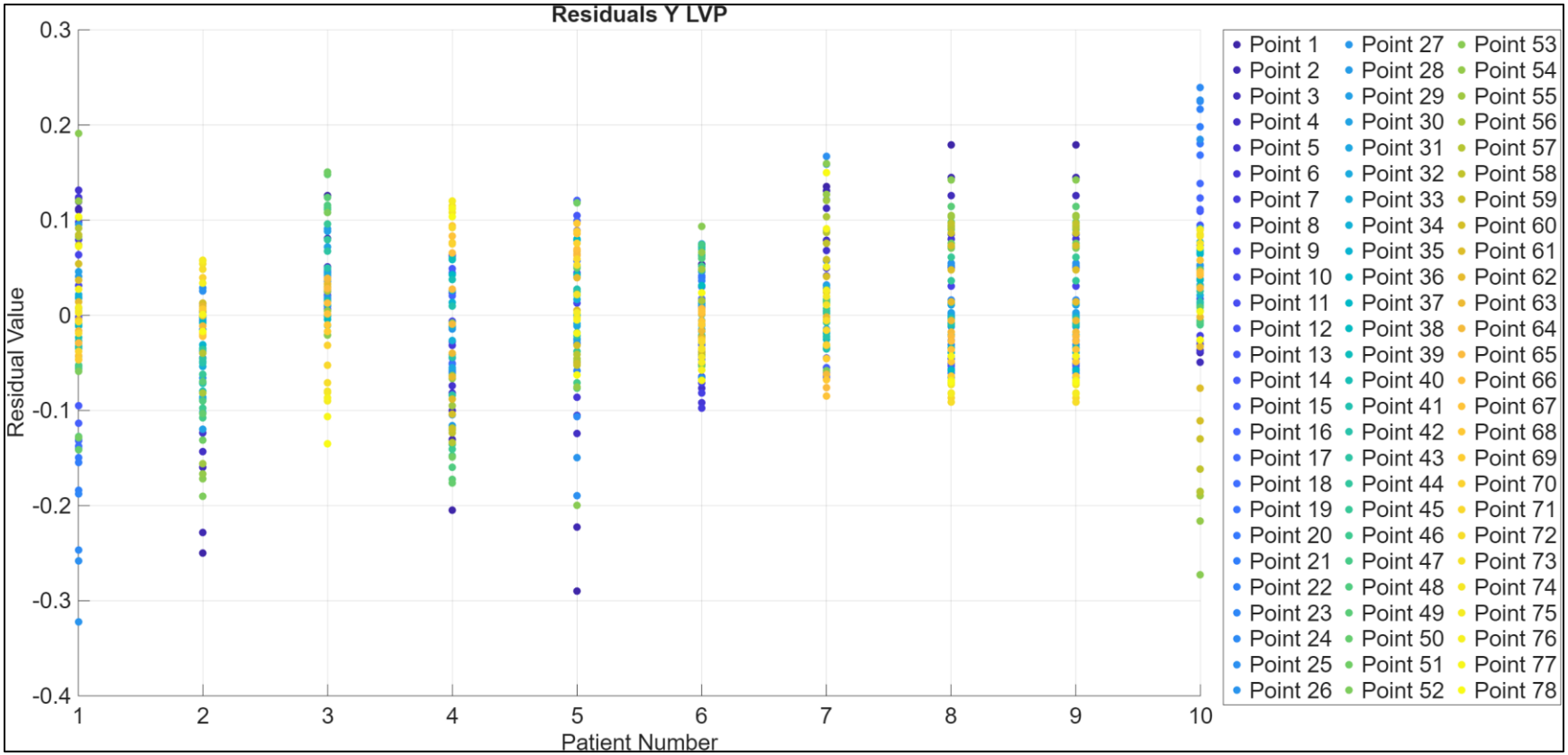

Figure B.41. *PCA residuals for the Y direction of the LVP. Points close to 0 indicate a strong fit with points farther away from 0 indicating a weaker fit*

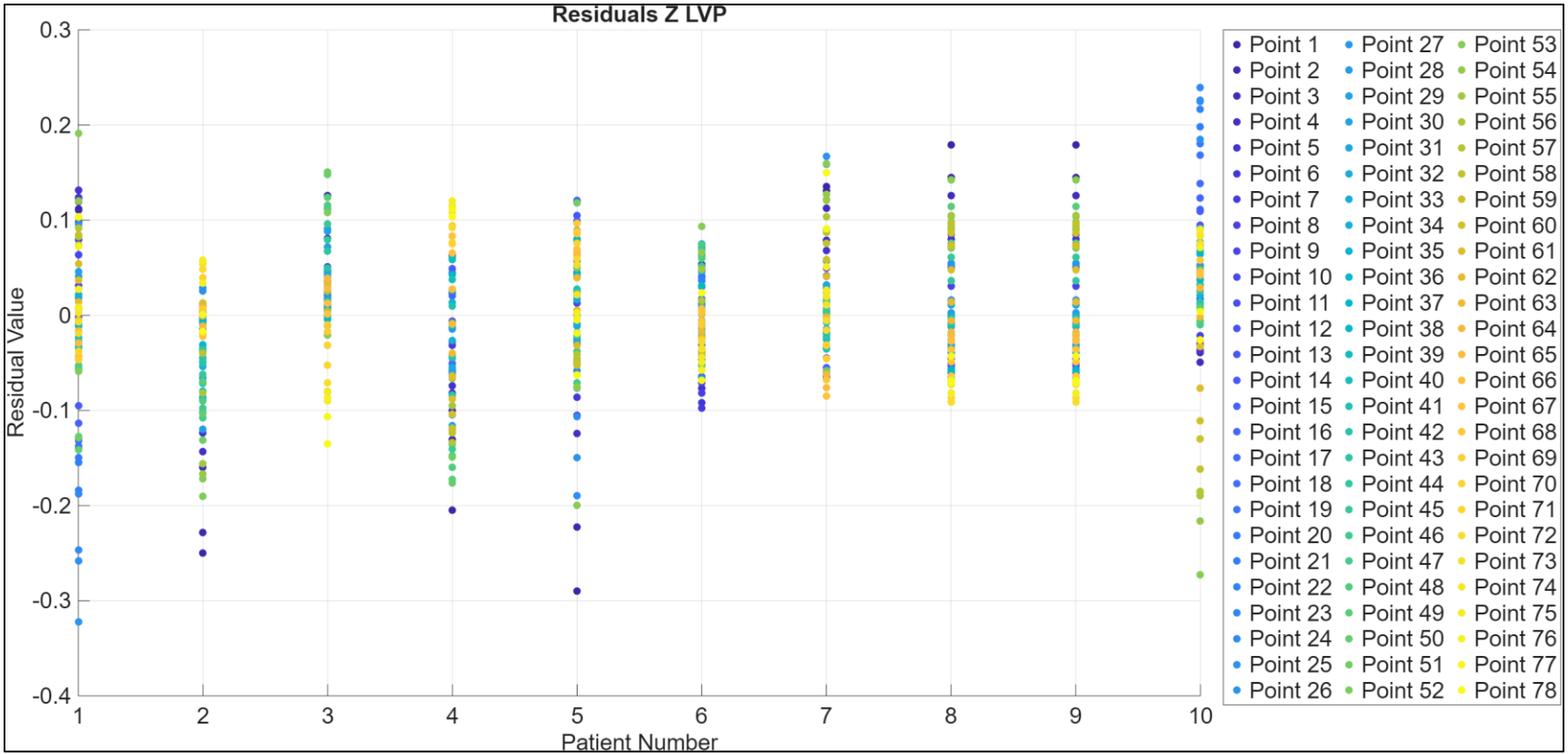

Figure B.42. *PCA residuals for the Z direction of the LVP. Points close to 0 indicate a strong fit with points farther away from 0 indicating a weaker fit.*

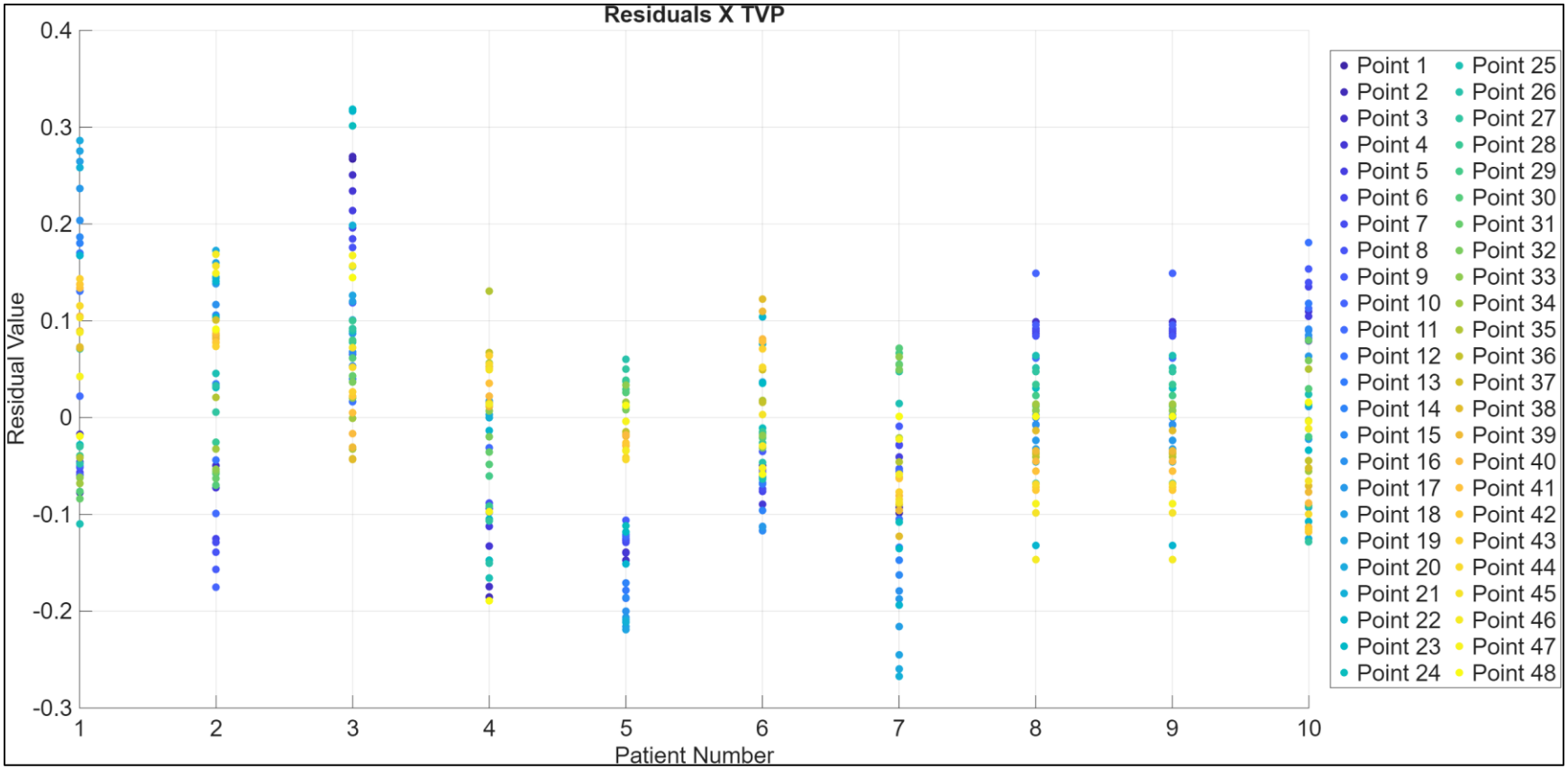

Figure B.43. *PCA residuals for the X direction of the TVP. Points close to 0 indicate a strong fit with points farther away from 0 indicating a weaker fit*

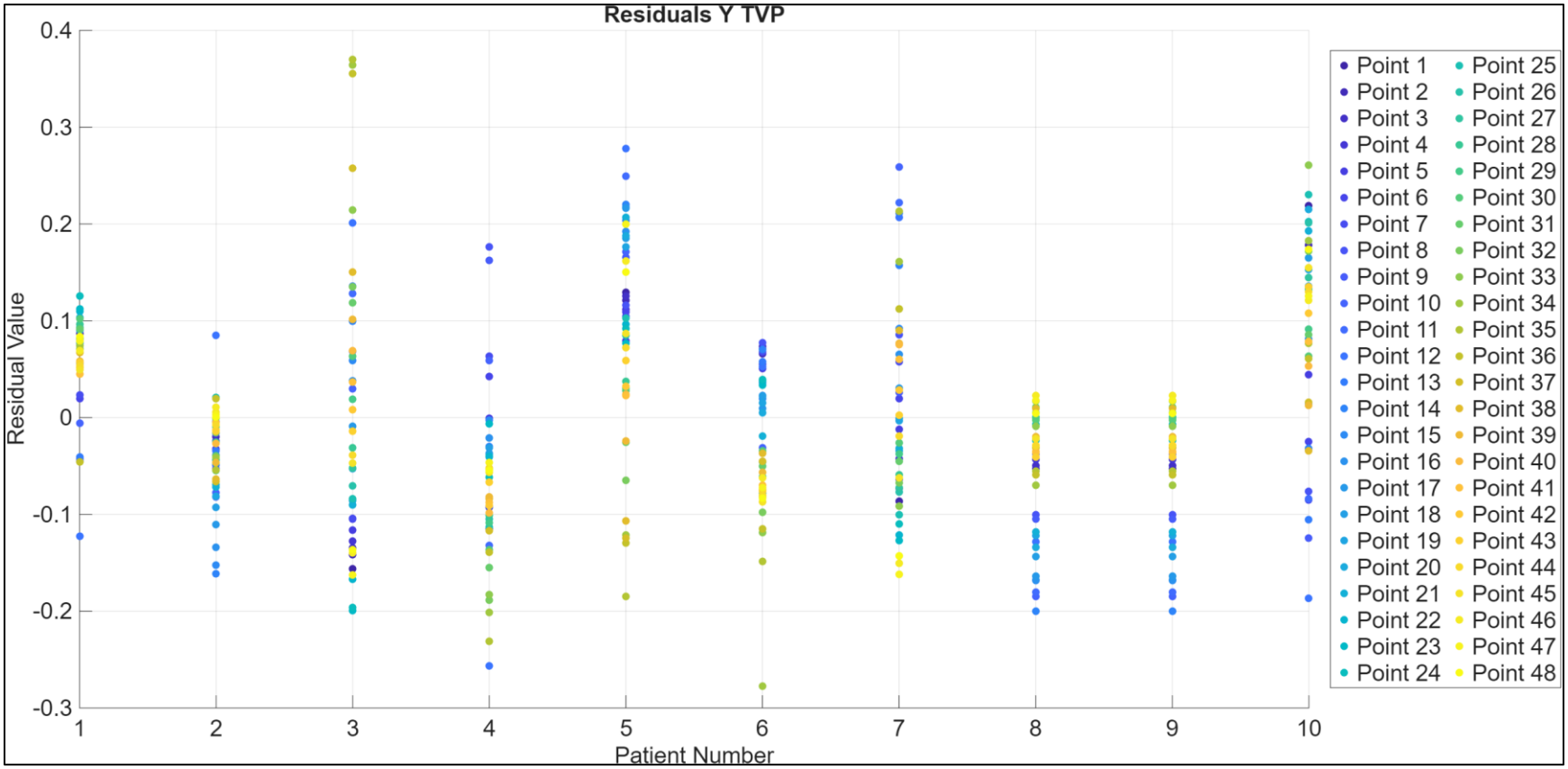

Figure B.44. *PCA residuals for the Y direction of the TVP. Points close to 0 indicate a strong fit with points farther away from 0 indicating a weaker fit.*

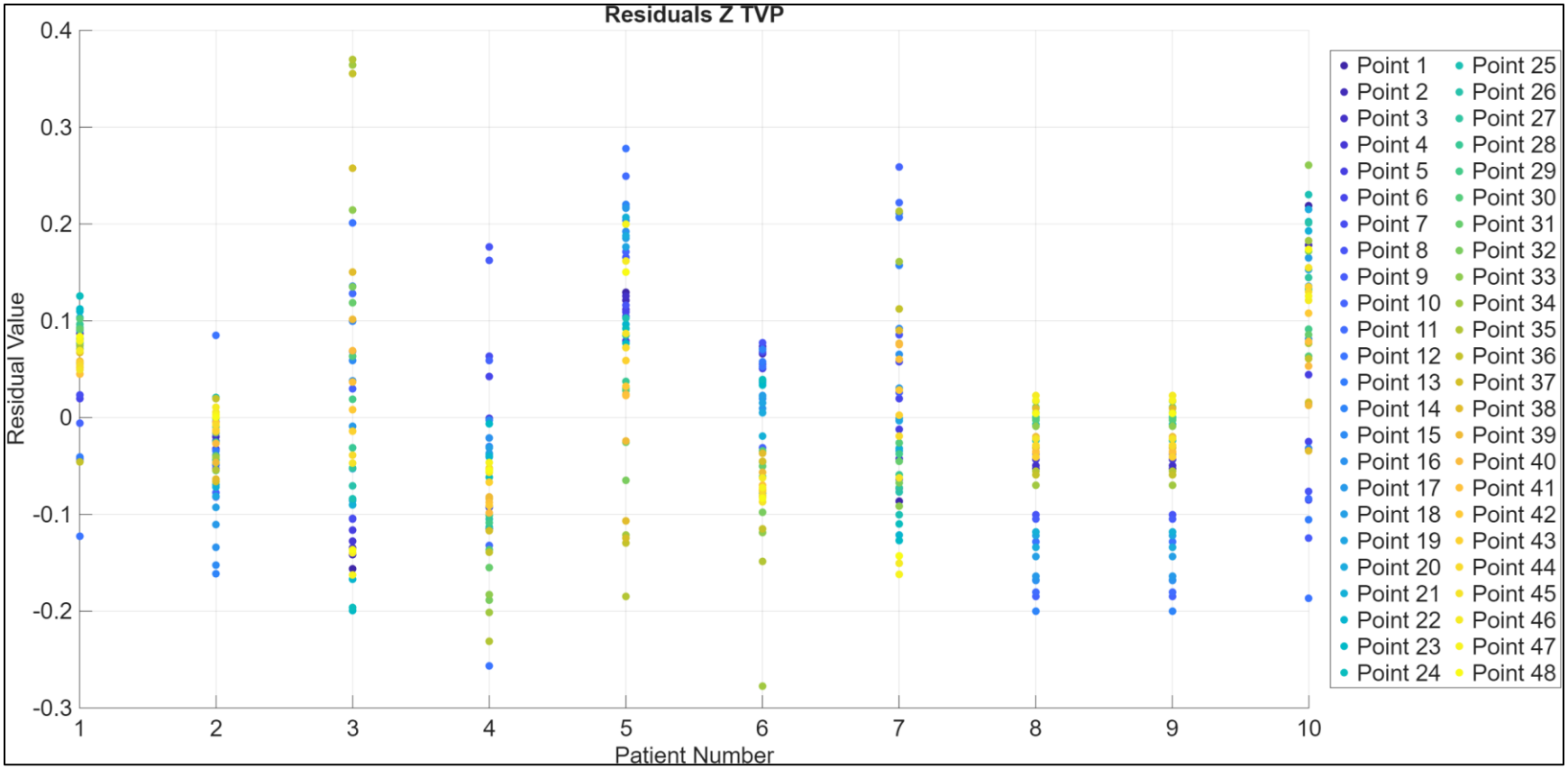

Figure B.45. *PCA residuals for the Z direction of the TVP. Points close to 0 indicate a strong fit with points farther away from 0 indicating a weaker fit.*

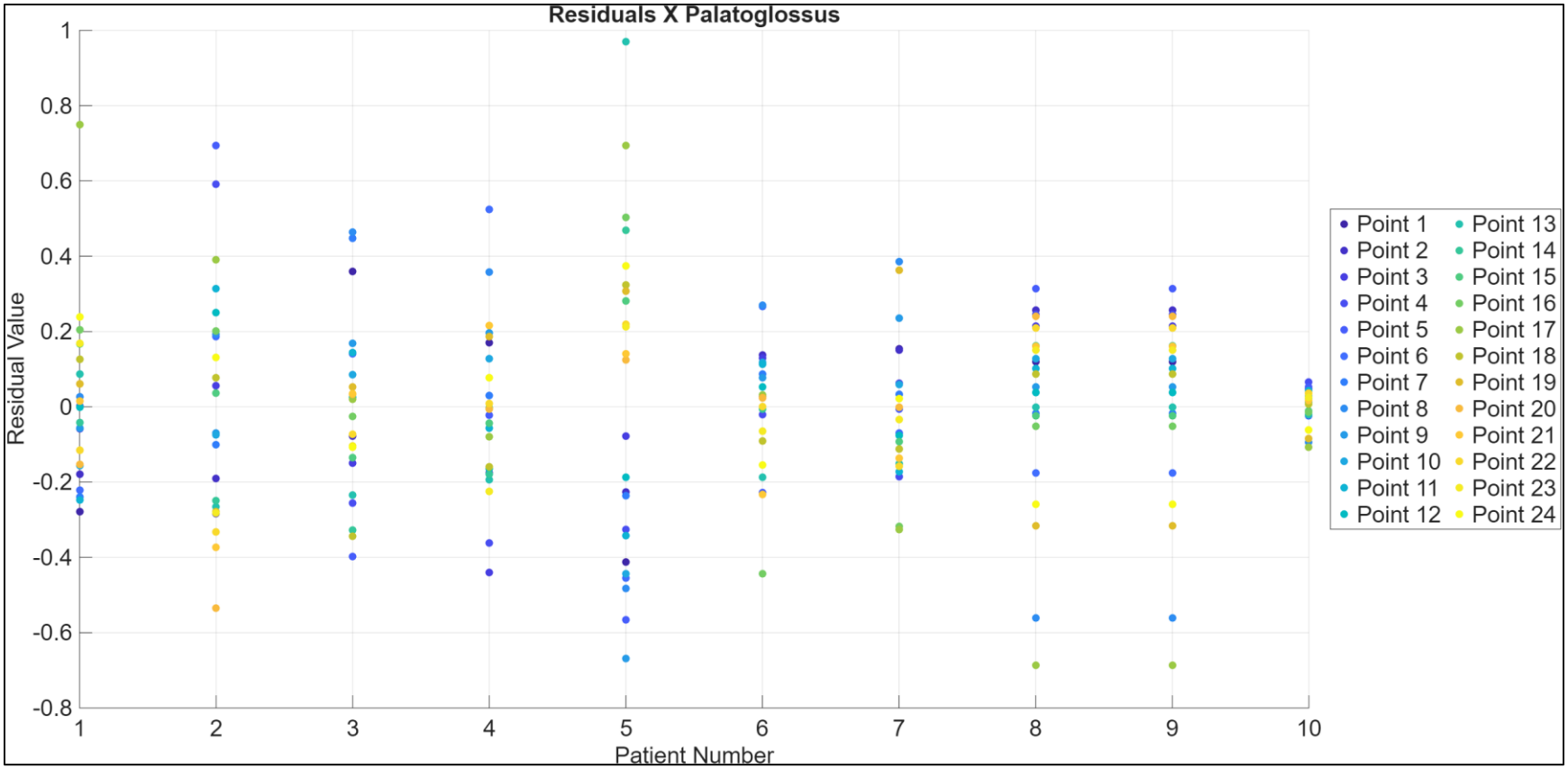

Figure B.46. *PCA residuals for the X direction of the Palatoglossus. Points close to 0 indicate a strong fit with points farther away from 0 indicating a weaker fit.*

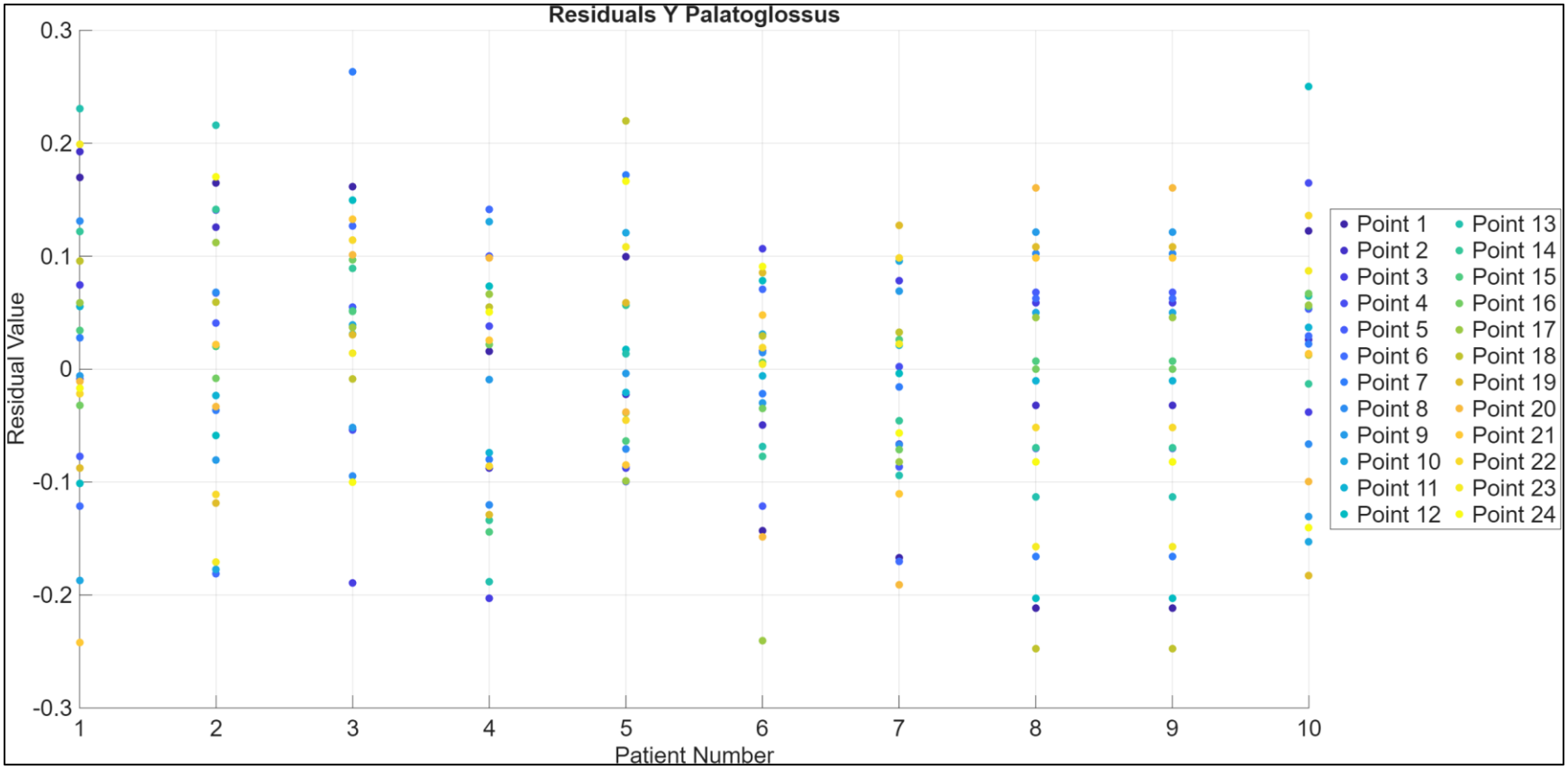

Figure B.47. *PCA residuals for the Y direction of the Palatoglossus. Points close to 0 indicate a strong fit with points farther away from 0 indicating a weaker fit.*

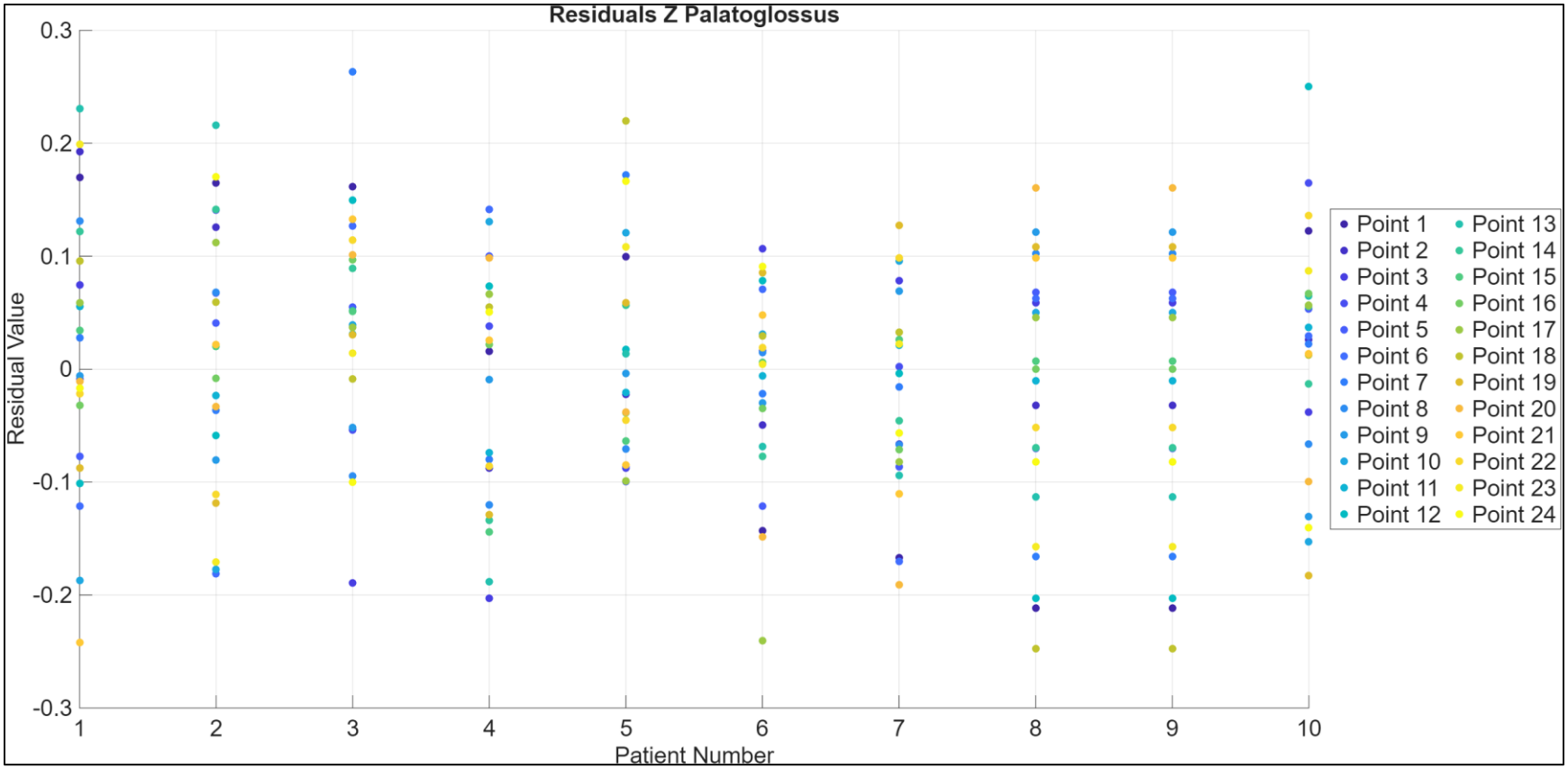

Figure B.48. *PCA residuals for the Z direction of the Palatoglossus. Points close to 0 indicate a strong fit with points farther away from 0 indicating a weaker fit*

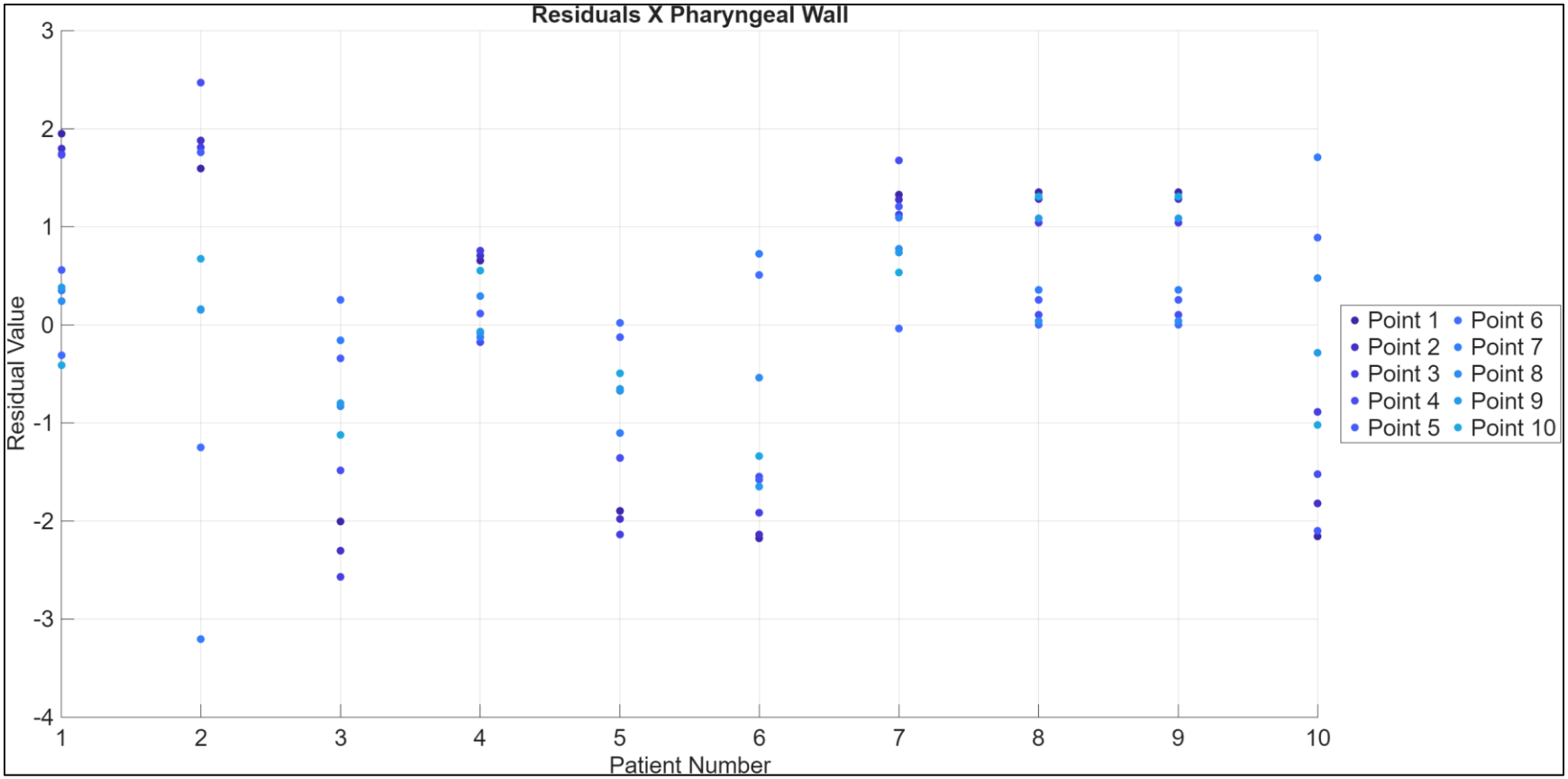

Figure B.49. *PCA residuals for the X direction of the Pharyngeal Wall. Points close to 0 indicate a strong fit with points farther away from 0 indicating a weaker fit.*

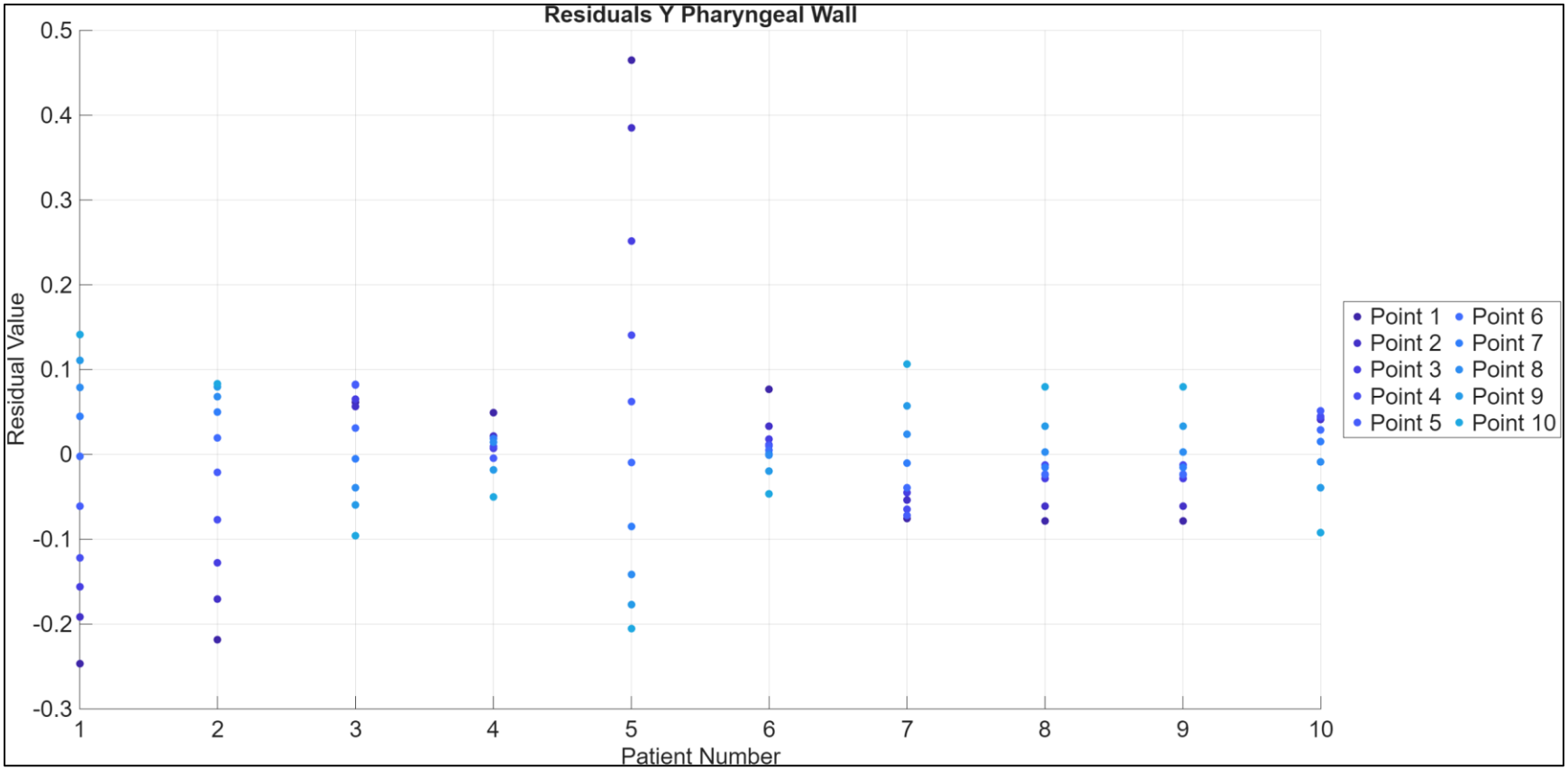

Figure B. *50. PCA residuals for the Y direction of the Pharyngeal Wall. Points close to 0 indicate a strong fit with points farther away from 0 indicating a weaker fit*

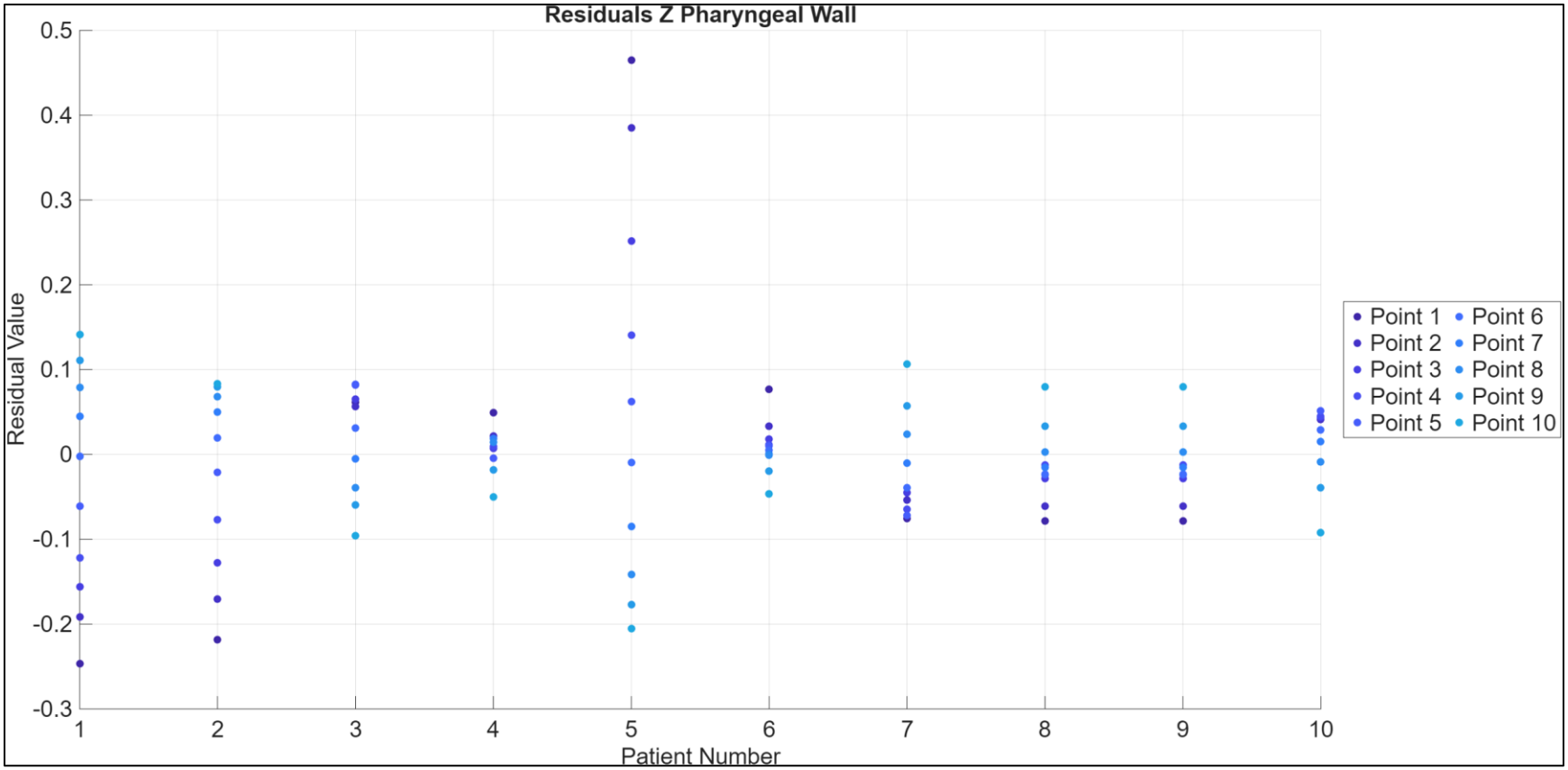

Figure B.51. *PCA residuals for the Z direction of the Pharyngeal Wall. Points close to 0 indicate a strong fit with points farther away from 0 indicating a weaker fit*

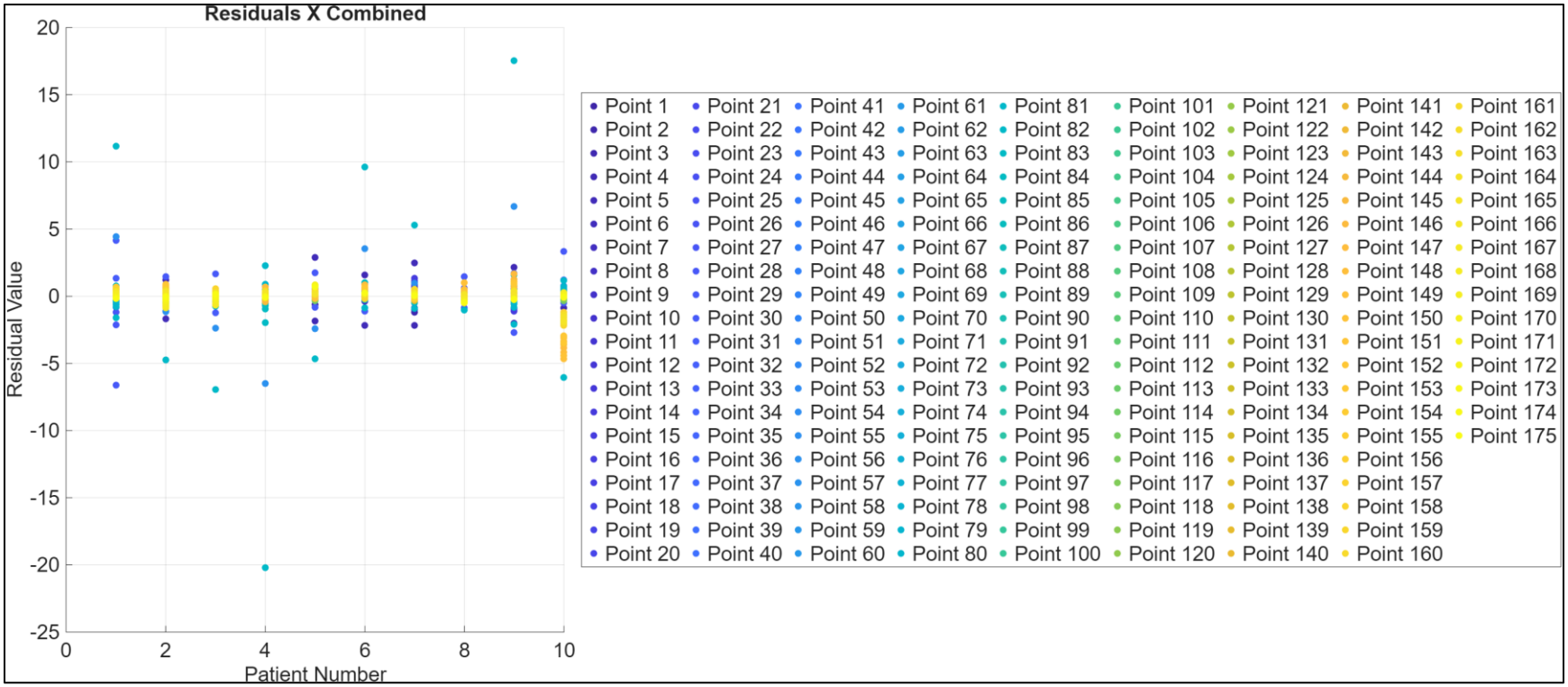

Figure B.52. *PCA residuals for the X direction combined coordinate sets. Points close to 0 indicate a strong fit with points farther away from 0 indicating a weaker fit*

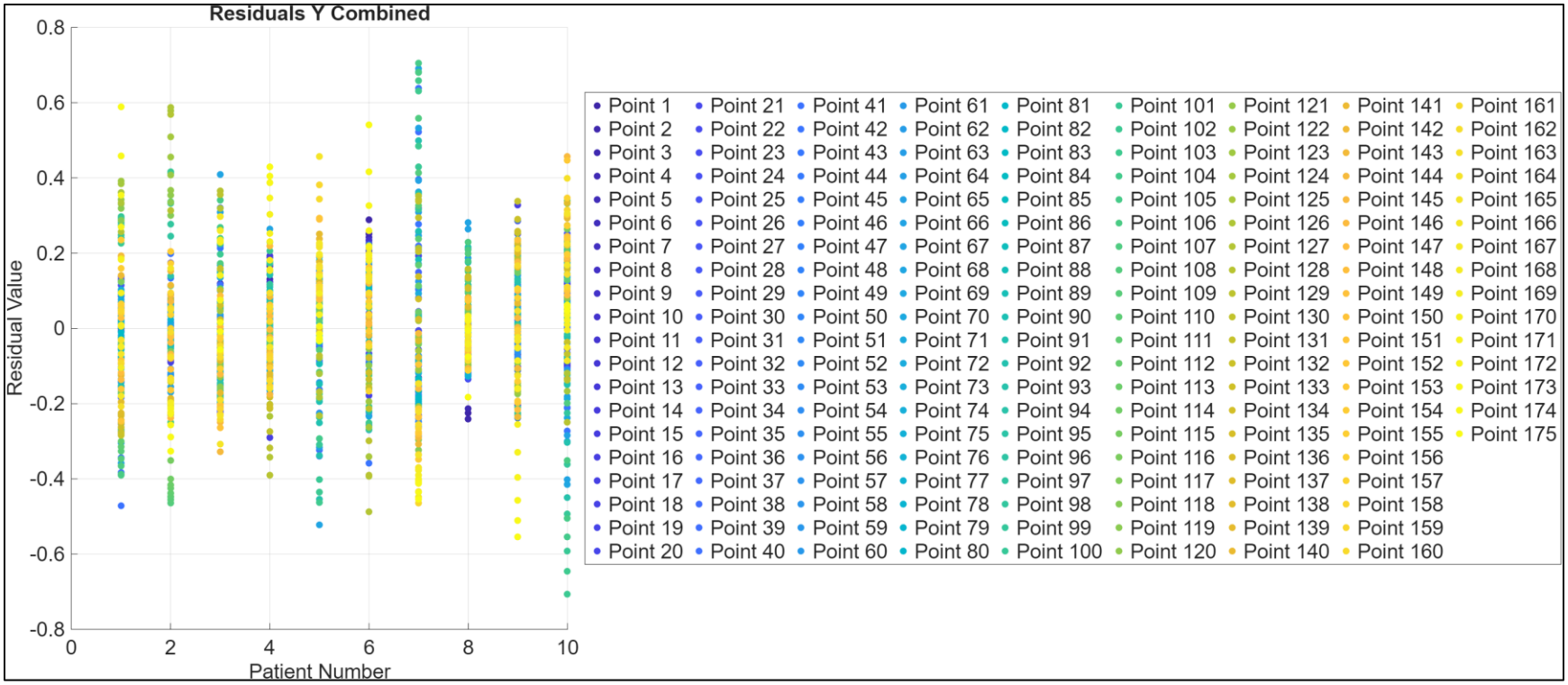

Figure B.53. *PCA residuals for the Y direction combined coordinate sets. Points close to 0 indicate a strong fit with points farther away from 0 indicating a weaker fit*

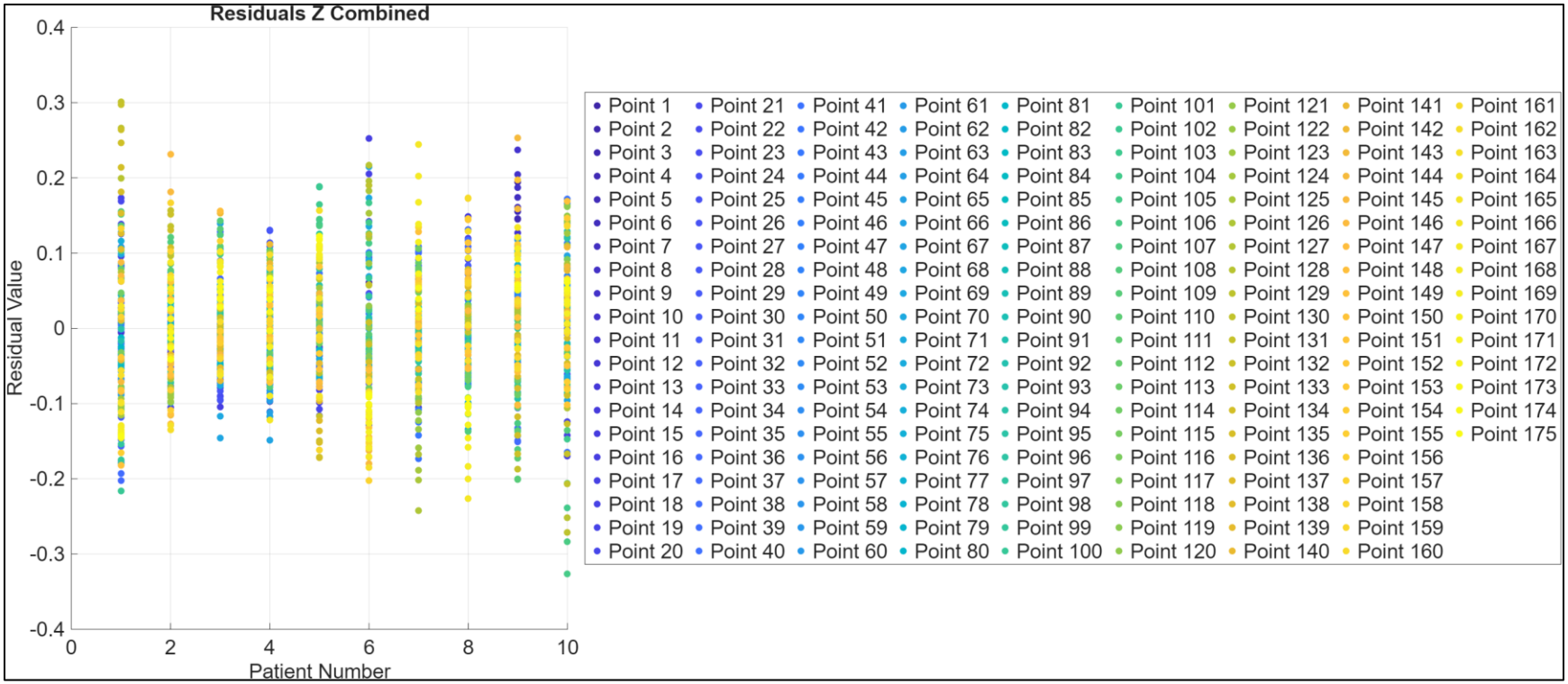

Figure B.54. *PCA residuals for the Z direction combined coordinate sets. Points close to 0 indicate a strong fit with points farther away from 0 indicating a weaker fit.*